

ZIRCON FERTILITY IN FLUVIAL SANDSTONES: A  
GEOCHRONOLOGICAL STUDY OF THE UPPER  
TRIASSIC SNADD FORMATION IN THE  
SOUTHWESTERN BARENTS SEA

Master in Geodynamics and Basin Studies

Vebjørn Johannes Selstad



Department of Earth Science

University of Bergen

March 2022





# Abstract

---

Detrital zircons are important for provenance studies and can provide answers to e.g., sediments source areas, palaeogeography, and tectonism. The use of detrital zircon geochronology has increased over the last two decades when it comes to provenance studies, and the importance of outlining biases and further developing methods are both wanted and important. Understanding the behaviour of zircon grains in fluvial systems is wanted, especially in the Barents Sea, where deposition of thick sediment packages with different provenance. The high interest is much because of the potential hydrocarbon exploration in the area. To better understand the fluvial effect and what this means on zircon grains in the southwestern Barents Sea, this thesis combines seismic, geochronology, facies analysis, and petrology to increase the knowledge on low-fertility subsurface formations.

Core 7131/4-1 penetrates the Guovca point bar and is recognizable on seismic and as 48 metres of core deposits. The samples were vertically collected from the subsurface core at the Norwegian Petroleum Directorate (NPD), exposed for geochronology measuring with LA-ICP-MS, and used for a hypothesis for fertility prediction. The hypothesis was tested through a second collection of samples at the NPD, which provided increasing understanding of fertility and support to the sampling model. This was accompanied with facies analysis which showed large variations in fertility in facies, which is interpreted to be caused by variation in energy flow conditions. Petrological description of all samples showed small variations. High proportions of quartz and rock fragments gives an immature signature. Large variations in zircon size are present in all samples, while the mean is stable. From the geochronology, early Permian to Late Devonian zircons with peaks at Carboniferous is displayed, matching the Uralian signature for the Barents Sea. Multidimensional plots (MDS) showed mostly similar age spectra, indicating low intraformational variations.

A Uralian provenance source is suggested for the studied material, with a point bar as the depositional environment. Fertility is assumed to be affected by energy flow conditions related to facies environment through patterns in the number of grains per gram sample in facies. The obtained knowledge from this thesis is important for the future sampling of low fertility sandstone, not only in the Barents Sea but also elsewhere.



# Acknowledgment

---

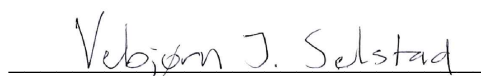
This thesis is a part of my M.Sc. degree in geodynamics and reservoir studies at the Department of Earth Science, University of Bergen. I want to use this section to show my greatest gratitude to all of those who has been in association in this project. First and foremost, I would like to thank my main supervisor Prof. Christian Haug Eide, it would have been much harder to finish this thesis in a pandemic without your guidance, encouragement, discussions, and feedback. You're truly a great person to work with. I would also thank my co-supervisor Hallgeir Sirevaag, you have been a of great value as well. Thanks for helping me during the first stay at NPD, with feedback, and guidance. I am very happy with how the projected ended up after our original plan was cancelled due to covid. Also, thank you to my co-supervisor Leif-Erik Rydland Pedersen, thank you for all the guidance and help with the SEM and LA-ICP-MS, and especially with the data. To my last co-supervisor, Albina Gilmullina, thank you for your help with the seismic data, and for discussions and guidance.

A special thanks to Ida Marie Gabrielsen and Lubna Sami Jawad Al-Saadi for helping me through my laboratory work.

Thanks to Sophie for proof reading.

To my fellow students and friends in Bergen and Stavanger, thank you for all the great memories throughout the time in Bergen, and especially through the last two years with covid restrictions. These would have been impossible to go through without the hikes, good evenings, and cabin trips. Thanks to my friends in Stavanger for making sure to remind me to visit them, and for visiting me as well.

A special thanks my family and to Gunnhild for her endless support, encouragement, and for always being there for me.



Vebjørn J. Selstad

Bergen, March 2022



# Table of content

---

|          |  |           |
|----------|--|-----------|
| <b>1</b> | <b>INTRODUCTION.....</b>   | <b>1</b>  |
| 1.1      | RATIONALE .....  | 1         |
| 1.2      | AIMS AND OBJECTIVES .....  | 4         |
| <b>2</b> | <b>GEOLOGICAL FRAMEWORK .....</b>  | <b>5</b>  |
| 2.1      | OUTLINE OF THE SW BARENTS SEA.....   | 5         |
| 2.2      | LITHOSTRATIGRAPHY AND SOURCES OF SEDIMENTS .....   | 5         |
| 2.3      | GEOLOGICAL EVOLUTION.....  | 7         |
| <b>3</b> | <b>THEORETICAL BACKGROUND.....</b>   | <b>13</b> |
| 3.1      | DETRITAL ZIRCON GEOCHRONOLOGY .....  | 13        |
| 3.2      | FLUVIAL ASPECT OF DETRITAL ZIRCON PROVENANCE.....  | 14        |
| 3.3      | DISTRIBUTIVE FLUVIAL SYSTEMS.....  | 15        |
| <b>4</b> | <b>METHODS AND DATA.....</b>   | <b>17</b> |
| 4.1      | SAMPLED COLLECTION .....   | 17        |
| 4.2      | SAMPLE PREPARATION .....   | 17        |
| 4.2.1    | Mineral separation.....  | 17        |
| 4.2.2    | Preparation of zircon mounts.....  | 20        |
| 4.3      | CL AND BS IMAGING.....   | 21        |
| 4.4      | LA-ICP-MS .....  | 21        |
| 4.5      | DATA PROCESSING .....  | 22        |
| 4.6      | SEISMIC DATASET.....   | 22        |
| <b>5</b> | <b>RESULTS .....</b>   | <b>23</b> |
| 5.1      | ANALYSIS OF THE GUOVCA CHANNEL IN 3D SEISMIC DATA.....   | 23        |
| 5.2      | SEDIMENTOLOGICAL ANALYSIS OF THE GUOVCA CHANNEL CORE .....   | 25        |
| 5.2.1    | Facies description .....   | 25        |
| 5.2.2    | Facies associations and flow conditions.....   | 32        |
| 5.3      | DETRITAL ZIRCON FERTILITY VARIATIONS.....  | 34        |
| 5.3.1    | Description of zircon fertility variations in initial 20 samples.....  | 34        |
| 5.3.2    | Hypothesis for controls on detrital zircon fertility .....   | 37        |
| 5.4      | ZIRCON GEOCHRONOLOGY .....   | 38        |
| 5.4.1    | Detrital zircon age distributions .....  | 38        |
| 5.4.2    | Multidimensional scaling .....   | 41        |
| 5.5      | ZIRCON SIZE .....  | 45        |
| 5.6      | PETROLOGICAL DATA.....   | 48        |
| 5.6.1    | Mineralogical description.....   | 48        |
| <b>6</b> | <b>DISCUSSION .....</b>  | <b>51</b> |
| 6.1      | WHAT CAN BE LEARNED ABOUT BARENTS SEA PROVENANCE AND GEODYNAMICS FROM THE NEW<br>GUOVCA POINT BAR ZIRCON AGE SPECTRUM? ..... | 51        |

|   |           |
|---|-----------|
| 6.1.1 Sediment sources in the Guovca point bar .....  | 51        |
| 6.1.2 Young Triassic zircon grains.....   | 53        |
| 6.2 WHAT CAUSES THE LARGE OBSERVED ZIRCON FERTILITY VARIATIONS?.....  | 55        |
| 6.2.1 Other fertility causes.....   | 57        |
| 6.3 IS THERE A SORTING/FACIES CONTROL ON ZIRCON AGE SPECTRA AS WELL? ARE THE DIFFERENT ZIRCON<br>AGE SPECTRA REPRESENTATIVE? DO THE DIFFERENT SAMPLES PASS STATISTICAL TEST FOR SIMILARITY? ..... | 58        |
| 6.3.1 Age spectra control.....  | 58        |
| 6.3.2 Representative age spectra and statistical approval.....  | 59        |
| 6.4 ADVISE FOR SAMPLING IN LOW ZIRCON-FERTILITY SANDSTONE .....   | 60        |
| <b>7 SUMMARY AND CONCLUSIONS.....</b>   | <b>62</b> |
| <b>8 FURTHER WORK .....</b>   | <b>64</b> |
| <b>REFERENCES .....</b>   | <b>65</b> |
| <b>APPENDICES.....</b>  | <b>72</b> |
| 8.1 APPENDIX I – SAMPLES .....  | 72        |
| 8.2 APPENDIX II – LA-ICP-MS.....  | 74        |
| 8.3 APPENDIX III – U-Pb DATA .....  | 76        |

## Abbreviations

---

|                                 |  |
|---------------------------------|--|
| <b><math>\rho</math></b>        | <i>Density</i>   |
| <b><math>\mu\text{m}</math></b> | <i>Micrometre</i>  |
| <b>A</b>                        | <i>Ampere</i>  |
| <b>BAR</b>                      | <i>Sample name Barents Sea</i>                                     |
| <b>BS</b>                       | <i>Backscatter</i>   |
| <b>c.</b>                       | <i>Circa (around)</i>  |
| <b>CL</b>                       | <i>Cathodoluminescence</i>   |
| <b>DIM</b>                      | <i>Diiodomethane</i>   |
| <b>Fm</b>                       | <i>Formation</i>   |
| <b>kV</b>                       | <i>Kilovolt</i>  |
| <b>LA-ICP-MS</b>                | <i>Laser ablation-inductively coupled plasma-mass spectrometry</i> |
| <b>LAS</b>                      | <i>Sample name LA-ICP-MS</i>                                       |
| <b>mRKB</b>                     | <i>Meters below the rotary table</i>                               |
| <b>n/a</b>                      | <i>Not applicable</i>  |
| <b>Pb</b>                       | <i>Lead</i>  |
| <b>RMS</b>                      | <i>Root-mean-square</i>  |
| <b>SEM</b>                      | <i>Scanning electron microscope</i>                                |
| <b>SW</b>                       | <i>Southwestern</i>  |
| <b>U</b>                        | <i>Uranium</i>   |





# 1 INTRODUCTION

---

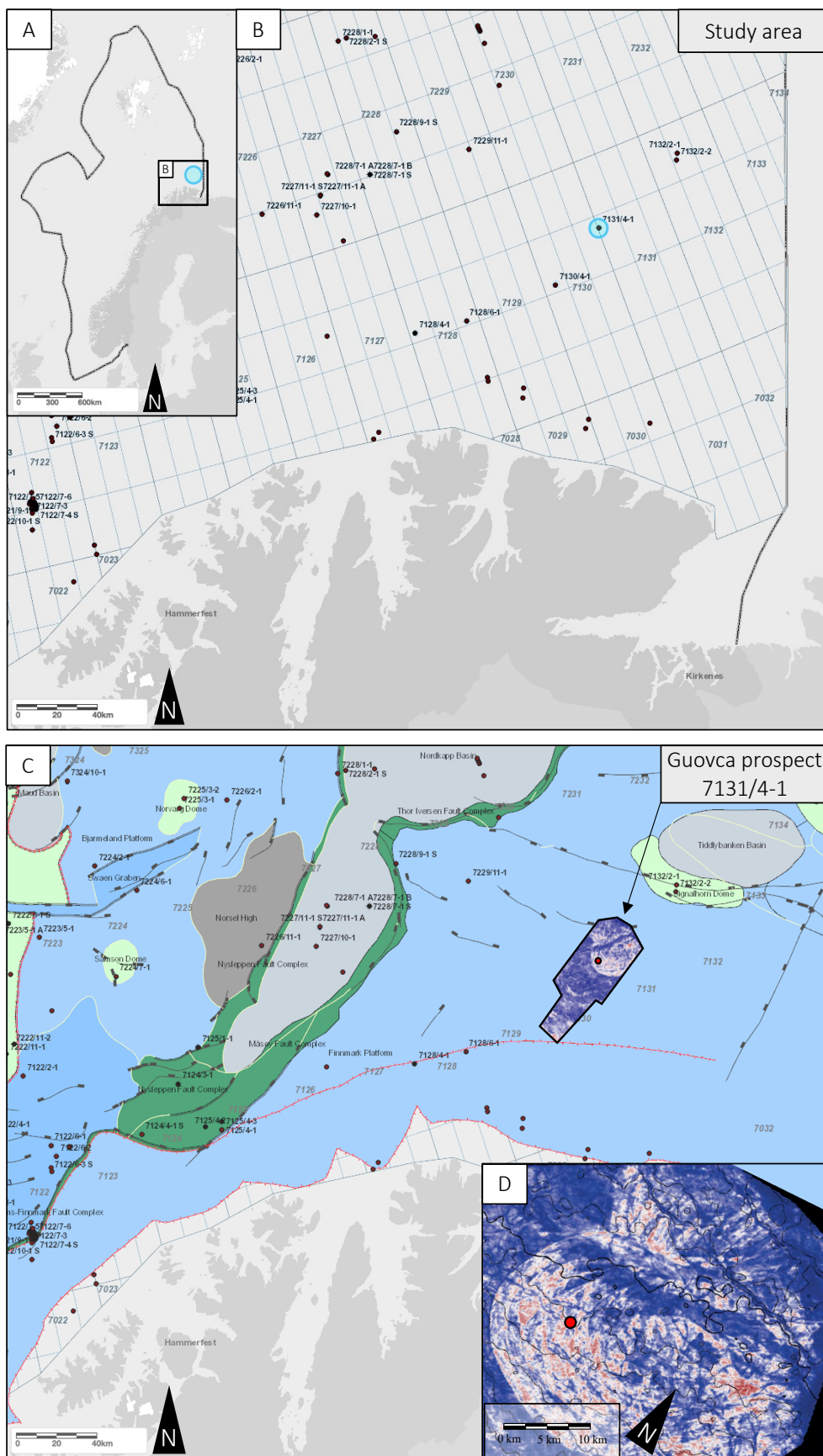
## 1.1 Rationale

Detrital zircon provenance of sedimentary rocks is a powerful method that gives good information on provenance areas by fingerprinting the timing of mainly felsic volcanism in the source area. In many cases source areas will have different geodynamic evolutions, making it possible to determine the source areas of sediments. This can be done connecting age populations in detrital zircon age spectra to known geodynamic events and dated rocks in the source area. Low price, prime equipment and relatively simple methods make this a popular method, but there are still important problems with this approach, such as zircon fertility, intraformational variability and various sorting effects.

The zircon fertility can place strong constraints on the obtained detrital zircon age spectra, especially for studies on subsurface formations in cores, where the sample size is limited. It has been suggested that at least 117 zircons should be dated in order to analyse all populations (which constitutes at least 5 % of the total population; Vermeesch, 2004). However, by analysing more zircons (around 1000), the certainty increases and allows for comparison between the size of the populations, something that can be difficult with limited number of analyses (Pullen et al., 2014).

Intraformational variability of zircon fertility and age spectra is little known. Information on the degree to which one can interpret differences between age spectra to have an important geological significance is limited (Saylor et al., 2013). By collecting similar weighted samples, fertility can be quantitative measured. Which is important for increasing knowledge on fertility one can use this to predict fertility in future provenance studies.

Sorting effects can change the primary detrital zircon age spectra because specific zircon age populations can have a different grain shape, and some shapes can be sorted out or get concentrated in specific areas (Augustsson et al., 2018; Chew et al., 2020). Some formations have very low zircon fertility (abundance of zircons in sample; Chew et al., 2020; Flowerdew et al., 2019), which makes it hard to collect and process enough sample material to obtain a good age spectre. This is especially a problem connected to studies of subsurface formations in cores since only a limited number of grams of material can be collected. For example, when sampling cores owned by the Norwegian Petroleum Directorate, each sample cannot weigh more than 35 g per sample, making it hard to do provenance with such small amounts of sample material.



**Figure 1.1:** A) Map of Norway, with study area highlighted in square and the Norwegian continental shelf is marked with a black line. B) Enlarged picture of the SW Barents Sea well 7131/4- is marked with a blue circle. C) Structural map of the study area shows important elements like Finnmark Platform, Nordkapp Basin, Hammerfest Basin and the Guovca prospect. D) RMS-amplitude maps display the contours of the meandering point bar, with well 7131/4-1 (red marker) penetrating the channel. Figures collected and modified from (NPD, 2021; Klausen et al., 2019; Klausen et al., 2014). 2

To better understand the factors governing the three sections mentioned above, this thesis focuses on the Triassic succession of the Barents Sea, because it is one of the better-studied formations in the world when it comes to sediment transport (Bugge et al., 1995; Glørstad-Clark et al., 2011; Klausen et al., 2014; Ryseth, 2014; Gilmullina et al., 2021), provenance (Mørk, 1999; Fleming et al., 2016; Klausen et al., 2017; Eide et al., 2018; Flowerdew et al., 2019). The significant interest has led to huge amounts of exploration data (2D- and 3D-seismic and cores) and a long history with scientific exploration has made the stratigraphy well known (Faleide et al., 1984; Glørstad-Clark et al., 2010; Henriksen et al., 2011; Gac et al., 2018; Worsley, 2008). Clearly visible clinofolds (Eide et al., 2018) and river channels (Klausen et al., 2014) display where the sediment originated from, and the different source areas are very well characterized from heavy minerals (Fleming et al., 2016), and zircon age spectra (Fleming et al., 2016; Line et al., 2020, Klausen et al., in press) that are strongly connected to the source area through seismic data.

The eastern sediment source in the Barents Sea is characterized by a detrital zircon age spectre with a major number of grains with an age peak at *c.* 300 – 330 Ma (Carboniferous), a smaller amount of age peak at *c.* 500 – 600 Ma (Cambrian – Early Neoproterozoic), and has low zircon fertility (Flowerdew et al., 2019). Specifically, the Guovca channel (Fig. 1.1D), a 19 km wide, 50 m deep meandering point bar body, which is well imaged gives the possibility to investigate the intraformational variations fertility, similarity in age spectra and provenance. The river deposit can be clearly observed in the seismic and in a core penetrating 43 of the 48 m of the channel, as well as five metres of the lake floor and paleosol deposits under. This study will collect samples from this channel to investigate sorting effects, fertility variations and intraformational variations in zircon spectra.

Additionally, this point bar deposit is 19 km wide and 50 m deep, making it comparable to rivers draining continental scaled water courses such as the Mississippi river (Klausen et al., 2019; Gilmullina et al., 2021). With a lateral migration rate of *c.* 59.1 m/year, the sediments deposited in the core must have been deposited in *c.* 300 years (Hudson and Kesel, 2000), much shorter than what can be caused because of tectonic, climatic, and geodynamic changes in the source area. This study investigates primary hydrodynamic sorting and intraformational variability which is relevant for sampling and interpretation of detrital zircon provenance studies, not geodynamic changes.

## 1.2 Aims and objectives

This thesis combines sedimentological core interpretation, detrital zircon geochronology and petrographic analyses, supported by seismic geomorphology aiming to improve the understanding on detrital zircon fertility and intraformational detrital zircon spectra variability within sedimentary rocks. To accommodate this aim, the following objectives has been made.

1. Seismic interpret the most distinct horizons in the early Snadd Fm and provide attribute map of the ancient meandering Guovca point bar deposits in the SW Barents Sea study area and (Fig. 1.1D).
2. Perform detailed sedimentological description of the cored interval. Perform a facies analysis of the Guovca point bar and interpret the associated energy environment therein and provide a sedimentological model for the point bar.
3. Densely sample core 7131/4-1 for further detrital zircon provenance and provide a hypothetical model on fertility sorting of zircons and test it.
4. Present the zircon age spectra generated from the detrital zircon grains and test them for statistical similarity. Outline the intraformational variation of fertility and age spectra.
5. Assess whether there are facies or sorting control on zircon age spectra in the studied deposits, and offer recommendations for sampling of low zircon-fertility fluvial sandstone

## 2 GEOLOGICAL FRAMEWORK

---

### 2.1 Outline of the SW Barents Sea

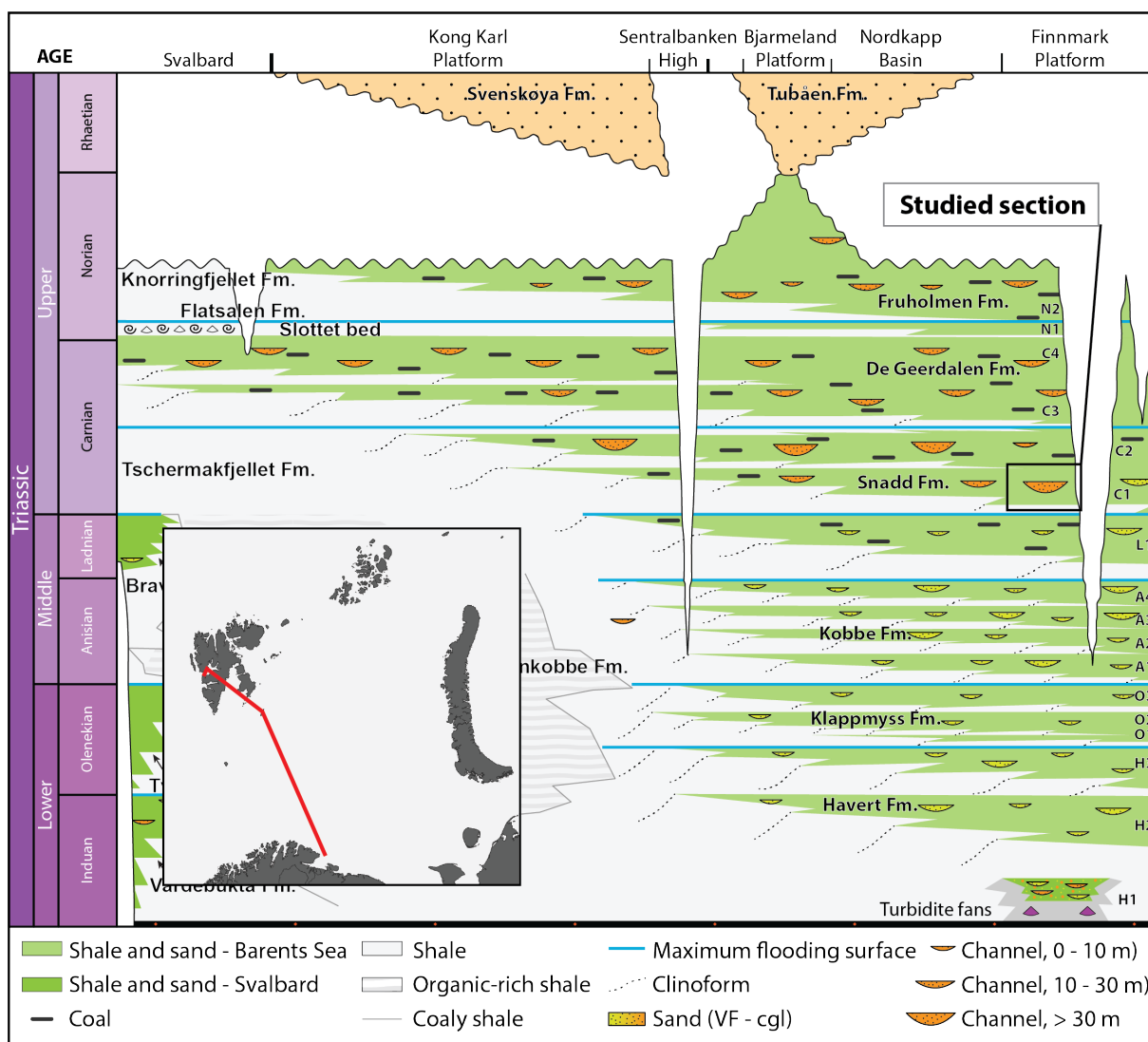
The Guovca prospect is located on the Finnmark Platform in the southwestern part of the Barents Sea, at around 71 °N and 31 °E, just northeast of Hammerfest (Fig. 1.1A). The SW Barents Sea is an epicontinental basin with complex evolution and structural elements (Faleide et al., 1984). The area is bounded by young passive continental margins in the north and west, enclosed by Novaya Zemlya in the east and Franz Josef Land and Svalbard archipelagos in the north (Dengo and Røssland, 1992; Gudlaugsson et al., 1998). The mentioned structural elements have a trending orientation aligned with the Caledonians, NNE – SSW, and have since worked as sedimentary basins (Klausen et al., 2014; Glørstad-Clark et al., 2010). Through time the SW Barents Sea has undergone a complex structural evolution after the Caledonian orogeny ceased in the Early Devonian – late Silurian, 420 – 359 Ma (Gudlaugsson et al., 1998).

### 2.2 Lithostratigraphy and sources of sediments

The SW Barents Sea host an almost continuous sedimentological record covering the deposits from upper Paleozoic to Cenozoic times (Glørstad-Clark et al., 2010), representing the time-span from when the SW Barents Sea was located close to the equator to its present-day location. The sedimentological record of SW Barents SE is highly influenced by the change in climatic environment caused by the northward movement (Smelror et al., 2009; Gilmullina et al., 2020). The Triassic sediments are represented by six lithostratigraphic units; Havert-, Klappmyss-, Kobbe-, Snadd-, De Geerdalen-, and Fruholmen Formation, each representing a cycle of transgression and regression, separated by maximum flooding surfaces (MFS; Klausen et al., 2015; Glørstad-Clark et al., 2010), akin to the subgroups Sassendalen, Storfjorden, and Realgrunnen.

At the Finnmark platform, the Havert Fm (Induan) is recognized by mostly siltstone with clinoforms and mud-rich topsets rich in mud that hosts sandy fluvial deposits (Eide et al., 2018; Rossi et al., 2019; Gilmullina et al., 2020). Paleogeographic reconstruction indicates both Fennoscandian and southeastern areas as sediment sources (Glørstad-Clark et al., 2010). The overlaying Klappmyss Fm (Olenekian) consists of dark shales with thin sandstone beds. Prograding clinoform patterns imply two sources of deposition during this period as well (Gilmullina et al., 2020; Glørstad-Clark et al., 2010). During the Lower Triassic, the subsidence rates of the basin were high and large amounts of sediments were deposited in the SW Barents Sea (Gilmullina et al., 2020).

The Middle Triassic is separated into the Kobbe Fm (Anisian) and the Snadd Fm (Ladinian). sedimentation rates decreased during this period due to a much calmer tectonic period (Gilmullina et al., 2020). The Kobbe Fm is recognized by stepwise filling on the Loppa High, containing sandstone, siltstone, and shales in fluvial and delta-front environments (Smelror et al., 2009). The Snadd Fm, which is the focus of this thesis, consists of sediments with thickness up to 1500 m, thickening in a westward direction. The Middle Triassic consists of marine shales and siltstone in the west, interbedded with sandstone channel bodies in-between (Klausen et al., 2014).



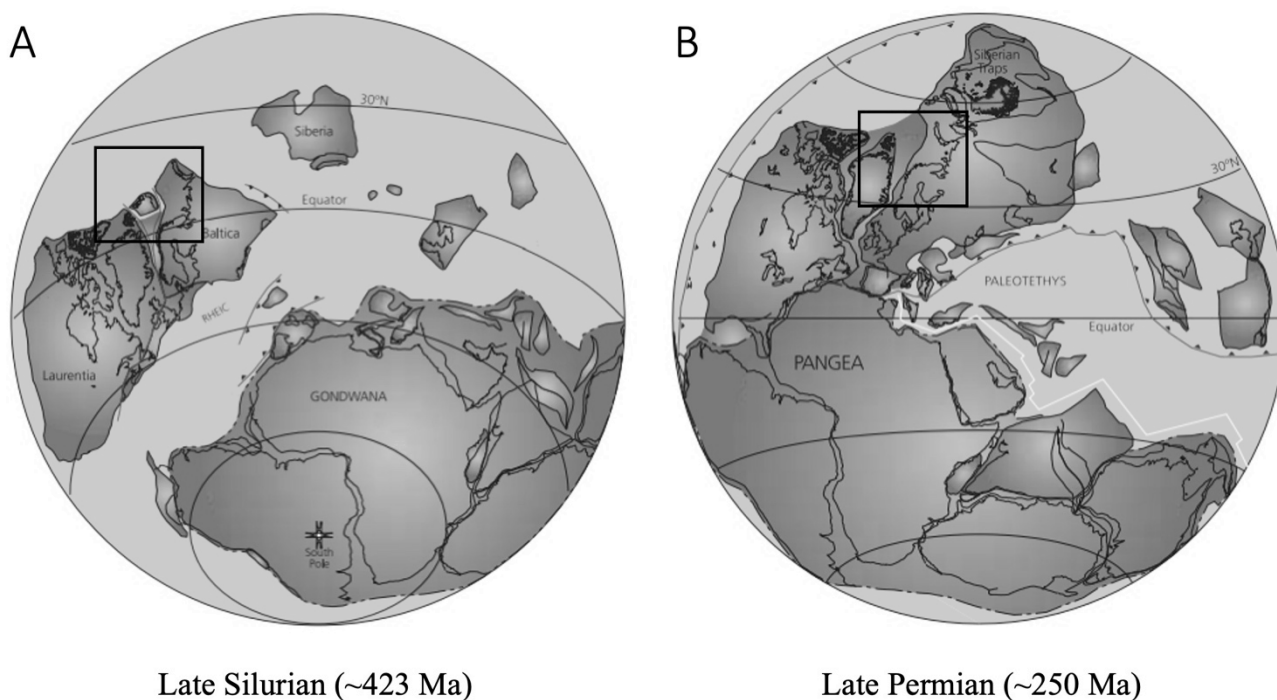
**Figure 2.1:** Lithostratigraphic chart of correlated Triassic deposits across the Greater Barents Sea. Ranging from the Induan to Rhaetian. Increase in western prograding shale-and channel systems into the Triassic. Increase in eroded material occurs in the mid-Norian and continuous throughout the Triassic. Relevant sequence is marked with a black and yellow square, including the Ladinian to Early Norian Snadd Formation. Modified from Gilmullina et al. (2020).

A southeastern source is interpreted from clinoform progradation from the east. Clinoform patterns also occur from the Fennoscandian Shield indicating an active but limited source region from the south (Glørstad-Clark et al., 2010). The Snadd Fm continuous into the Carnian, which

is recognized as a flooding surface. The Carnian unit consists of similar deposits, only the sandstone bodies increase in thickness and width (Gilmullina et al., 2020). The Carnian Snadd Fm is overlain by a Norian flooding surface, marking the ending of a massive progradation of widespread deposits in the Snadd Fm (Fleming et al., 2016). A petrographic change occurs in the transition from Snadd- to the Norian Fruholmen, a transition from a litharenithic sandstone to a mature quartz arenite (Ryseth, 2014; Line et al., 2020). The Rhaetian Tubåen Fm marks the end of the Triassic, a sandstone dominated package with thin coal layers, and mudrock. The transition between Fruholmen Fm and Tubåen Fm is marked by an increase in amount of sandstone (Ryseth, 2014). In the southwestern area, parts of the Late Triassic formations have been eroded in later times the upper formation much more than the lower ones (Nøttvedt et al., 1993).

### 2.3 Geological evolution

The southwestern Barents Sea has been substantially influenced by several compressional and extensional events since the Paleozoic. The Caledonian Orogeny formed in response to the oblique continental collision between Laurentia and Baltic cratons during the Ordovician – Late Devonian times (Fig. 2.2; Gac et al., 2018). During late Silurian – early Devonian times, the crystalline basement of the Barents Sea formed as the Caledonian metamorphic and igneous rocks consolidated (Doré, 1995; Gudlaugsson et al., 1998). An important phase of the orogenic evolution, a late Devonian transition from collision to collapse occurred, as well as the onset of the north-east rifting between the Atlantic-Arctic (Smelror et al., 2009). This led to the Late Devonian development of NE – SW oriented fan-shaped half-graben system, and a distinct basin physiography and networks of sediment routes (Faleide et al., 1984; Dengo and Røssland, 1992; Gudlaugsson et al., 1998). Evaporite deposited and carbonate platform coverage started to form in these basins during the late Carboniferous – early Permian. This was because of the tropical and humid environment, and minor clastic deposits derived from nearby areas (Bugge et al., 1995; Eide et al., 2018). The northern continental movement in Silurian to Permian (Figs. 2.2A and B) led to a depositional change of more clastic sediments (Faleide et al., 1984). Through the Paleozoic, continents went from being initially separated to colliding and making up the supercontinent Pangea, concurrently drifting towards a more arctic environment. Rifting events in the Late Permian caused accommodation space large enough for the major amounts

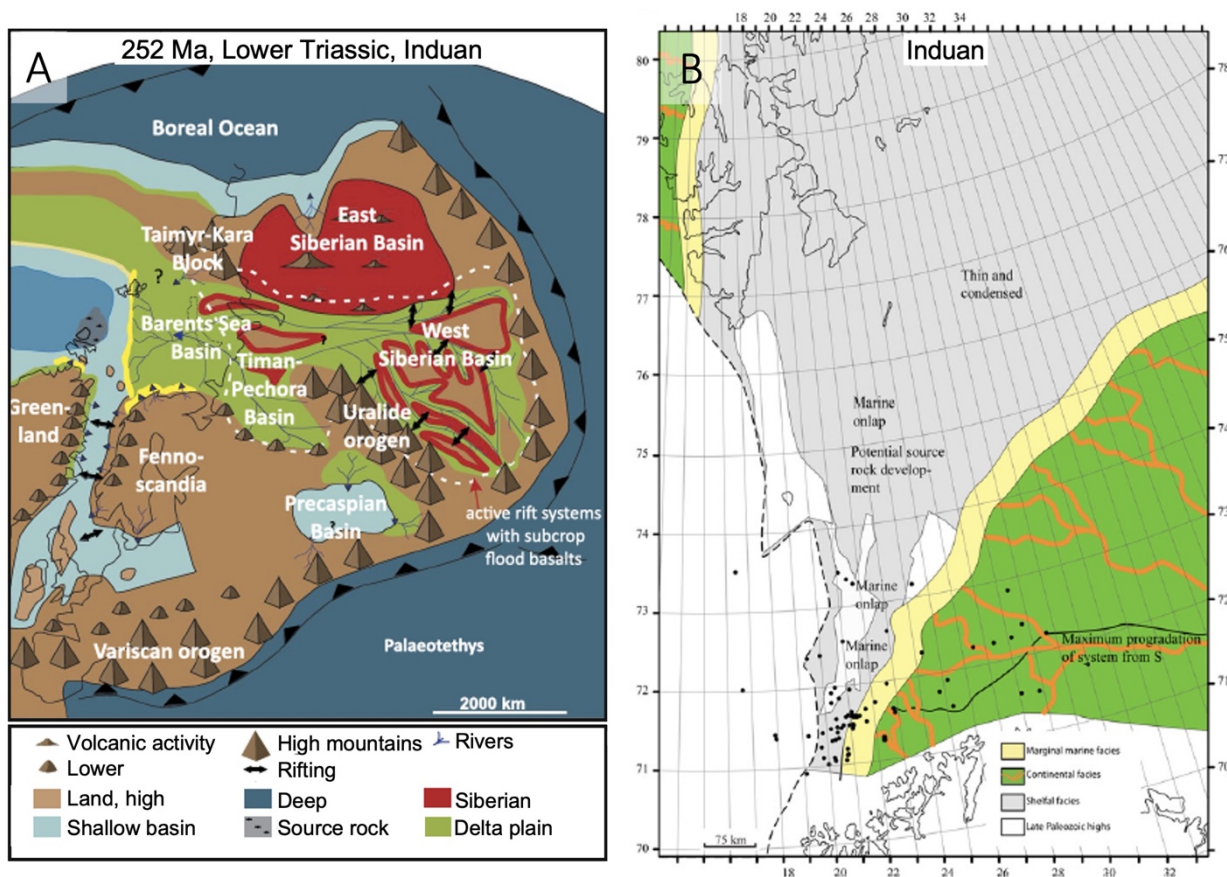


**Figure 2.2:** Paleogeographic reconstruction of late Silurian (A) to late Permian (B) continental drift. The Barents Sea area moved from the equator to around 40–50 °N. Collision led to formation of the Caledonian orogeny and the supercontinent Pangea. Late Permian gas releases and eruptions in the Siberian Traps Large Igneous Province leading to mass extinction and increased global average temperature. Modified from Smelror et al. (2009).

of clastic sediments to deposit (Gac et al., 2018). These deposits were primarily derived from the Uralian Orogeny, a continent-continent collision between West Siberian Craton and Baltica, initiating in early Carboniferous to late Permian (Puchkov, 2009). During this time the marine connection between the southeast and The Barents Sea started to close, forcing the sediments to transport northeast (Smelror et al., 2009).

The transition from the Paleozoic to the Mesozoic marks a major change in the Earth's environment, caused by the Permian – Triassic gas release and major eruptions in the Siberian Trans large igneous province (Eide et al., 2018; Puchkov, 2009). Most important, the gas release lead to increased sedimentation as a consequence of rising global temperature and acidic rain, causing deforestation and increased chemical weathering (Algeo and Twitchett, 2010). During the Triassic, the SW Barents Sea was still a part of the supercontinent Pangea, located at around 44 – 49 °N (Klausen et al., 2015). During this period the Basin was highly affected by sediments deriving from the Uralian Mountain Belt in the southeast and by structural extension between Fennoscandia and Greenland (Fig. 2.3A; Ryseth, 2014). This led to subsidence of the Barents Sea leading to the formation of the foreland basin and as source of prograding fluvial- and deltaic deposits reaching up to 20 km in the deepest parts and 2.5 – 3



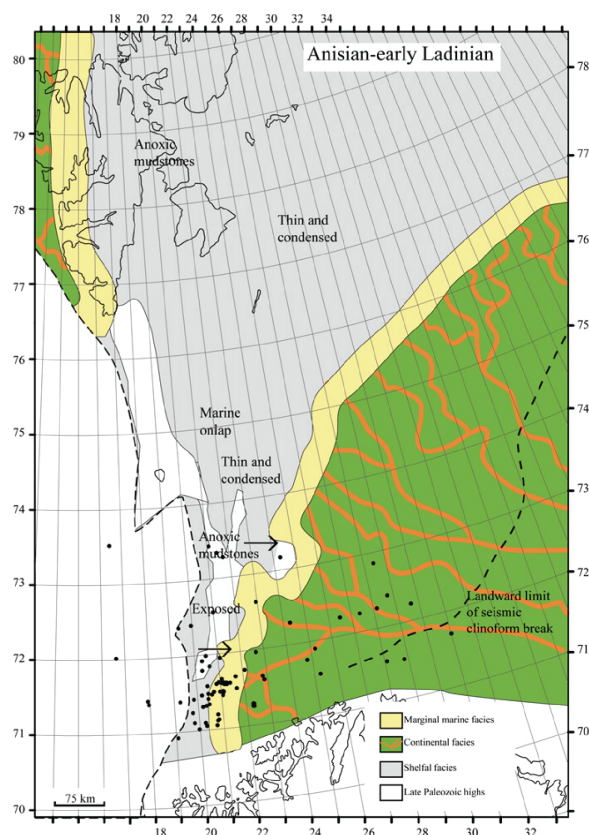


**Figure 2.3:** A) Paleogeographic map of the regional setting of the Great Barents Sea during the lower Triassic Induan period. Maximum progradation only touched the southwestern margin of the Barents Sea Basin. Uplift of the Uralian Mountain Belt, Atlantic rifting, and major sediment infilling in the Barents Sea. Modified from Gilmullina et al. (2020) B) Paleogeographic map showing reconstruction of the western Barents Sea during the Triassic Induan. Delta environment prograding towards from the southeast. Channel systems transporting clastic sediments along the delta surface. Modified from Glørstad-Clark et al. (2010)

km in the distal parts like the SW Barents Sea (Henriksen et al., 2011; Ryseth, 2014; Haile et al., 2021). In the North Atlantic, westward rifting led to subsidence of the western part of the Barents Sea, and a SW Barents Sea coastline kept prograding towards the west (Fig. 2.3B; Glørstad-Clark et al., 2010; Flowerdew et al., 2019). During the late Triassic – early Jurassic, minor sources of non-marine sediments from the Novaya Zemlya and the Fennoscandian shield filled up in the basin (Gilmullina et al., 2020).

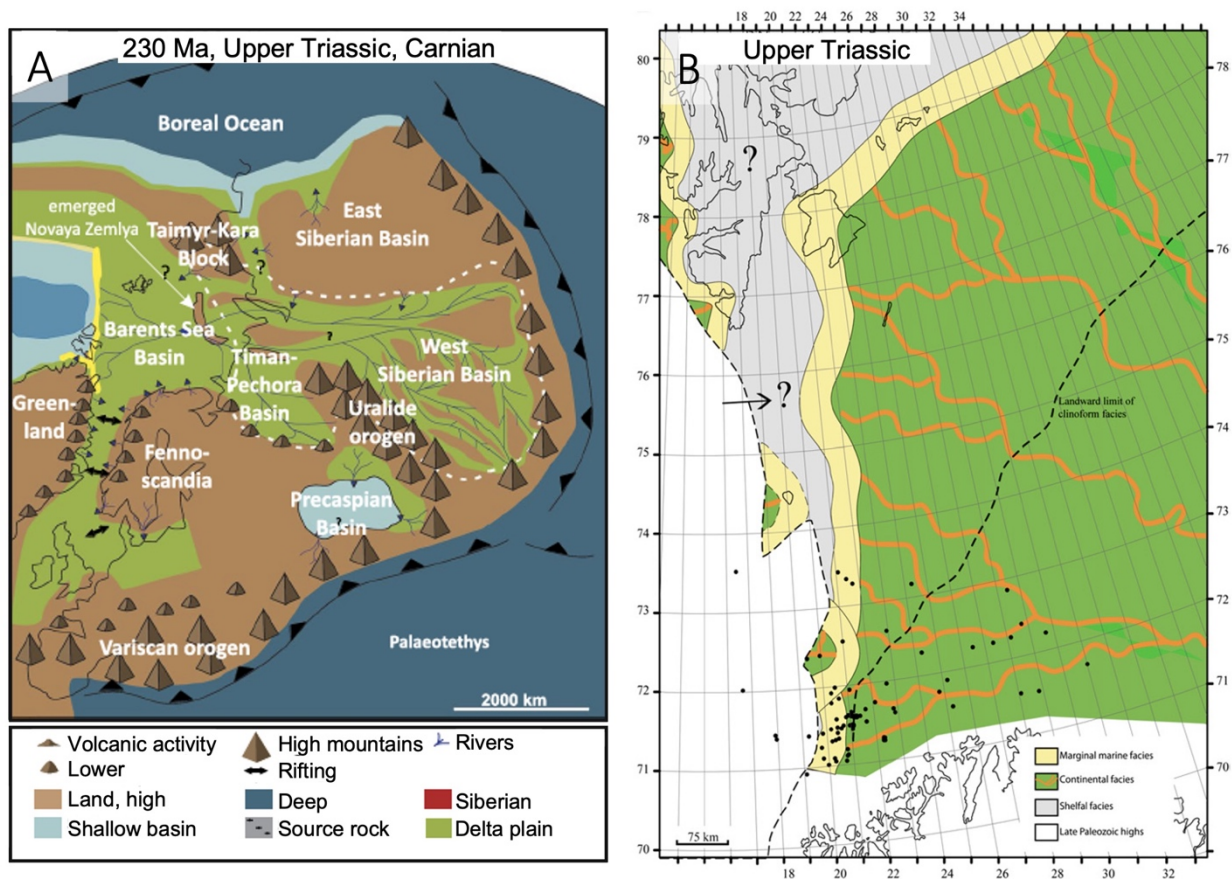
The climate during middle Triassic was moderately humid, resulting in continuous increase in erosion and transport from the Uralian Mountain Belt. The Finnmark- and Bjarmeland Platform experienced little tectonic activity compared to the surrounding, and only minor subsidence was recorded here. The area along the western margin was more active, with occurring fault activity and the uplift and erosion of Loppa High which became an area of deposition in the late Triassic, before re-activating as high later in the Triassic (Henriksen et al., 2011). The Triassic delta kept prograding towards the north-east (Fig. 2.4) as siliciclastic deposits were transported in fluvial

distribution systems, transforming the basin from marine deposition to more deltaic and continental (Gac et al., 2018; Glørstad-Clark et al., 2011). Variation in the supply of sediments was affected seasonally in the SW Barents Sea. In calmer periods, thick packages of organic-rich shale were deposited, while thick fluvial sandstone sequences were deposited during more turbulent periods (Klausen et al., 2019). As the delta prograded north-westward, fluvial channel systems evolved in the surface of the delta, turning bigger and more complex. At the same time, minor amounts of sand were transported from the Fennoscandian shield (Smelror et al., 2009). This can be seen in seismic patterns, through clinoform geometries at the Finnmark Platform (Glørstad-Clark et al., 2010).



**Figure 2.4:** Paleogeographic map showing reconstruction of the western Barents Sea during the Triassic Ladinian to early Carnian. More northeast progradation compared to the Induan. Maximum progradation reached more towards the western Barents Sea Basin. Delta environment prograding towards from the southeast. Channel systems transporting clastic sediments along the delta surface. Modified from Glørstad-Clark et al. (2010).

The Carnian was a time of marine regression in the Arctic, leading to an extensive progradation of the Barents Sea delta. The associated Snadd Fm is distributed widely over the Barents Shelf (Fig. 2.5B), varying in thicknesses between 1000 to 1200 m (Ryseth, 2014). Near-shore and coastal environments moved westward (Fig. 2.5A), affecting the more terrestrial environments, like the ones covering the Finnmark platform (Smelror et al., 2009; Gac et al., 2018). Climate changed in the Arctic during the Middle- to Late Triassic, from humid conditions to dry



**Figure 2.5:** A) Paleogeographic map of the regional setting of the Great Barents Sea during the lower Triassic Induan period. Maximum progradation reached all the way to the Svalbard Archipelago. Transportation was high during this time, and the Barents Sea delta probably reached its maximum during the Carnian. Modified from Gilmullina et al. (2020) B) Paleogeographic map showing reconstruction of the western Barents Sea during the Triassic Carnian. Delta environment reaching all the way to the Svalbard Archipelago. Modified from Glørstad-Clark et al. (2010).

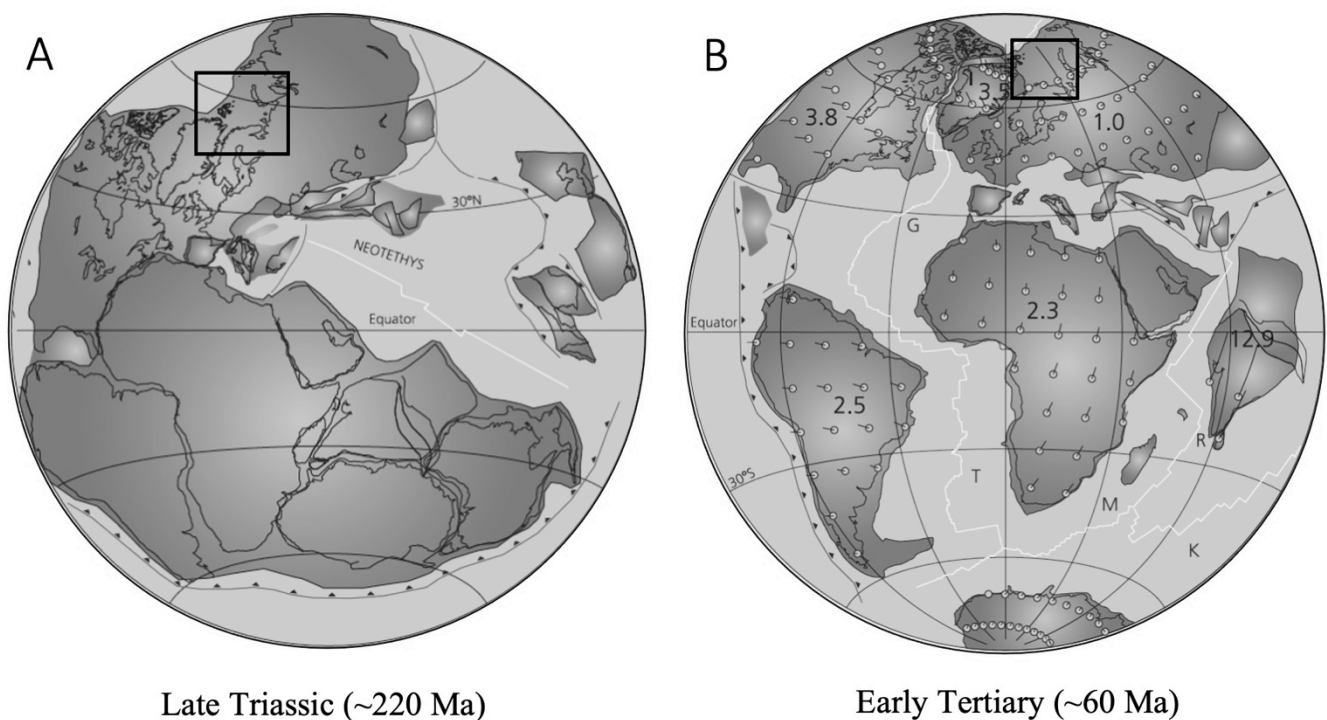
conditions as the continent moved to around 50 °N (Fig. 2.6; Hochuli and Vigran, 2010; Mangerud and Rømuld, 1991). During the Late Triassic, the Kara Sea Region east in the Barents Sea was uplifted and eroded, leading to a more westward progradation of the Barents Sea delta (Smelror et al., 2009). Worsley (2008) addresses that the channel and coastal sandstone from the Finnmark Platform and Nordkapp Basin display a more mature textures and better reservoir properties than the surrounding northern areas. This most likely due to the sediments being sourced from the Baltic shield and reworked during times of highstand.

The clastic sedimentation continued into the Jurassic All over the western Barents Sea a continuous layer of early to middle Jurassic deposits can be found as an erosive unconformity. Uplift of the Novaya Zemlya and Pay-Khoy acted as sources during the latest Triassic to Early Jurassic (Gilmullina et al., 2020). The sediments were mainly derived from Fennoscandian with low sedimentation rates (Ryseth, 2014; Eide et al., 2018). Late Jurassic rifting occurs on the



Loppa High and the Hammerfest and Nordkapp basins. During the late Mesozoic, a period of major structural changes occurred. This is one of two periods in post-Triassic times that has highly formed the present structure of the Barents Sea (Faleide et al., 1993). Sediments from the latest Triassic Snadd Fm at Loppa High has been eroded as a consequence rifting in post-depositional times (Klausen et al., 2014)

During the Cenozoic, rifting occurred at the western margin due to sea floor spreading in the Atlantic Ocean. Furthermore, this resulted in the separation of the Svalbard Archipelago and Greenland (Klausen et al., 2014). The Barents Sea region has been affected by a two-stage opening of the Norwegian-Greenland Sea. Progressively rifting of Greenland in a northward direction led to shearing of the passive continental Barents Sea margin. Following, the continental break-up led to the onset of sea floor spreading in the present Atlantic ocean (Faleide et al., 1984). The base Cretaceous unconformity marks the change in sedimentological deposition going from Cretaceous to early Cenozoic (Gac et al., 2018). The Barents Sea went through several repetitions of episodic uplift and erosion (Dorè, 1992). This led to large-scale tilting of crustal blocks in a north-south direction (Glørstad-Clark et al., 2011), which was followed by repetition of glacial periods in the later periods (Lasabuda et al., 2021)



**Figure 2.6:** Paleogeographic reconstruction of Late Triassic (A) to Early Tertiary (B) continental drift. The Barents Sea area moved from a position at around 50 °N, to more arctic climate at around 70 °N. Rifting of the super continent Pangea, forming new continents and formation of new oceans. Rifting of the of the Atlantic Ocean culminating into sea floor spreading occurs during this period. Modified from Smelror et al. (2009).

### 3 THEORETICAL BACKGROUND

---

#### 3.1 Detrital zircon geochronology

Detrital zircon geochronology of siliciclastic sediments is a widely used method for source-to-sink studies. The physical and chemical characteristics of zircons make them resistant to geological processes like erosion, transport, metamorphism, and volcanism which makes them abundant in mostly all sedimentary archives (Fedó et al., 2003). The properties of zircon make it suitable for geochronological analysis and rapid single-grain U-Pb and Th-U isotope analyses. Studies for determining sandstone provenance has gained popularity over the years (Vermeesch, 2018), and is helpful for determining e.g., possible source of sediments and depositional patterns (Morton, 1991).

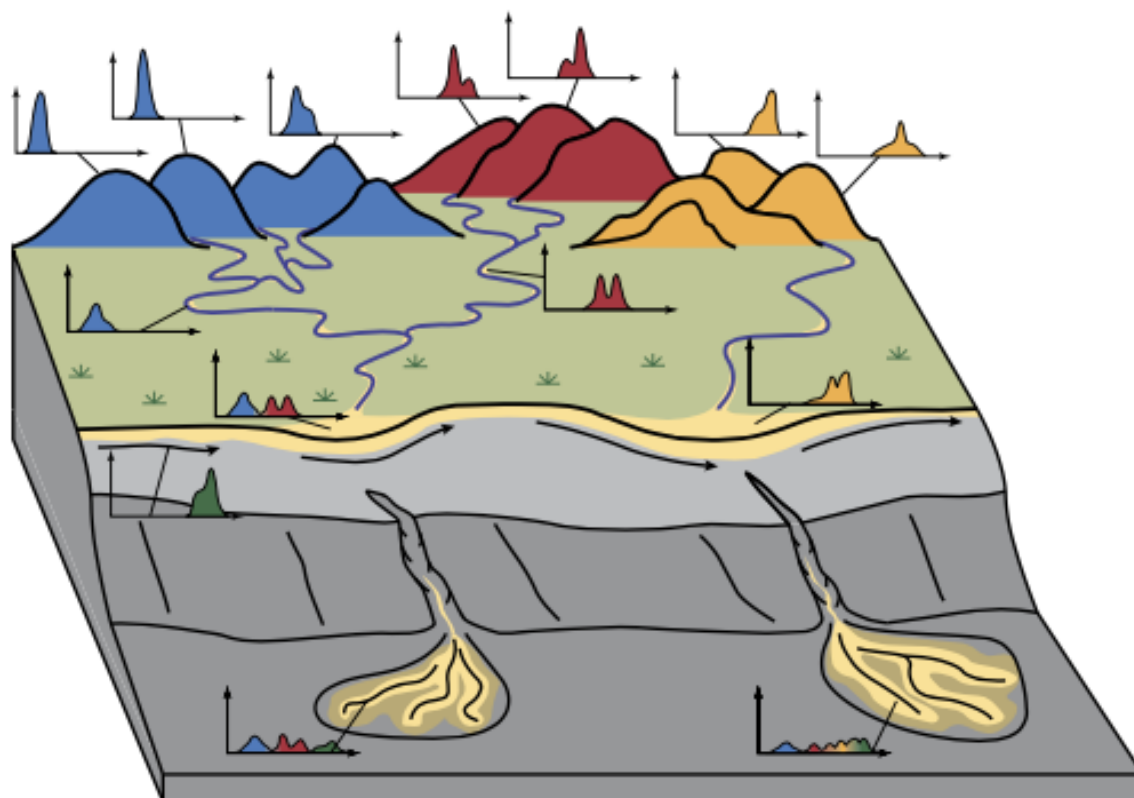
Minerals with a density higher than  $2.80 \text{ g/cm}^3$  are often referred to as heavy minerals. Zircon ( $\rho = 4.60 - 4.70 \text{ g/cm}^3$ ) is one of them and is commonly found in sedimentary rocks, and because of its refractory characteristics is often used for geochronological dating. Zircon consists of zircon (Zr) and silicate ( $\text{SiO}_4$ ), and it is categorized as a nesosilicate. It follows the zirconium-hafnium solid solutions series, hosts long-lived isotopes of uranium (U) and thorium (Th), and components of rare-earth mineral (REE; Morton, 1991). The latter isotopes decay into different types of lead (Pb), which is essential for the geochronology of zircon. Three systems decay simultaneously into Pb, each with a different half-life: (i)  $^{238}\text{U} \rightarrow ^{206}\text{Pb}$  (half-life: 4.47 Ga), (ii)  $^{235}\text{U} \rightarrow ^{207}\text{Pb}$  (half-life: 707 Ma), and (iii)  $^{232}\text{Th} \rightarrow ^{208}\text{Pb}$  (half-life: 13 Ga). Having three chronometers with different half-lives gives the opportunity to detect/record processes that affect the isotopic ratios of the zircons (e.g., metamorphism/Pb-loss). This will cause a bias on the measured ages. By comparing the different isotopic ages, the degree of concordance can be calculated (Andersen et al., 2019). None or minimal amounts of Pb is present in zircons originally, meaning that the measured amount must originate from the decay of U or Th. The relation between the different U isotopes is constant, making it possible to measure the relationship between the three different decay systems. Zircons have the ability to preserve the isotopic amount of U and Th, and the radiogenic amount of Pb during heating up to *c.*  $900 \text{ }^\circ\text{C}$  (Davis et al., 2018), under this temperature zircons will stay undifferentiated (Lee et al., 1997).

Provenance studies use the calculated age and isotopic signatures in comparison to known source area signatures, combined with other approaches, e.g., sequence stratigraphy, tectonic studies mineralogy, sedimentology, or seismic (Haughton et al., 1991).

Possible zircon recycling must be taken into account as exhumed deposits containing zircons may be eroded and redeposited resulting in mixed patterns of zircon sources (Johnson et al., 2018). The importance of understanding the sorting of zircons in distributive fluvial systems is therefore key in detrital provenance studies.

### 3.2 Fluvial aspect of detrital zircon provenance

Provenance studies address multiple techniques (mentioned above) to obtain information on the source of origin. Sedimentological provenance is complex and must be substantiated with other studies. Provenance studies aim to reconstruct the dispersal pathways and ancient sediment transport systems, often with the goal to predict sand properties or to infer geodynamic evolution of the source region. Hence, understanding distributive fluvial systems and sorting is essential to map provenance sources. Primarily, fluvial systems compile and transport sediments towards marine or lacustrine basins (Galloway and Hobday, 1996).



**Figure 3.1:** Hypothetical dispersal of four sediment sources with different density plots in the colours green, blue, red, and yellow. The age distribution plots of the deposited sediments show how the detrital zircon age distributions can be affected during the transport from source to sink. Collected from Sharman & Johnstone (2017).

Fluvial systems can highly affect the distribution pattern of zircon age spectra, by combining diluting or sorting of different populations (Fig. 3.1). Depending on the sampling area, the age spectra may be significantly different from place to place. Subsurface samples have a high probability of being mixed with other sources due to the long transport distance (Sharman and Johnstone, 2017). Samples collected close to the source area will mainly show unmixed age spectra as they are close to the source (Fig. 3.1).

Fluvial systems vary over time in size, strength, and sediment transport, and its physiographic effect on sorting is minimal addressed. Transported material tends to be sorted by size while the shape is affectively important as well, but depending on size (Powell, 1998; Carling et al., 1992). Hydrodynamic parameters (e.g., turbulence, depth, and flow velocity) can influence the mineralogical and chemical compositions of the fluvial detritus during transport and deposition. Density is an important factor for mineral sorting and thus affects the sorting of detrital zircons. The physical properties of alluvial material during erosion, transport, and deposition lead to distinct patterns in material segregation (Powell, 1998). According to Ibañez-Mejia et al. (2018), there are two issues connected to provenance applying sediment geochronology to fluvial systems. The first issue is that detrital zircon ages may cluster by grain size (Garzanti et al., 2009; Lawrence et al., 2011; Sircombe et al., 2001). The second one is that sorting of grain size is affected by the dynamics of sediment transport (Hajek et al., 2010; Udden, 1914). The appearance of zircons in fluvial sedimentary systems deriving from different sources may be due to physical properties at different times and therefore require a broad sampling collection. A challenge is to obtain biases on the sedimentological record of the detrital zircon.

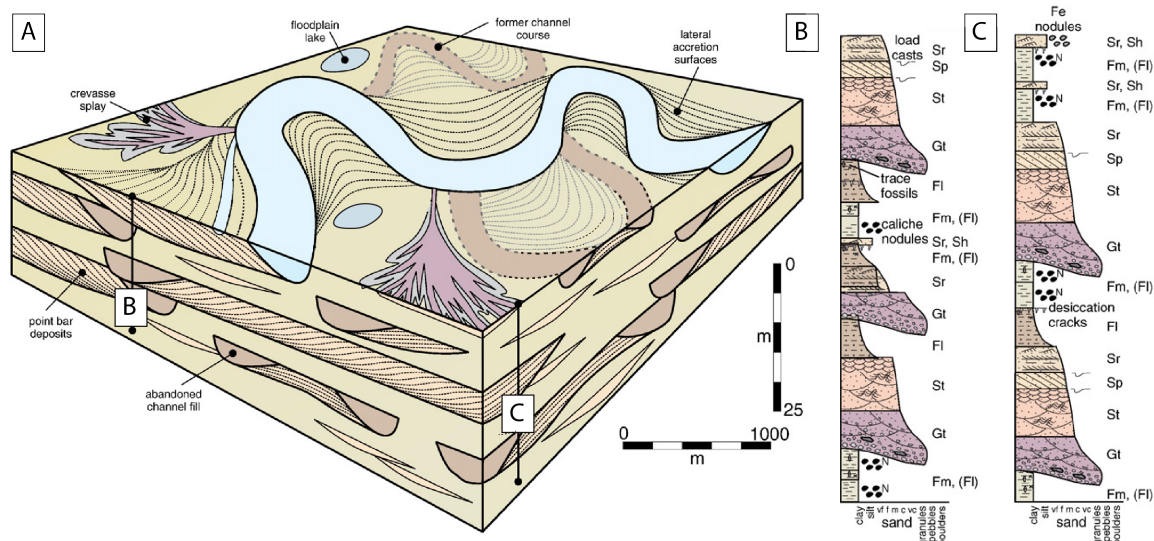
### 3.3 Distributive fluvial systems

Distributive fluvial systems (DFSS) transport alluvial material in areas close to or within mountain areas and form differently depending on surrounding environments. Parameters like tectonic, climate, gradient, sediment supply, and planform termination type affect the physiography and type of river systems that form individually or combined (Hartley et al., 2010). With the large drainage area of the Uralian Mountain Belt, such DFSSs formed on the delta plain that was deposited in the Barents Sea during Triassic times (Klausen et al., 2019). In the proximal area, large amounts of water and sediment formed meandering river systems that migrated across the plain while more braided systems were formed in the distal part (Klausen et al., 2014).

Migrating meandering rivers eroded and deposited fluvial material on the delta plain (Skjold et al., 1998). The thickness/width relationship changed distally, in which the meandering bodies can migrate several kilometres laterally, while the thicknesses are limited to tens of metres.

During migration cycles, the meandering river will form a distinct set of features (Fig. 3.2; Durkin et al., 2017), these can be recognized in situ systems, in seismic models, sedimentological cores, and outcrops. Over time the system will vertically stack a set of features (Figs. 3.2B and C), creating a repetitive succession of coarsening upwards gravel beds, cross-bedded and laminated sands, and massive and laminated finer material (Collinson, 2019). The sedimentary structure and grain size reflect the energy level of the different levels of the meandering river, the highest energy at the bottom gravel base, and a decrease upwards with the sandstone bodies. The uppermost fine clay deposits represent the lowest energy elements, the floodplain and levee deposits (Ghazi and Mountney, 2009).

Migration of the meandering turns varies widely according e.g., the environment it erodes in and the distance from drainage and depositional area. From an alluvial segment of the Mississippi River, proximal measurements show meandering turns of an average of *c.* 59.1 m/year (Hudson and Kesel, 2000). This system is similar to the one in the Barents Sea, and the measurements are collected from several turns in the proximal area.



**Figure 3.2:** Key features of meandering river systems. A) 3D overview of a meandering turn and the succession of elements that stack upwards. B) and C) show sedimentary logs, representing the depositional sequences and facies occurring through the two cored sections. Modified from Ghazi & Mountney (2009).



## 4 METHODS AND DATA

---

### 4.1 Sampled collection

20 samples (BAR-69 to BAR-88, Tab. 4.1) were acquired from well 7131/4-1 at the Norwegian Petroleum Directorate the 4<sup>th</sup> of January 2021 (Appendix I). These were acquired by breaking off pieces by hand, hammer, or sawing. Samples from all relevant facies were collected from the interval 1070.00 m to 1117.89 m, belonging to the Snadd Fm. In agreement with NPD, total sample weight could not exceed a total of 700 g, thus each sample weighs  $\sim 35 \pm 1 - 2$  g. A piece of every sample was cut off for thin section epoxy mounts leaving the rest of the samples for zircon geochronology (Fig. 4.2A). Preparation and analyses were executed at the labs of the Mathematics and Natural Sciences Faculty at the University of Bergen.

These initial 20 samples were used to develop a model for zircon fertility and zircon-age-sorting in the studied channel. Samples from all facies were collected and variability in fertility and age-sorting was investigated and evaluated. A second model was developed, explaining the variability, and predicting that certain facies would contain many zircons and other few zircons. Seven additional samples were acquired on the 3<sup>rd</sup> of November to test the model that was developed. These samples were treated the same way as the initial samples and considered according to the predicting model.

### 4.2 Sample Preparation

#### 4.2.1 Mineral separation

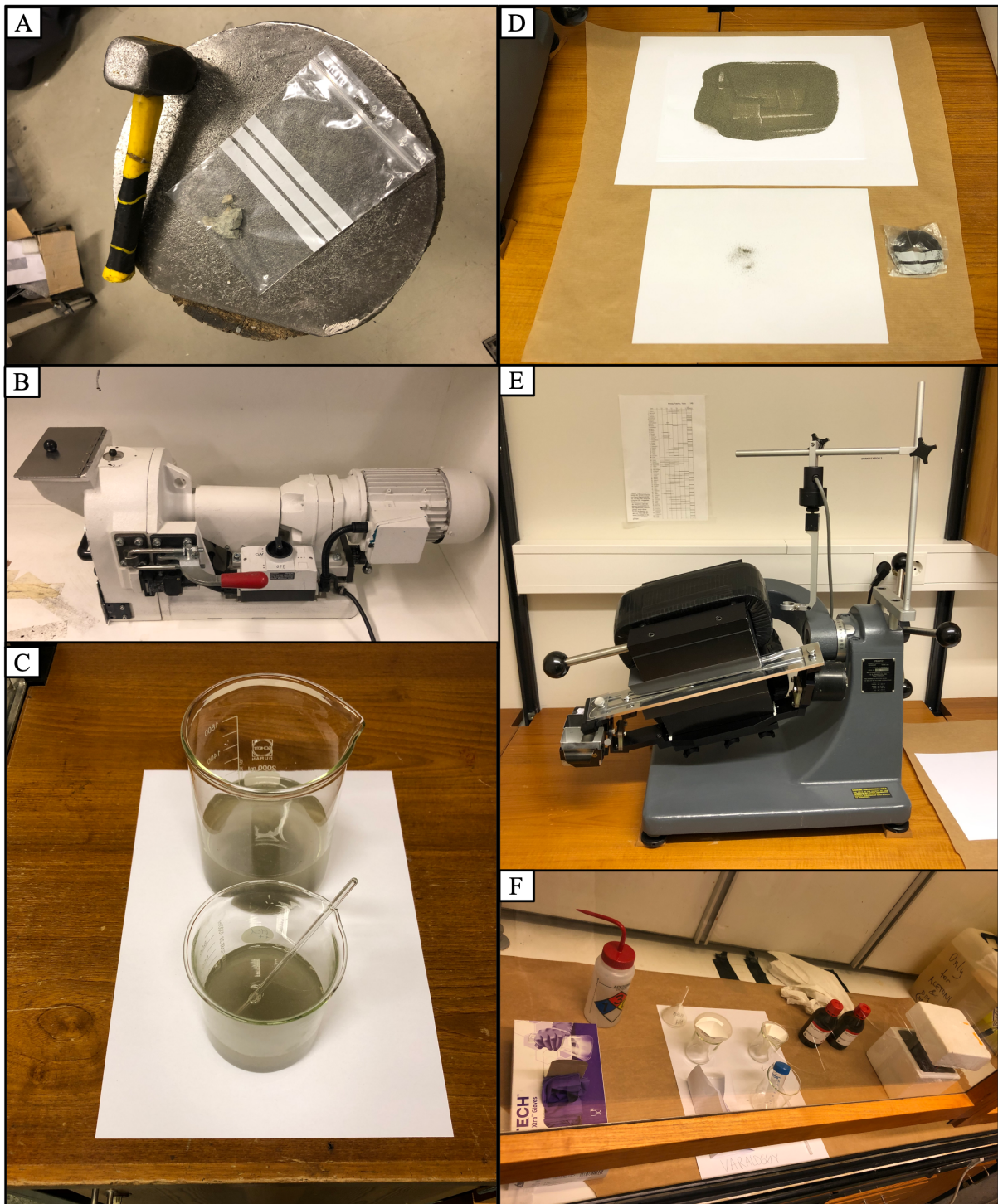
The samples for zircon geochronology were crushed by hand and fed in the pulverizing Fritsch Pulverisette 13 discmill to a grain size  $< 315$  micrometre ( $\mu\text{m}$ ), which is common for zircon grains (Fig. 4.1B). Samples were sieved in between to remove particles  $> 315$   $\mu\text{m}$ , then washed in one L beakers leaving the heavy minerals to be further separated (Fig. 4.1C).

The heavy mineral fraction was further brought to the Frantz magnetic separator where ferromagnetic minerals were removed by a handheld magnet initially (Fig. 4.1D). The remaining material was poured on to the tilted tray holding a sideways and forward tilt of  $15^\circ$  (Fig. 4.1E) and five increasing currents were applied (0.2, 0.5, 0.7, 1.0, and 1.2 A). The separated fractions were poured into conical tubes (Fig. 4.1F) filled with 100 ml of diiodomethane (DIM) with a density of  $3.32 \text{ g/cm}^3$ .

The density of the heavy liquid lets the zircons ( $\rho = 4.60 - 4.70 \text{ g/cm}^3$ ) sink, while lighter minerals, such as apatite ( $\rho = 3.10 - 3.20 \text{ g/cm}^3$ ), will float on top. Freezing the bottom of the conical tube with liquid nitrogen ( $c. -210 \text{ }^\circ\text{C}$ ) lets the DIM freeze and the upper part stay liquid. The liquid DIM can be poured out into one beaker with a funnel and filter paper. The frozen bottom plug “popsicle” melts and can be poured into another beaker with funnel and filter paper (Simpson et al., 2012). Both filters were then rinsed with acetone and sealed with paper clips.

**Table 4.1:** Overview of BAR-sample information, depth in core 7131/4-1, weight of samples from the core, LAS-number, mount position, number of zircons in the samples and number of zircons per gram of sample. An additional number of samples was collected during a second stay at NPD and can be viewed at the bottom, after the first sample collection at NPD. These samples were only picked and counted.

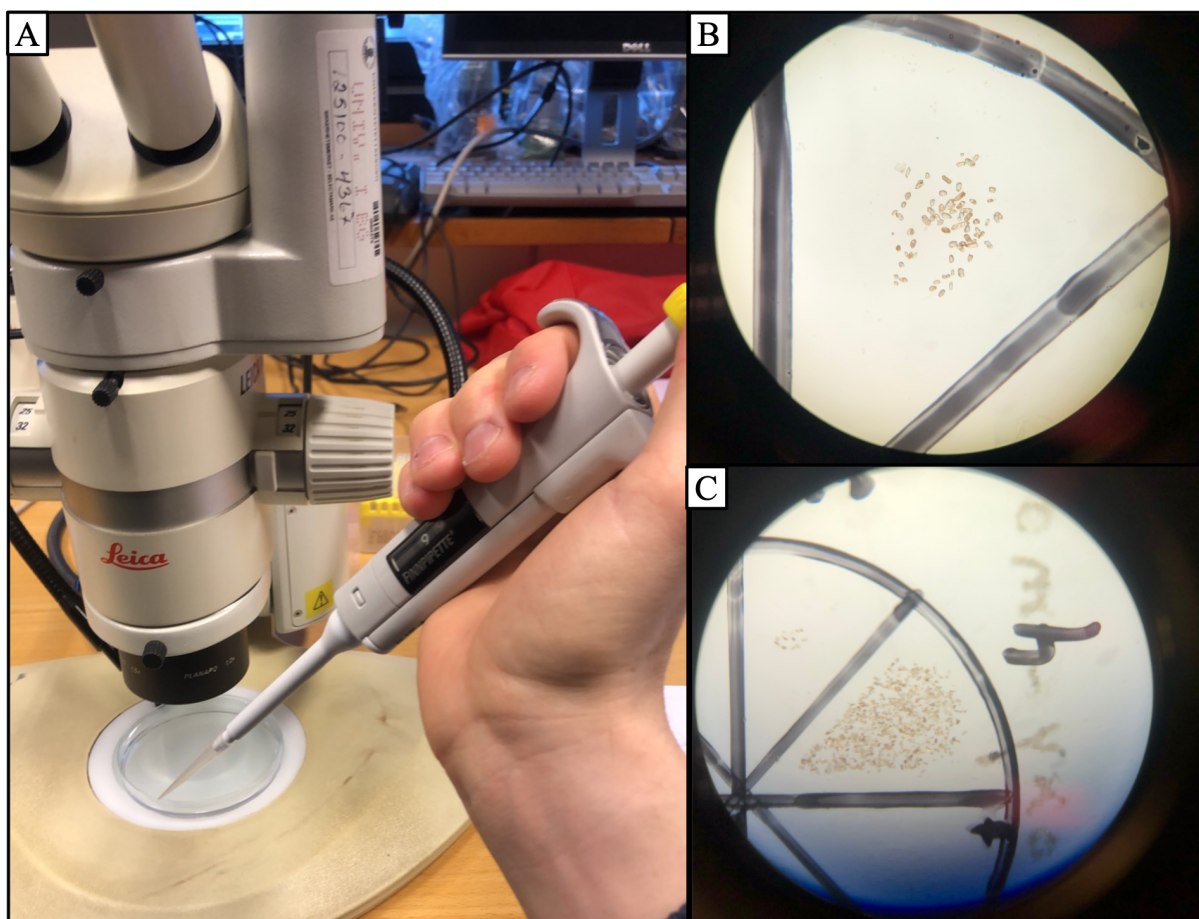
| <b>Initial samples to develop model</b>      |                  |                   |                   |              |                    |               |
|--|------------------|-------------------|-------------------|--------------|--------------------|---------------|
| <b>Sample name</b>                           | <b>Depth (m)</b> | <b>Weight (g)</b> | <b>LAS-number</b> | <b>Mount</b> | <b>n (n dated)</b> | <b>n/gram</b> |
| <b>BAR-69</b>                                | 1070.00          | 35                | LAS412_3          | M1P2         | 8 (8)              | 0.23          |
| <b>BAR-70</b>                                | 1074.80          | 34                | LAS412_2          | M1P1         | 21 (27)            | 0.62          |
| <b>BAR-71</b>                                | 1079.35          | 35                | LAS412_4          | M1P3         | 14 (14)            | 0.4           |
| <b>BAR-72</b>                                | 1080.10          | 32                | LAS412_5          | M1P4         | 501(535)           | 15.65         |
| <b>BAR-73</b>                                | 1084.80          | 36                | LAS412_6          | M1P5         | 37 (38)            | 1.03          |
| <b>BAR-74</b>                                | 1088.45          | 35                | LAS412_7          | M1P6         | 11 (11)            | 0.31          |
| <b>BAR-75</b>                                | 1088.70          | 35                | n/a               | n/a          | 0                  | n/a           |
| <b>BAR-76</b>                                | 1089.75          | 33                | LAS412_1          | M1P8         | 58 (61)            | 1.75          |
| <b>BAR-77</b>                                | 1093.85          | 35                | LAS411_4          | M2P2         | 61 (67)            | 1.74          |
| <b>BAR-78</b>                                | 1093.92          | 36                | LAS411_5          | M2P3         | 57 (67)            | 1.58          |
| <b>BAR-79</b>                                | 1099.75          | 35                | LAS411_6          | M2P4         | 67 (69)            | 1.91          |
| <b>BAR-80</b>                                | 1100.77          | 34                | LAS411_3          | M2P1         | 5 (5)              | 0.14          |
| <b>BAR-81</b>                                | 1101.92          | 37                | LAS411_7          | M2P5         | 13 (13)            | 0.35          |
| <b>BAR-82</b>                                | 1106.40          | 37                | LAS411_8          | M2P6         | 164 (170)          | 4.43          |
| <b>BAR-83</b>                                | 1108.55          | 36                | LAS411_1          | M2P7         | 54 (57)            | 1.54          |
| <b>BAR-84</b>                                | 1111.30          | 35                | LAS411_2          | M2P8         | 5 (5)              | 0.14          |
| <b>BAR-85</b>                                | 1112.25          | 35                | LAS413_1          | M3P1         | 40 (42)            | 1.14          |
| <b>BAR-86</b>                                | 1112.65          | 35                | LAS413_2          | M3P2         | 145 (145)          | 4.14          |
| <b>BAR-87</b>                                | 1112.93          | 35                | LAS413_3          | M3P3         | 88 (93)            | 2.5           |
| <b>BAR-88</b>                                | 1116.85          | 35                | n/a               | n/a          | 0                  | n/a           |
| <b>Additional samples to test hypothesis</b> |                  |                   |                   |              |                    |               |
| <b>BAR-89</b>                                | 1080.1           | 17                | n/a               | n/a          | 110 (sand)         | 6.47          |
| <b>BAR-90</b>                                | 1080.1           | 35                | n/a               | n/a          | 7 (mud clast)      | 0.2           |
| <b>BAR-91</b>                                | 1080.1           | 13                | n/a               | n/a          | 22 (sand)          | 1.69          |
| <b>BAR-92</b>                                | 1101.3           | 32                | n/a               | n/a          | 49 (drape)         | 1.53          |
| <b>BAR-93</b>                                | 1103.2           | 10                | n/a               | n/a          | 0 (clast)          | 0             |
| <b>BAR-94</b>                                | 1103.2           | 12                | n/a               | n/a          | 42 (sand)          | 3.5           |
| <b>BAR-95</b>                                | 1103.3           | 15                | n/a               | n/a          | 3 (siderite)       | 0.2           |



**Figure 4.1:** The different steps in mineral separation. A) Samples crushed with hammer or by breaking of by hand. B) The Fritsch Pulverisette discmill 13 grinds up the material in fractions  $<315 \mu\text{m}$ . C) Samples washed repetitively in beakers to keep as much material as possible. D) Handheld magnet removed the ferromagnetic minerals. E) Magnetic separation with the Frantz magnetic separator. F) Popsicle method, separation of zircons with DIM heavy liquid.

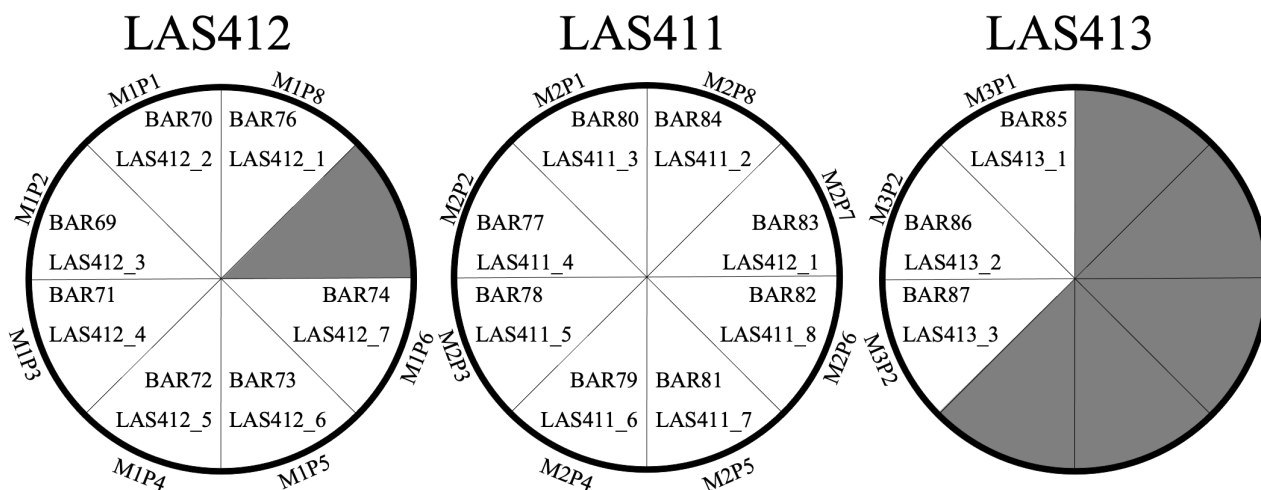
### 4.2.2 Preparation of zircon mounts

Further, the material was handpicked under a Leica loupe in petri dishes filled with ethanol and moved to glass plates with a pipette (Fig. 4.2A). The grains were organized in a “pizza slice”-system (Figs. 4.2B, C, and 4.3), each sample filling a piece with grains. Even though the samples contained variable amounts of detrital zircon from less than ten to several hundred of grains, all recognizable, pickable grains were picked in each sample since determining the amount of zircon per samples is a major goal on the study. Epoxy resin was then poured into the circular mount, followed by manually grinding with SIKA powder with 800  $\mu\text{m}$ , 1000  $\mu\text{m}$  and 1200  $\mu\text{m}$ , and at last, polished with a diamond paste of 6  $\mu\text{m}$  and an aluminium oxide powder of 0.5  $\mu\text{m}$ . The objective of the grinding is to expose the core of the zircon grains so that they can be analysed.



**Figure 4.2:** A) photo of the Leica loupe with the petri dish containing zircons grains under and the pipette that is used for moving the zircon grains to the glass plate. B) and C) photo of sample BAR-72 and BAR-78 with the picked zircon grains in “pizza slice” -system. All the assumed zircon grains were picked for fertility analysis.





**Figure 4.3:** Zircon mounts system, three mounts were filled with zircon grains in a "pizza slice" -system. BAR-name in ascending order indicates the samples names from well 7131/4-1 in downward order. LAS-names are from analyses in LA-ICP-MS. 18 of 20 samples contained zircon grains to be analysed.

### 4.3 CL and BS imaging

Magmatic and/or metamorphic events may cause differences in element composition which results in zonation patterns (Connelly, 2001). Brighter areas have a relatively low amount of uranium and yttrium, while darker areas are richer in these (Rubatto and Gebauer, 2000). To map the internal structures imaging of zircon grains, cathodoluminescence (CL) and backscatter (BS) imaging was conducted using a Zeiss Supra 55VP Scanning electron microscope (SEM) with a CL- and BS detector connected. Carbon coating was added initially to obtain conductivity before imaging with a working distance of 15.7 mm and power of 15 kV. Atlas software (v. 4.1) was used for mosaic picturing which is favourable for mapping zonation patterns and inclusions which are to be avoided during LA-ICP-MS analysis.

### 4.4 LA-ICP-MS

Three epoxy mounts (Fig. 4.3) containing 18 sample slices with zircon grains were analysed by laser ablation-inductively coupled plasma-mass spectrometry (LA-ICP-MS). Initially, the mounts were washed with five %  $\text{HNO}_3$  followed by an ultrasonic bath in de-ionized water to remove any surface containments that can affect the result. U-Pb zircon analysis was done using a 193 nm ArF excimer laser ablation system (RESOLUTION M-50 LR) connected to an HR-SC-ICP-MS (Nu Instruments Attom ES). Complete parameter overview is found in Appendix II. The laser ran repetitive rounds of 20 analyses. Starting with six analysis of zircon standards, followed by 14 analyses of samples (BAR-69 to BAR-88). During the run, zircons were ablated for 30 s, followed by 15 s of blank measurement. The laser was fired with a repetition rate of

five Hz and with a fluence of 2-2.5 J/cm<sup>2</sup>. A spot size of 26 μm was applied. Sample data was collected in time resolved peak-jumping pulse-counting mode with one point measured per peak for masses <sup>202</sup>Hg + <sup>204</sup>Pb + <sup>204</sup>Hg, <sup>206</sup>Pb, <sup>207</sup>Pb, <sup>208</sup>Pb, <sup>232</sup>Th, <sup>235</sup>U, and <sup>238</sup>U. Due to the non-linear transition between the two detector modes in the ICP-MS, <sup>238</sup>U was calculated from <sup>235</sup>U when measured in attenuated mode (> 2 000 000 counts, <sup>238</sup>U = <sup>235</sup>U counts x 137.818) using a purpose-made python script. If measured in counting mode, the data was left unchanged (Bjerga et al., 2021). U-Pb data can be viewed in Appendix III.

#### 4.5 Data processing

Reduction of data was done using Iolite 4 (v. 4.4.5) with VizualAge UComPbine data reduction scheme. Data reduction methods follow Paton et al. (2010), which includes gas blank correction, laser-induced elemental fractionation of U and Pb, and instrument mass bias. Blank counts and instrumental biases were corrected with an automatic spline function, while down-hole element fractionation was corrected using an exponential or exponential + line function. A correction was not needed for common Pb, only monitored. Remaining element fractionation and instrumental mass bias were corrected by normalization to the natural zircon reference material 91500 (1065 Ma - Wiedenbeck et al., 1995), GJ-1 (609 - Jackson et al., 2004) and Plešovice (337 Ma - Sláma et al., 2008) was used for quality control. With mean ages of 1066.5 ± 27.8, 604.4 ± 13.7 and 344.8 ± 9.9 Ma, respectively. DetritalPy (Sharman et al., 2018) was used to process, plot and compare the U-Pb datasets.

#### 4.6 Seismic dataset

Seismic figures are interpreted from the Guovca dataset located at the Finnmark Platform, survey number ST9802, with well 7131/4-1 being the only well penetrating the Snadd Fm with a thickness of 242 m. The seismic cube consists of high quality seismic continuous to discontinuous reflectors. The cube comprises *c.* 1900 m<sup>2</sup>, but only 1500 m<sup>2</sup> is available for interpretation. Petrel (by Schlumberger, v. 2019.3) was used for interpretation of horizons and creation of attribute surfaces. Top Kobbe, Top Snadd, and early Carnian surfaces were interpreted with seeded auto tracking along inlines, and crosslines was used for guidance. The seismic model will help us viewing the architecture of the meandering point bar, and potentially let us measure the proportions of it.

## 5 RESULTS

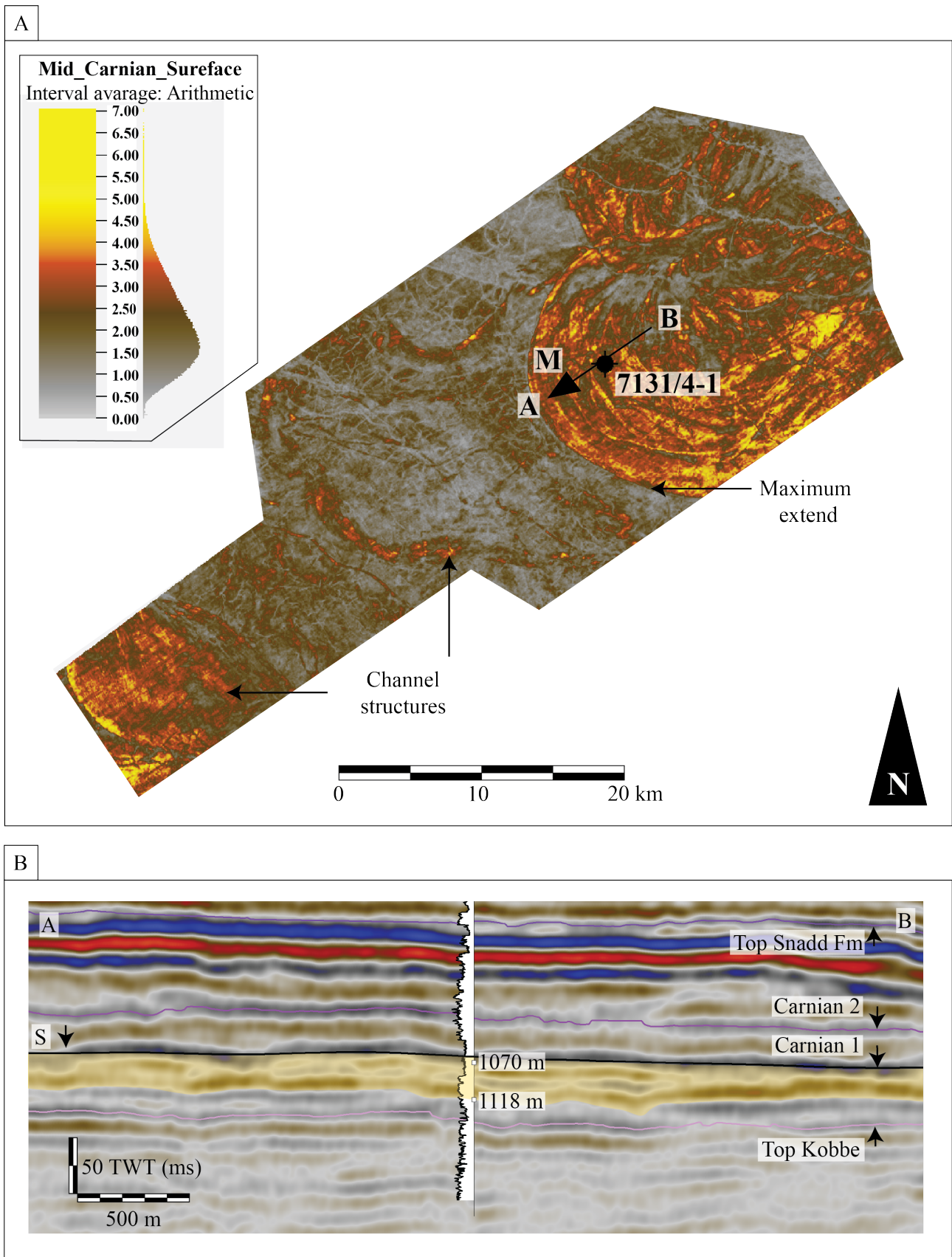
---

The following chapters present the results from the analysis of the dataset from the large scale to small scale. Firstly, the analysis of the Guovca channel in 3D seismic is presented, followed by a detailed facies analysis of the interpreted channel deposits displayed in well 7131/4-1. Further, the fertility of the collected core samples will be presented, and a description of the spectra from the zircon geochronology results. Finally, measurements from SEM- images of zircon size and petrological observations of thin sections are presented at the end.

### 5.1 Analysis of the Guovca channel in 3D seismic data

All over the Greater Barents Sea Basin, seismic reflection data have documented Triassic River deposits, especially the river systems that prograde westwards from the Uralian provenance area (Gilmullina et al., 2021; Gac et al., 2018; Eide et al., 2018; Klausen et al., 2015; Henriksen et al., 2011; Nøttvedt et al., 1993). It is highly wanted to understand the constrain of various sediment sources in the Barents Sea as they have various hydrocarbon potential, which are highly associated with the provenance (Mørk, 1999; Henriksen et al., 2011). Seismic images of the Guovca point bar has earlier been presented in this seismic cube (Klausen et al., 2014; Klausen et al., 2015).

Seismic horizons close to the cored interval were interpreted as early Carnian. Top Snadd and Top Kobbe were also interpreted. The seismic is of high quality and displays continuous to discontinuous low and high amplitude reflectors. In the southwestern and northeastern corners, the seismic is highly discontinuous because of faulting. Discontinuous to continuous wavy reflectors with low amplitude is often observed in the early Carnian interval, both in C1 and C2. These wavy reflectors display wide sandstone channels bodies (below C1, Fig. 5.1A). A high amplitude reflector is present in what seems to be the surface of the river (S, Fig. 5.1A), while the bodies show a low amplitude (cross-section A – B, Fig. 5.1B). Migration direction is marked with an arrow (M, Fig. 5.1A), as well as the maximum extent of the meandering turn. The 48 m interval cored in this thesis shows only channel deposits, and it is therefore unknown if the channel body-thickens is larger than the interval. The seismic indicates that the river surface is a few meters above the top of the interval. The exact depth of the river has not been measured, but *c.* 58 m is measured by Klausen et al. (2015), and the width of the channel body ranges for *c.* 20 km.



**Figure 5.1:** A) RMS- amplitude map of a large meandering point bar deposit (orange coloured) visible in the early Carnian (C1) with well 7131/4-1 penetrating the formations. Smaller channel structures are visible in the western- and middle parts of the map. The seismic cross-section (A-B) is visible as figure B), M indicated the migration direction and maximum extent is also highlighted. B) Cross-section of the meandering point bar, it is displayed as wavy discontinuous to continuous reflectors. Surface (S) marks the position of the map in A).



RMS-amplitude maps (Fig. 5.1A) highlights geological structures such as the early Carnian channel sandstone bodies. Distinct meandering point bar structures are visible from these maps (Fig. 5.1), showing large meandering turns that represent the lateral accretionary surfaces that are deposited over time as the river migrates. Orange-yellow areas reflect river deposits and grey areas reflect the delta plain that formed from the eastern areas which the rivers eroded in. Such large river bodies are constrained to the proximal parts, large turns like those present rarely occur in distal areas where detrital material is deposited (Klausen et al., 2015). Meandering turns like this are not present in many catchment areas, but from the lower Mississippi river migration rates of *c.* 59.1 m/year are present, indicating a depositional time of around 300 years.

## 5.2 Sedimentological analysis of the Guovca channel core

### 5.2.1 Facies description

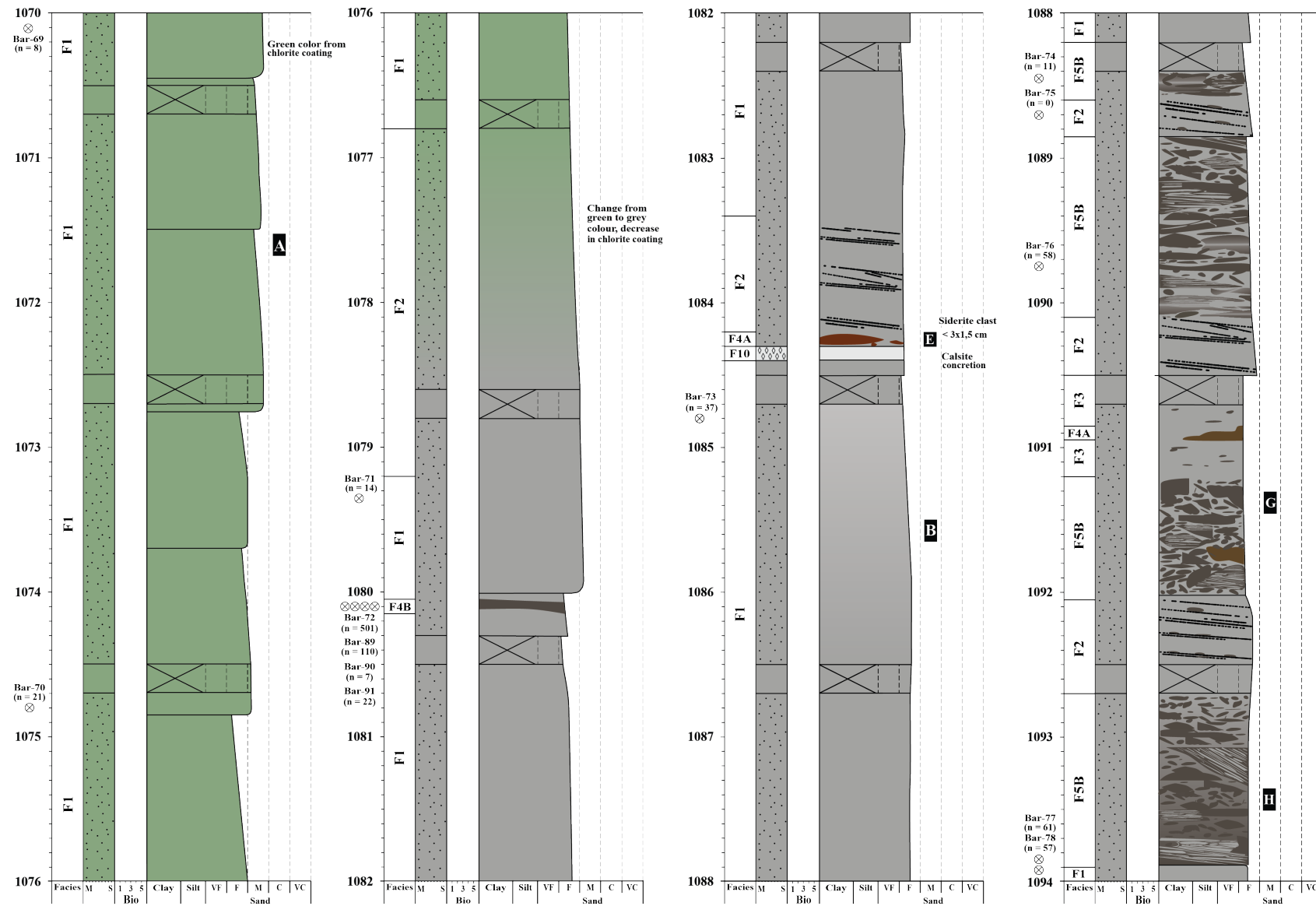
The meandering point bar deposit interpreted from 3D seismic data is penetrated by well 7131/4-1, and through detailed core analysis of this well ten facies and four sub-facies can be identified (Tab. 5.1). This large amount of facies is necessary to characterize the flow conditions at the time of the deposition and their effect on detrital zircon fertility. The cored interval can be divided into sandstone facies (**Facies F1 – F6**), mudstone facies (**Facies F7 – F9**) and overprinting facies (**Facies F10**), in which **Facies F7 – F10** are in the lower part of the core (Figs. 5.2 and 5.3; Tab. 5.1). Explanation of log is displayed in Fig. 5.4.

**Facies F1** (Figs. 5.5A and B) occur mainly in the upper part of the cored interval as very fine- to medium-grained, homogenous sandstone bodies, and as thinner bodies in between the other facies. The structureless sandstone has a green colour due to chlorite content in the upper eight metres but changes into a grey colour as the chlorite content decreases. Occasionally, organic fragments are visible (< 2 mm), and the facies thickness varies from 0.05 – 6.8 m. The very fine- to fine-grained sandstone also occurs with mud drapes, both as single and multiple mud drapes (**Facies F2**; Fig. 5.5C). The mud drapes are oriented horizontally and tilted in both directions and occur as wavy and straight lines. The thickness of this facies ranges from 0.1 – 1.35 m. The very fine- to fine-grained sandstone is visible with intraformational pebbly mud clasts (**Facies F3**; Fig. 5.5D) ranging from 5 – 30 mm in size. The facies thickness is between 0.1 – 2.25 m where the thinnest occur in the middle part of the cored interval and the thickest parts in the lower interval.

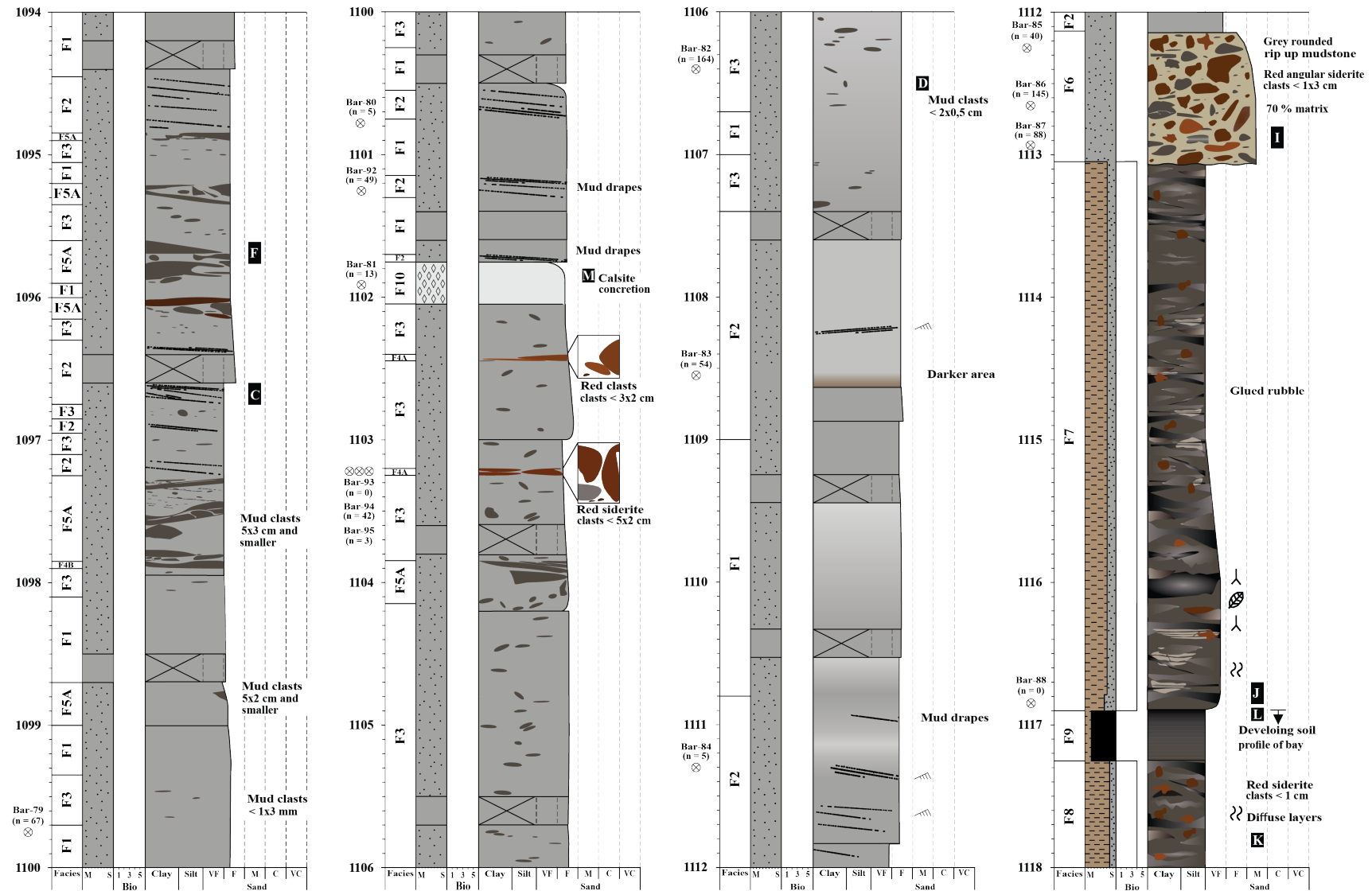
**Table 5.1:** Overview of numbered lithofacies, facies description, thickness, BAR-number to each sample collected from facies, and environment interpretation.

| Facies nr.       | Lithofacies             | Description   | Thickness  | Samples                | Interpretation                            |   |
|------------------|-------------------------|---|--|------------------------|---|---|
| Sandstone facies |                         |   |  |                        |   |   |
| F1               | Structureless sandstone | Very fine- to medium-grained sandstone, occurs mainly in the top of the core, but occasionally in between other facies. Changes in colour from green to grey as chlorite content changes, mainly structureless. | 0.05 – 6.8 m   | 69, 70, 71, 73, 78, 79 | Relatively stable flow in fluvial channel |   |
| F2               | Mud-draped sandstone    | Occurs as very fine- to fine sandstone as thin drapes of mud or tiny organic fragments. Occurs both as individual drapes and stacked draped sand laminae and beds.  | 0.1 – 1.35 m   | 75, 80, 83, 84, 92     | Variable flow in fluvial channel          |   |
| F3               | Pebbly sandstone        | Very fine- to fine sandstone with elongated oval mud clasts with ranging in size from 5x3 – 30x10 mm (pebble). The granule occurs individually, rarely in direct contact.                                       | 0.1 – 2.25 m   | 82                     | Variable flow in fluvial channel          |   |
| F4               | F4A                     | Sandstone with cm-scale red clasts  | Fine to medium sandstone with isolated red clasts in size ranging from one cm (granule) to several cm (pebble). Clasts occur rounded with both low and high sphericity. Some clasts exceed core width, so biggest size is not distinguishable.         | 0.05 – 0.1 m           | 89, 90, 91                                | Channel base/sideritized clasts from paleosol |
|                  | F4B                     | Sandstone with cm-scale grey clasts   | Fine to medium sandstone with isolated grey clasts in size ranging from one cm to several cm (pebble). Clasts occur rounded with both low and high sphericity. Some clasts exceed core width, so biggest size is not distinguishable.                  | 0.05 m                 | 72, 93, 94, 95                            | Channel base                                  |
| F5               | F5A                     | Moderately sorted mud-clast conglomerate  | Very fine- to fine sandstone with intraformational mud clasts, size ranging from mm (granule) to several cm (pebble). Clasts are mainly elongated, with rounded edges, tend to have the longest axis horizontal positioned, and are rarely in contact. | 0.05 – 0.6 m           | None                                      | Channel base                                  |


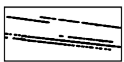

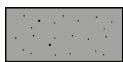










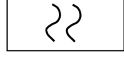

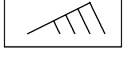
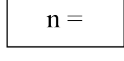
|                     |   |  |              |            |                                   |
|---------------------|---|--|--------------|------------|-----------------------------------|
| F5B                 | Poorly sorted mud-clast conglomerate          | Very fine- to fine sandstone with intraformational mud clasts, size ranging from mm (granule) to several cm (pebble). Clasts are mainly elongated, horizontal aligned, and have rounded edges. It differs from F5A due to the higher number of clasts (granule and pebbles). | 0.05 – 1.2 m | 74, 76, 77 | Channel base                      |
| F6                  | Sandstone with rounded- to angular clasts     | Fine-grained sandstone with both angular red clasts with low sphericity and rounded grey clasts with both low and high sphericity ranging from mm (granule) to cm (pebble) in grain size.  | 0.8 m        | 85, 86, 87 | Channel-lag deposits              |
| Mudstone facies     |   |  |              |            |                                   |
| F7                  | Bioturbated siltstone with red angular clasts | Siltstone containing red irregular clasts and a bioturbation up to degree of four. Red siderite clasts are present.  | 4 m          | 88         | Floodplain/ floodplain lake       |
| F8                  | Bioturbated mudstone with red angular clast   | Mudstone with red irregular red clasts and bioturbation up to a degree of three. Red siderite clasts are present   | 0.8 m        | None       | Floodplain/floodplain lake        |
| F9                  | Coal  | Occurs as a very tiny layer in the lowest part of the core, changes gradual to the underlying siltstone.   | 0.05 m       | None       | Peat/upper organic paleosol layer |
| Overprinting facies |   |  |              |            |                                   |
| F10                 | Calcite concretion                            | Sandstone with precipitation of calcite cement, occurs very fine due to the fine cement that fills the pores.  | 0.05 – 0.3 m | 81         | Paleosol                          |



**Figure 5.2:** Detailed log of core 7131/4-1 (1070–1094 m), with BAR-sample and facies annotated in the left column. Note the sandstone with the varying green colour indicating the change in chlorite content and the isolated clast (1080.1 m) where the sample with highest number of zircons was collected. There is also an abrupt change to more chaotic deposits (1088–1094 m) showing an increase in supply clasts in mixed sizes. Letters in medium sand column are examples from facies (Fig. 5.5).



**Figure 5.3:** Detailed log of core 7131/4-1 (1094–1118 m), with BAR-sample and facies annotated in the left column. Note the end of rapid changing environment to homogenous structureless sandstone without clasts (1107.6 m), the change to channel lag deposits (1112.15 m). There is also an abrupt change to silt- and mudstone at the bottom of the cored interval, containing clasts mud- and siderite clast, and plant fragments (1113.05–1118 m). Letters in medium sand column are examples from facies (Fig. 5.5).

|   |                      |   |                    |   |                      |
|---|----------------------|---|--------------------|---|----------------------|
|  | Sandstone w/chlorite |  | Sandstone          |  | Zircon/petrography   |
|  | Sandstone            |  | Pebbles            |  | Core image of facies |
|  | Silt-/mudstone       |  | Mud clasts         |  | Leaf fragment        |
|  | Calcite              |  | Mud-/rip-up clasts |  | Root structure       |
|  | Coal                 |  | Siderite clasts    |  | Bioturbation         |
|  | Bioturbated mud/silt |  | Current ripples    |  | Concordant zircons   |

**Figure 5.4:** Symbol explanation of sediments, structures, and signs presented in the interpreted core log of well 7131/4-1 (Figs. 5.2 and 5.3). Zircon/petrography samples are presented in section 5.3 – 5.6.

**Facies 4** is divided into two sub-facies: sandstone with cm-scale red siderite clast (**Facies F4A**; Fig. 5.5E) and sandstone with cm-scale grey mud clast (**Facies F4B**; Fig. 5.5F). The clasts occur individually or as a few within the fine- to medium-grained sandstone matrix. The thickness of the facies is equal to the size of the clasts, which ranges from 0.05 – 0.1 m. Occasionally, the clasts exceed core width, thus the maximum clast size is not distinguishable.

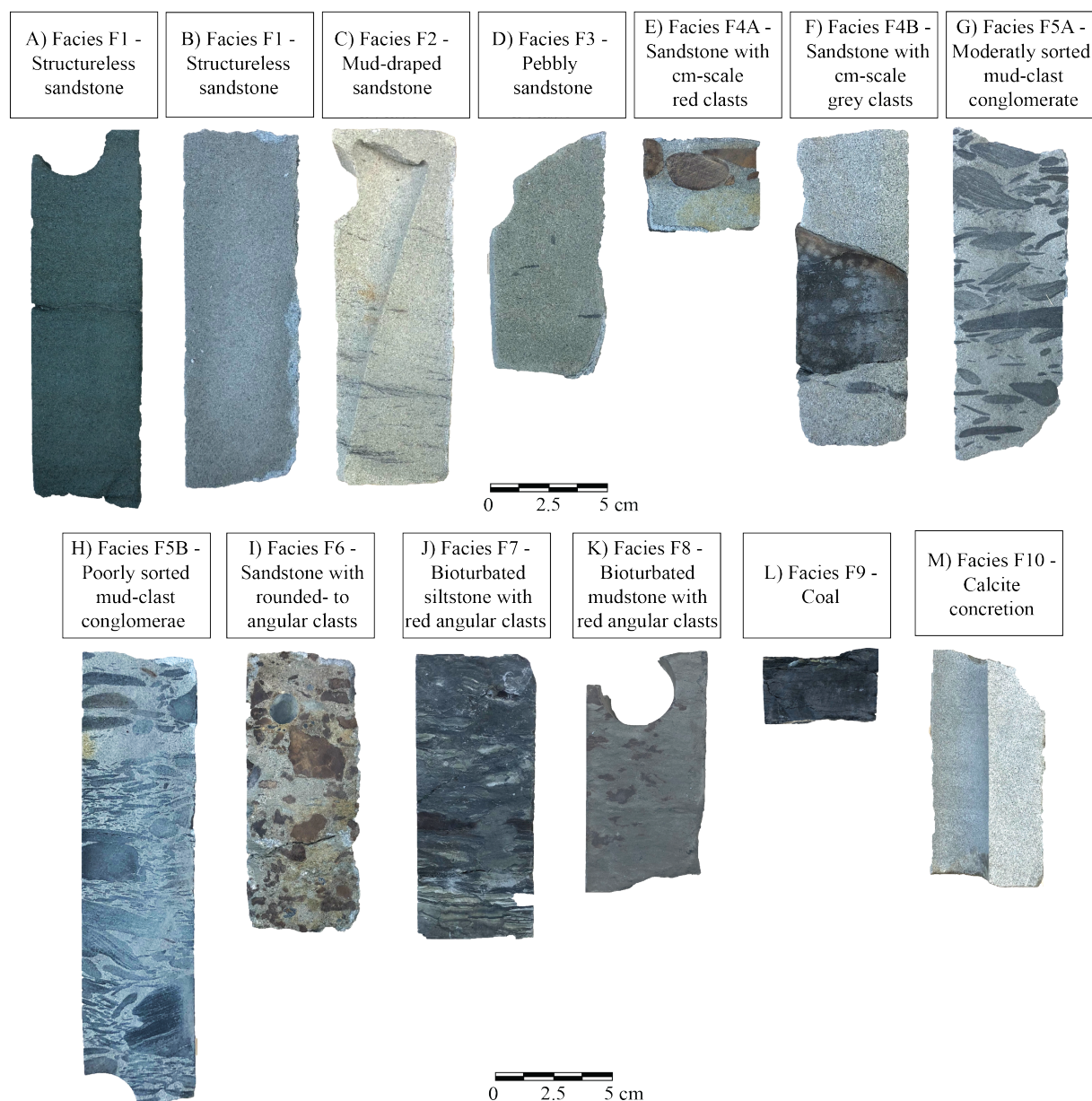
**Facies 5** is also divided into two sub-facies: moderately sorted mud-clast conglomerate (**Facies F5A**; Fig. 5.5G) and poorly sorted mud-clast conglomerate (**Facies F5B**; Fig. 5.5H). The matrix of Facies F5A and F5B consists of very fine- to fine-grained sandstone. The difference between these facies, however, is the amount and size of the clasts. F5A has a lower clasts content than F5B and the clasts vary more in size. F5A occurs matrix supported while F5B is clast supported, and the facies thickness ranges from 0.05 – 0.6 m for the moderately sorted (F5A) and 0.05 – 1.2 m for the poorly sorted (F5B). The clasts in both facies are elongated, lens-shaped, and aligned mostly horizontal (perpendicular to the drilling direction).

The last sandstone facies (**Facies F6**; Fig. 5.5I) host clasts ranging 0.5 to 3 cm, the clasts are rounded to angular shape, red (siderite), and grey (mud clasts) coloured. It is observed as a 0.9 m thick layer at bottom of the cored interval and the do not seem to be aligned in a specific orientation.

At the bottom of the cored interval, an erosive surface marks the change to silt- and mudstone facies. **Facies F7** (Fig. 5.5J) is a siltstone with pervasive bioturbation index (BI *sensu* Taylor & Goldring (1993)) of 4. Root traces, leaf fragments, and red-coloured (siderite) clasts with diameters of 5 – 40 mm can be observed in this facies. **Facies F8** is represented by a mudstone layer at the bottom of the cored interval (Fig. 5.5K). A BI of three and angular red clasts in 1 – 40 mm size characterizes this facies. **Facies F9** (Fig. 5.5L) is positioned in-between the siltstone

(F7) and the mudstone (F8). This facies is represented by a thin (40 mm) layer of coal, and it has a porous and dry characteristics.

The last facies, calcite concreted sandstone (Facies F10; Fig. 5.5M) consist of fine- to medium-grained sandstone with calcite filling of pore space. Although the concretion is secondary, it is not possible to deduce what facies the samples had before cementation. This has therefore been defined as separate facies



**Figure 5.5:** Core images of the interpreted ten facies and four sub facies. A) Structureless sand with high chlorite content, B) structureless sand with little chlorite content, C) sandstone with mud drapes, D) pebbly sandstone, E) sandstone with cm-scale red clasts, F) sandstone with cm-scale grey clasts, G) sandstone with variation in clast size, less chaotic, H) sandstone with variation in clast size, very chaotic, I) sandstone with rounded- to angular red- and grey rounded clasts varying from mm-cm, J) siltstone with red angular clasts and high grade of bioturbation, K) mudstone with red angular clast and medium grade of bioturbation, L) coal, M) calcite concretion.

### 5.2.2 Facies associations and flow conditions

Three of the sandstone facies, **Facies F1 to F3**, show structureless sandstone with mud drapes and pebbles, and is interpreted as middle- to upper point bar (Fig. 5.6). These facies are mainly constrained to the upper parts of the cored interval (1070 – 1088 m), but also as thin layers in-between other sandstone facies. The absence of large mud- and siderite clasts indicates calmer or more regular flow conditions. This interval is also pervasively cemented by chlorite, giving the deposits a green colour, indicating marine, and perhaps tidal, influence (Dowey et al., 2012).

An increase in energy conditions occurs in the middle part of the core (1088 – 1104 m, Figs. 5.2 and 5.3). The middle part displays sandstone with cm-scale red- and grey clasts (**Facies F4A and F4B**) and moderately- and poorly sorted mud-clast conglomerate (**Facies F5A and F5B**). **Facies F4A- and B** are interpreted as channel base deposits during high energy flow (Fig. 5.6; Willis, 1989). The cm-scaled clasts are sorted out from eroded material, such as channel banks hosting siderite clasts or mudstone banks (Williams, 1966). The mud-clast conglomerate (**Facies F5A and B**) is also interpreted to be channel base deposits but consist of intraformational rip-up mud clast sorted over a moderate distance (Fig. 5.6). The clasts have rounded edges but are poorly- and moderately sorted, indicating a long and steady transport (Williams, 1966; Willis, 1989). **Facies F6** (1112 – 1113 m) displays angular siderite- and rounded to sub-rounded clasts ranging from 1x3 cm and lower. It is identified as a layer of channel lag deposits which are constrained to the channel base (Fig. 5.6; Collinson, 2019).

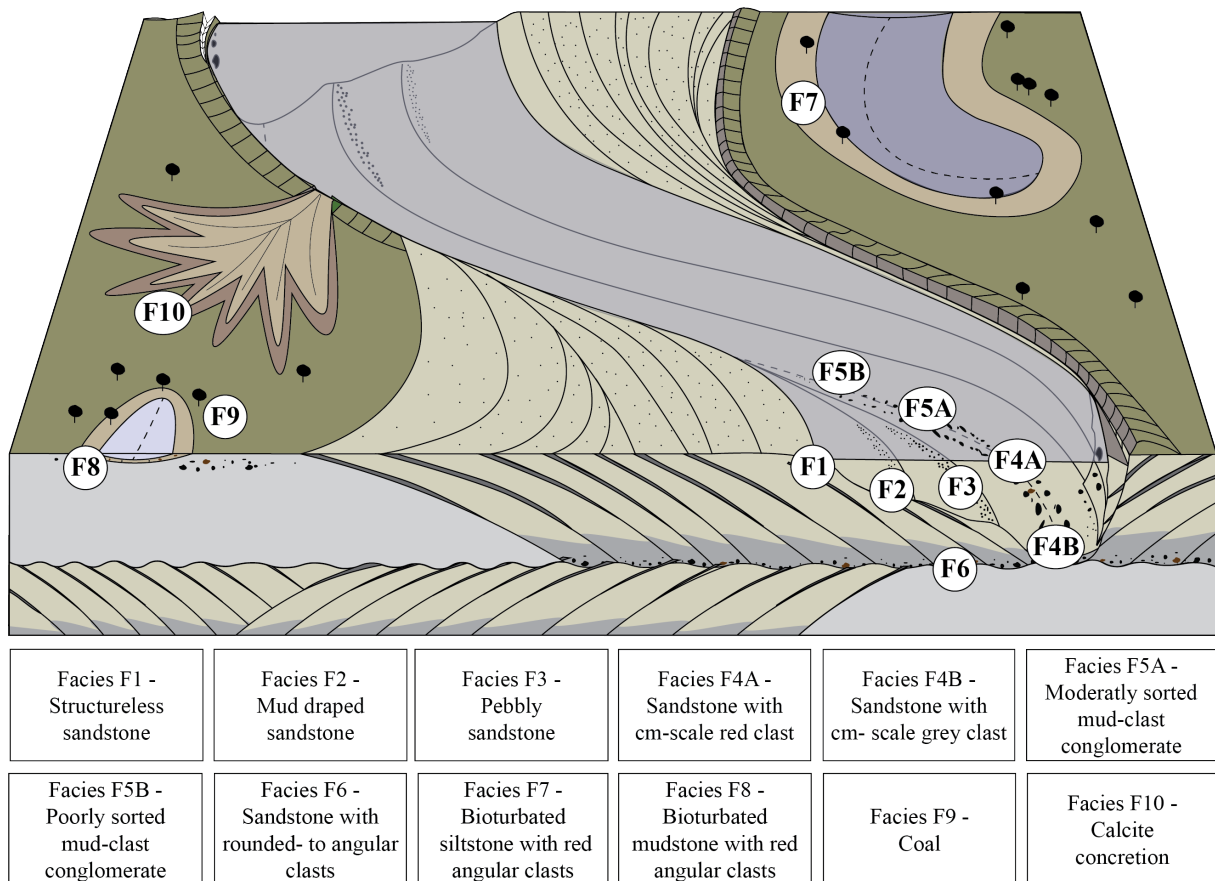
Below the sandstone facies, an erosive surface (Fig. 5.3) marks the change from sandstone to mudstone facies. The mudstone facies (**Facies F7 – F9**; 1113 – 1118 m) are interpreted as lacustrine- and bay fill deposits (Fig. 5.6; coastal plain deposits consisting of lagoonal, lacustrine and paleosol deposits). This is because of the high organic content and bioturbation, leaf fragments and roots, and grain size of silt and mud (Fig. 5.3). The paleosol texture might overprint an earlier lacustrine signature (Ghazi and Mountney, 2009). Calcite concretions (**Facies F10**), sandstone with calcite cement is also present (1102 m and 1084.5 m). Precipitation may occur in soil environment, and sandstone is usually found as floodplain deposits in soil environment (El Khoriby, 2006). The calcite concretion is present within fluvial deposits and is therefore likely eroded and redeposited as a concretion.

The associated energy level of each facies is a factor that can affect the transport and deposition of clastic sediments and especially detrital zircon grains (Garzanti and Andò, 2019). Each of the interpreted facies are associated with different levels of energy. Increasing number of clasts and clast size reflects higher energy levels, while plain sandstone facies absent of clasts indicate



lower energy facies. Grains will be in suspension until the fluvial system no longer is strong enough to transport the grain, and eventually the grain will fall out.

In this point bar system (Fig. 5.6), the structureless-, mud draped-, and pebbly sandstone (**Facies F1 – F3**) are all interpreted to be deposits from the medium energy flow conditions in the upper point bar (Miall, 1988; Cabello et al., 2018). The three other facies, (**Facies F4 – F6**), are deposited in relatively high energy flow condition facies. These facies contain clasts which requires higher energy flow conditions to transport and deposits (Ghazi and Mountney, 2009; Miall, 1988; Labrecque et al., 2011). The mudstone facies (**Facies F7 – F9**) are deposited in low-energetic flow conditions such as flood plain and upper paleosol environment (Fig. 5.6; e.g., Ghazi and Mountney, 2009). Calcite cemented sandstone (**Facies F10**) is interpreted as concretions precipitated within fluvial sandstones by later soil processes. The original deposition was likely under medium energy conditions.



**Figure 5.6:** Conceptual facies model of interpreted facies environment. Structureless-, mud draped-, and pebbly sandstone are associated with medium energy flow conditions in upper point bar. Sandstone with cm-scale red and grey clasts, moderately- and poorly sorted-, and sandstone with rounded to- angular clasts are categorized as high energy flow conditions. Coal, bioturbated silt-, and mudstone reflect low energy environment.

### 5.3 Detrital zircon fertility variations

#### 5.3.1 Description of zircon fertility variations in initial 20 samples

The 20 samples, in vertically order from top to bottom of Guovca core represents nearly all the ten different identified facies, apart from the poorly sorted mud-clast conglomerate (**Facies F5A**), bioturbated mudstone (**Facies F8**), and coal (**Facies F9**) which was not sampled because other areas had higher prioritizing. The number of picked zircon grains per gram of sample (n/gram), when every detectable zircon grain was picked, gives a strong indication of the actual zircon fertility per sample. The sample weights are from 10 – 37 grams and contain 0 – 501 detrital zircon grains (Tab. 5.2). Thus, the zircon grain picking revealed that the number of grains per samples varies widely between different samples.

The samples have been divided into four categories according to the number of zircon grains per gram (0, < 1, 1 – 4 and > 4 grains/gram). The size of samples from drill cores are often very limited. Therefore, studies where the goal is to perform detrital zircon provenance analysis, it makes sense to sample facies with higher zircon fertility. A sample with zircon fertility of four grains per gram would give at least 140 zircon grains per 35 g sample, which is typical for a drill core samples. Studies of detrital zircon commonly suggest to date more than *c.* 117 grains (Vermeesch, 2004) to make sure the detrital zircon spectra are representative, because there is a 95 % certainty that no fraction  $\geq 0.05$  of the population is missed by analysing 117 grains. In this study, the average number of zircons for all the samples is 67.8, far from what is wanted to obtain statistical significance for zircon dating. The number of zircons per gram in facies displays values from 0 in bioturbated siltstone to 6.60 in sandstone with cm-scale grey clasts (Tab. 5.2).

Two of the collected samples, BAR-75, and BAR-88, contain no zircon. These samples are from **Facies F7** (floodplain lake) and F2 (upper point-bar), two facies with relatively low energy. Five samples (BAR-69, -70, -73, -78, and -79) were analysed from **Facies F1** (structureless sandstone). These included 8, 21, 37, 57 and 67 zircons, which provides an average value of 1.08 zircons per gram facies. From **Facies F2** (upper point-bar) four other samples (BAR-71, -80, -83, and -84) were collected. These contain 14, 5, 54, and 5 grains, and counts 0.61 zircons per gram facies (Tab. 5.3). The relatively higher energy levelled **Facies F3** (pebbly sandstone) is represented with only one sample counting 164 grains, which is 4.43 zircons per gram in facies. The increase in the number of zircons per gram facies is notable as the value is much higher than F1 and F2.

**Table 5.2:** Overview of the samples and depth, weight, facies number, number of zircons in sample and number of zircons (n) per gram sample. Samples have been coloured according to amount of zircon per gram to easily see which samples contain none (white), low (red), medium (grey) and high (green) number of grains.

| Initial samples to develop model      |           |            |        |               |        |              |
|---------------------------------------|-----------|------------|--------|---------------|--------|--------------|
| Sample name                           | Depth (m) | Weight (g) | Facies | Zircons (n)   | n/gram | Energy level |
| BAR-69                                | 1070.00   | 35         | F1     | 8             | 0.23   | Medium       |
| BAR-70                                | 1074.80   | 34         | F1     | 21            | 0.62   | Medium       |
| BAR-71                                | 1079.35   | 35         | F2     | 14            | 0.4    | Medium       |
| BAR-72                                | 1080.10   | 32         | F4B    | 501           | 15.66  | High         |
| BAR-73                                | 1084.80   | 36         | F1     | 37            | 1.03   | Medium       |
| BAR-74                                | 1088.45   | 35         | F5B    | 11            | 0.31   | High         |
| BAR-75                                | 1088.70   | 35         | F2     | 0             | n/a    | Medium       |
| BAR-76                                | 1089.75   | 33         | F5B    | 58            | 1.76   | High         |
| BAR-77                                | 1093.85   | 35         | F5B    | 61            | 1.74   | High         |
| BAR-78                                | 1093.92   | 36         | F1     | 57            | 1.58   | Medium       |
| BAR-79                                | 1099.75   | 35         | F1     | 67            | 1.91   | Medium       |
| BAR-80                                | 1100.77   | 34         | F2     | 5             | 0.14   | Medium       |
| BAR-81                                | 1101.92   | 37         | F10    | 13            | 0.35   | Medium       |
| BAR-82                                | 1106.40   | 37         | F3     | 164           | 4.43   | Medium       |
| BAR-83                                | 1108.55   | 36         | F2     | 54            | 1.5    | Medium       |
| BAR-84                                | 1111.30   | 35         | F2     | 5             | 0.14   | Medium       |
| BAR-85                                | 1112.25   | 35         | F6     | 40            | 1.14   | High         |
| BAR-86                                | 1112.65   | 35         | F6     | 145           | 4.14   | High         |
| BAR-87                                | 1112.93   | 35         | F6     | 88            | 2.51   | High         |
| BAR-88                                | 1116.85   | 35         | F7     | 0             | n/a    | Low          |
| Additional samples to test hypothesis |           |            |        |               |        |              |
| BAR-89                                | 1080.10   | 17         | F4B    | 110 (sand)    | 6.47   | High         |
| BAR-90                                | 1080.10   | 35         | F4B    | 7 (mud clast) | 0.2    | High         |
| BAR-91                                | 1080.10   | 13         | F4B    | 22 (sand)     | 1.69   | High         |
| BAR-92                                | 1101.30   | 32         | F2     | 49 (drape)    | 1.53   | Medium       |
| BAR-93                                | 1103.20   | 10         | F4A    | 0 (clast)     | 0      | High         |
| BAR-94                                | 1103.20   | 12         | F4A    | 42 (sand)     | 3.5    | High         |
| BAR-95                                | 1103.20   | 15         | F4A    | 3 (siderite)  | 0.2    | High         |

The highest number of zircons were picked in **Facies F4B** (sandstone with cm-scale grey clasts). A total of 501 of grains were picked from a single sample (BAR-72), resulting in a fertility value of 6.60 zircon per gram. The zircon grains from this sample alone makes up 37 % of the total number of zircon grains from the first a river system. The sample host one clast ranging wider than the core width and was one of three samples that was resampled during the second visit at NPD. **Facies F4B** is also associated with relatively high energy levels as the large clast requires high energy to be transported. Three samples (BAR-74, -76, and -77) were collected from **Facies F5B** (poorly sorted mud-clast conglomerate), containing 11, 58, 61 zircons, respectively. F5B is associated with relatively high energy level compared to the others and has a fertility value of 1.26 zircons per gram in facies. **Facies F6** (sandstone with rounded

to- angular clasts) is interpreted as channel lag deposits, one of the highest relative energy levels. The three samples (BAR-85, -86 and -87) contains 40, 145 and 88 grains, which gives 2.6 grain per gram in facies. **Facies F7** (bioturbated siltstone with red angular clasts) does not include any zircons and is associated with a relatively low-energetic environment. **Facies F8** (bioturbated mudstone with red angular clasts) and **F9** (coal) were not sampled because mudstone and coal are not associated with detrital zircon grains. **Facies 10** (calcite concretion) included 13 grains, which is relatively low. Calcite precipitation is associated with floodplain soil, a relatively calm depositional area, with occasional increase in energy during flooding (El Khoriby, 2006).

**Table 5.3:** The average number of grains per gram in facies. Note that **Facies F3, F4A, F5B** and **F6** are the ones with the highest number per sample. F1, F2, F7 and F10 are the ones with lowest average grains per sample.

| Facies nr. | Facies  | Zircons per gram in facies |
|------------|---|----------------------------|
| F1         | Structureless sandstone                       | 1.08                       |
| F2         | Mud-draped sandstone                          | 0.61                       |
| F3         | Pebbly sandstone                              | 4.43                       |
| F4         | F4A Sandstone with cm-red clasts              | 1.22                       |
|            | F4B Sandstone with cm-grey clasts             | 6.60                       |
| F5         | F5A Moderately sorted mud-clast conglomerate  | n/a                        |
|            | F5B Poorly sorted mud-clast conglomerate      | 1.26                       |
| F6         | Sandstone with rounded to- angular clasts     | 2.60                       |
| F7         | Bioturbated siltstone with red angular clasts | n/a                        |
| n/a        | Bioturbated mudstone with red angular clasts  | n/a                        |
| F9         | Coal  | n/a                        |
| F10        | Calcite concretion                            | 0.35                       |

Briefly summarized, three samples pass the suggested statistical minimal value of 117 grains (BAR-72, -82, and -86), these have a more than four zircons per gram. Eight samples have 1 – 4 zircons per gram sample (BAR-73, -76, -77, -78, -79, -83, -85 and -87), seven samples (BAR-69, -70, -71, -74, -80, -81, -84) have less than one zircon per sample, and two samples (BAR-75 and -88) does not include any zircons. On average, the four facies with the lowest fertility are F7 (bioturbated siltstone with red angular clasts) with 0 grains, F10 (calcite concretion) with 13, F2 (mud-draped sandstone) with 16 and F1 (structureless sandstone) with 38. The four samples with highest fertility are F5B (poorly sorted mud-clast conglomerate) with 42 grains on average, F6 (sandstone with rounded to- angular clasts) with 91 grains, F3 (pebbly sandstone) with 164, and F4B (sandstone with cm-scale grey clasts) which has 501 grains. The samples show large variations in fertility within the facies, but the average value of zircons per

gram of sample material in the facies gives a strong indication on the fertility variations between the facies.

### 5.3.2 Hypothesis for controls on detrital zircon fertility

Based on the inter-sample variability described in Section 5.3.1, the following hypothesis has been devised: the highest zircon fertilities are recorded in facies associated with high energy levels. The detrital zircons are found within the sand, and not the mud- or siderite clasts. Low zircon fertilities are observed in mud-draped sandstone. This hypothesis is based on the presence of zircon grains in previous samples.



**Figure 5.7:** The three parts of the core where the seven samples were collected, first part contain a clast positioned with sand above and under, second part contained mud-draped sandstone, and last part contain siderite clast, mud clast and sand.

Seven additional samples (Tab. 5.2) were collected during a second visit at the Norwegian Petroleum Directorate with the goal to test a hypothetical model above. The sandstone and mud- and siderite clasts were separated and sampled individually to source the detrital zircon grains. BAR-89, -90, and -91 were collected from the same area as BAR-72 (**Facie F4B**; 1080.1 m), the most fertile sample, to verify if and how many zircon grains that were sourced from clasts or sand. One sample, BAR-92 (1101.3 m), were collected to verify low fertility in mud-draped sandstone, and three samples (BAR-93, -94, and -95) were collected at 1103.2 m to verify the fertility of mud clast, sand, and siderite clasts. Confirmation of the grains and quantification of fertility was conducted using scanning electron microscope (SEM).

BAR-89 (**Facies F4B**; upper sandstone, Fig. 5.7) displayed high zircon fertility of 6.47 grains per gram and BAR-90 (mud clast) displayed low fertility of 0.2 grains per gram, confirming the hypothesis that facies with cm scale clasts contain high number of grains, and that the detrital zircons are found from the surrounding sand matrix. An unexpected low fertility of 1.69 was displayed in BAR-91 (**Facies F4B**; lower sandstone, Fig. 5.7), high fertility was expected as the sample is such short distance to BAR-89.

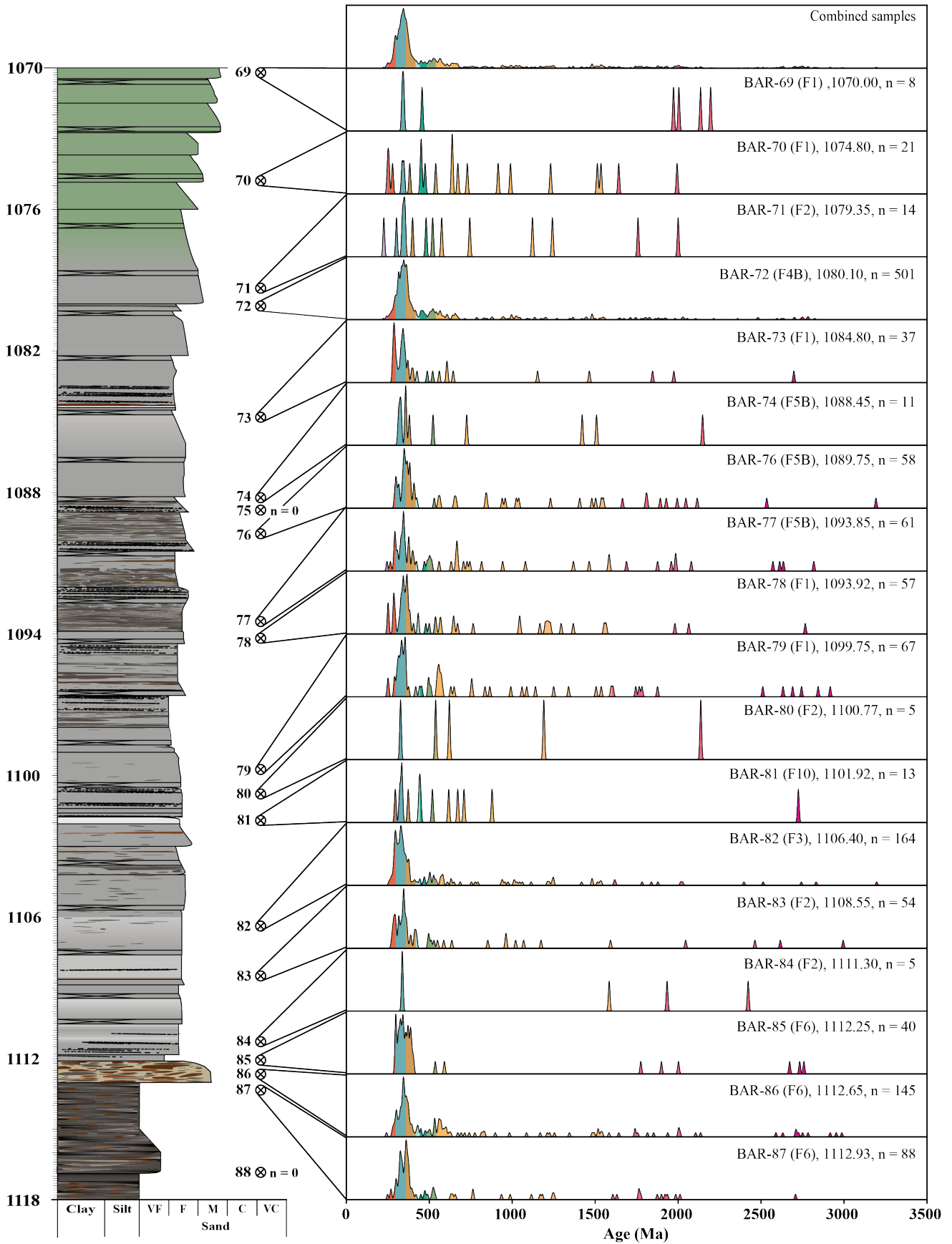
BAR-92 (**Facies F2**; mud-draped sandstone) displayed a high number of zircon grains per gram (1.53 grain per gram), but the large sample size gives it a moderate zircon per gram value. A low number was expected for this facies sample, such as most of the previous samples, but a moderate value was obtained.

BAR-93 (**Facies F4A**; mud clast, Fig. 5.7) did not included any zircons, whereas to siderite clast (BAR-95), included only three zircon grains. The sandstone matrix around BAR-93 and -95 contained 42 zircons in 12 grams, leaving a value of 3.5 grains per gram which is in the upper levels. This gave supporting evidence to the hypothesis above.

## 5.4 Zircon geochronology

### 5.4.1 Detrital zircon age distributions

From the LA-ICP-MS geochronology, 1417 zircons from eighteen samples were analysed. Using the given boundaries for concordance ( $\geq 90\%$ ), 1349 (95 %) of the grains were included. Individually the samples differ from each other in number of detrital grains, two samples did not include any zircons, 15 samples have up to 99 zircon grains, and three samples have over 100 zircon grains. It is clear that fertility is variable, and according to Vermeesch (2004), only three of these samples would be approved for zircon age distribution. To investigate whether there is evidence of sorting effects or changing detrital zircon age signals within the studied deposit, and to investigate the influence of sample size on detrital zircon age spectra, only the spectra with more than thirty grains will be mentioned in the following section. The 12 detrital zircon age spectra with more than 30 concordant grains all display a distinct blue Carboniferous age peak (blue in Fig. 5.8). The sample with the most grains (501 grains; BAR-72) displays a very similar detrital zircon age spectre as the combined spectre. It represents 35 % of the grains from all the eighteen samples, clearly indicating that the high number of grains yields a representative kernel density plot of zircon ages.



**Figure 5.8:** Sedimentary log of well 7131/4-1 and the picked samples to the right of the log. Kernel density plots of the detrital zircon age spectras from the cored samples to the right. Combined zircon age spectras at the top, and individual spectras under. Note the BAR-72 sample with 501 grains and BAR-84 with only five grains. All samples also have a Carboniferous (blue) peak, which is typical for eastern sourced sediments. Sample positions are not perfectly positioned, see Figs. 5.2 and 5.3 for accurate positions.

Carboniferous zircons dominate samples BAR-72 (36 % of the grains), with the highest peak located in the early Carboniferous. Additionally, a Permian peak (8 % of the grains) increasing towards Carboniferous, and a Devonian (19 % of the grains) peak decreasing from the Carboniferous shaped like a normal distribution with the early Carboniferous as middle value. There are also smaller, almost not visible peaks between Silurian – Mesoproterozoic, and some single grains with ages from Triassic to Archean.

BAR-73 differs slightly from BAR-72, as more of the grains are Permian in age (22 % of the grains). The rest of the spectra, even with only 37 grains, displays strong similarities to both BAR-72 and the combined sample. The Carboniferous peak is quite narrow for BAR-73 (35 % of the grains), which is also the case for BAR-76 (58 grains), -77 (61 grains) and -78 (57 grains) (28 – 30 % of the grains), but it differs in the way that the Permian peak is higher than the Carboniferous. BAR-76, -77, -78 and -79 all have some similar trends, a jagged normal distributed spectra with a tail of individual grains from Silurian and further to the Archean. BAR-76 consists of 58 grains and has two grains with Permian age, while the three others have a couple more with an additional small Triassic peak. Moreover, BAR-79, with 67 grains has a wider Carboniferous peak (36 % of the grains).

BAR-82, the sample with the second most detrital zircon grains (164 grains), displays a spectre with somewhat similar pattern as BAR-72, and the combined sample. It differs a bit with a narrow early Permian peak (14 % of the grains), and a wide Carboniferous peak (37 % of the grains). The ages are the unevenly distributed but has the same tail as the combined sample.

The Carboniferous peak (37 % of the grains) at BAR-83 (54 grains) is similarly narrow as BAR-73, -76 and -77, and it also has a tail of individual grains reaching much older ages. The spectre of BAR-85 (40 grains) differs strongly from the other spectra, the Carboniferous (47 % of the grains) and Silurian (29 % of the grains) peak is very high and wide, the Permian age is very narrow, and almost no grains peak in the tail. Only eight grains in the tail means that the rest of the 32 grains have a Permian to Silurian age. BAR-86 consists of 145 grains and has a similar detrital age distribution as BAR-72 and -82: a normally distributed curve with a top at Carboniferous (28 % of the grains) but with a narrower Carboniferous interval. It also has a peak at the early Neoproterozoic period and some small peaks consisting of one, two or three grains in the Mesoproterozoic to Archean. BAR-87 consists of 88 grains and has very similar looking spectre as the ones with more than 117 grains, the normally distributed peak at mid Carboniferous (35 % of the grains) is present in this case. The tail is much like the other tails, a few grains with ages ranging to Archean, it also has one grains with a Triassic age.



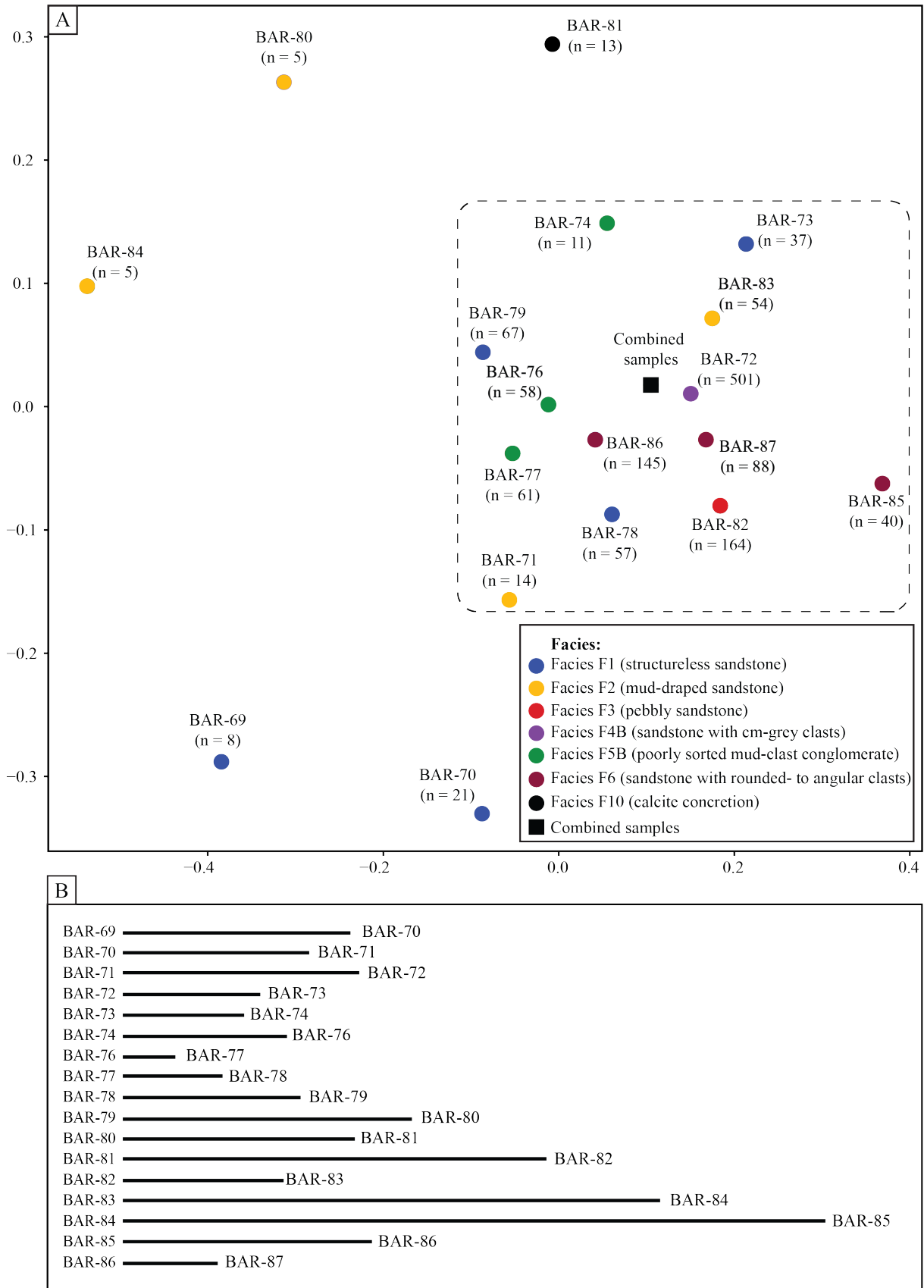
Generally, the combined spectra display few Triassic grains, a normal distribution from Permian to Ordovician with distinct peaks in early Carboniferous. There is also a wide group of grains with ages from Ordovician to *c.* 700 Ma, and a long tail that displays modest amounts of grains with ages ranging from 700 – 3000 Ma. The distinct peak around Carboniferous is commonly interpreted to be associated with the Uralian fold and thrust belt, the plateau from Ordovician to *c.* 700 Ma is associated with the Timanide orogen, and the long tail to be associated to a large catchment area with small-scale magmatic rocks from almost all time periods (c.f. Gilmullina et al., 2021).

#### 5.4.2 Multidimensional scaling

To investigate for similarities between the detrital zircon spectra, a statistical tool called multidimensional scaling has been applied (MDS). An MDS plot is a two-dimensional scatter plot that utilizes the *D* value from Kolmogorov-Smirnov (K-S) test to visualize samples with high similarity close together and dissimilar samples further away (Vermeesch, 2013; Spencer and Kirkland, 2016). All eighteen samples are shown in the MDS-plot (Fig. 5.9A), and in the combined by facies MDS-plot (Fig. 5.10), even the samples with less than 30 grains. They are included to display the grade of dissimilarity that is formed due to the low number of grains.

The combined spectra and the eighteen zircon age spectra display a cluster around the combined age spectre (dotted square, Fig. 5.9), and a few outliers (BAR-69, -70, -80, 81-, and -84) outside the square. Few grains are common for all the outliers and two samples with low number of grains (BAR-71, *n* = 14 and BAR-74, *n* = 11) cluster even with a low number of grains. The samples with highest similarity to the combined spectra are BAR-72, -76, -83, -86, and -87. The number of grains in these samples vary between 54 and 501 and the take from this is that samples with quite low fertility can show similar age spectre to high fertile samples.

Structureless sandstone, (**Facies F1**, blue markers) and mud-draped sandstone (**Facies F2**, yellow markers) provides the most dissimilar detrital zircon age spectra within the facies. The pebbly sandstone (**Facies F3**, red marker) is the second most fertile sample (*n* = 164). It shows strong similarities to the other samples with high zircon fertility (BAR-72 and -86). In the drill core, BAR-72 is very far from the three surrounding samples, but the spectre is very similar. Sandstone with cm-scale grey clasts (**Facies F4B**, purple marker), the most fertile samples is surrounded by BAR-83, -86, and -87. The poorly sorted mud-clast conglomerate (**Facies F5B**, green markers) all plot very close to each other and the combined samples in the main cluster.

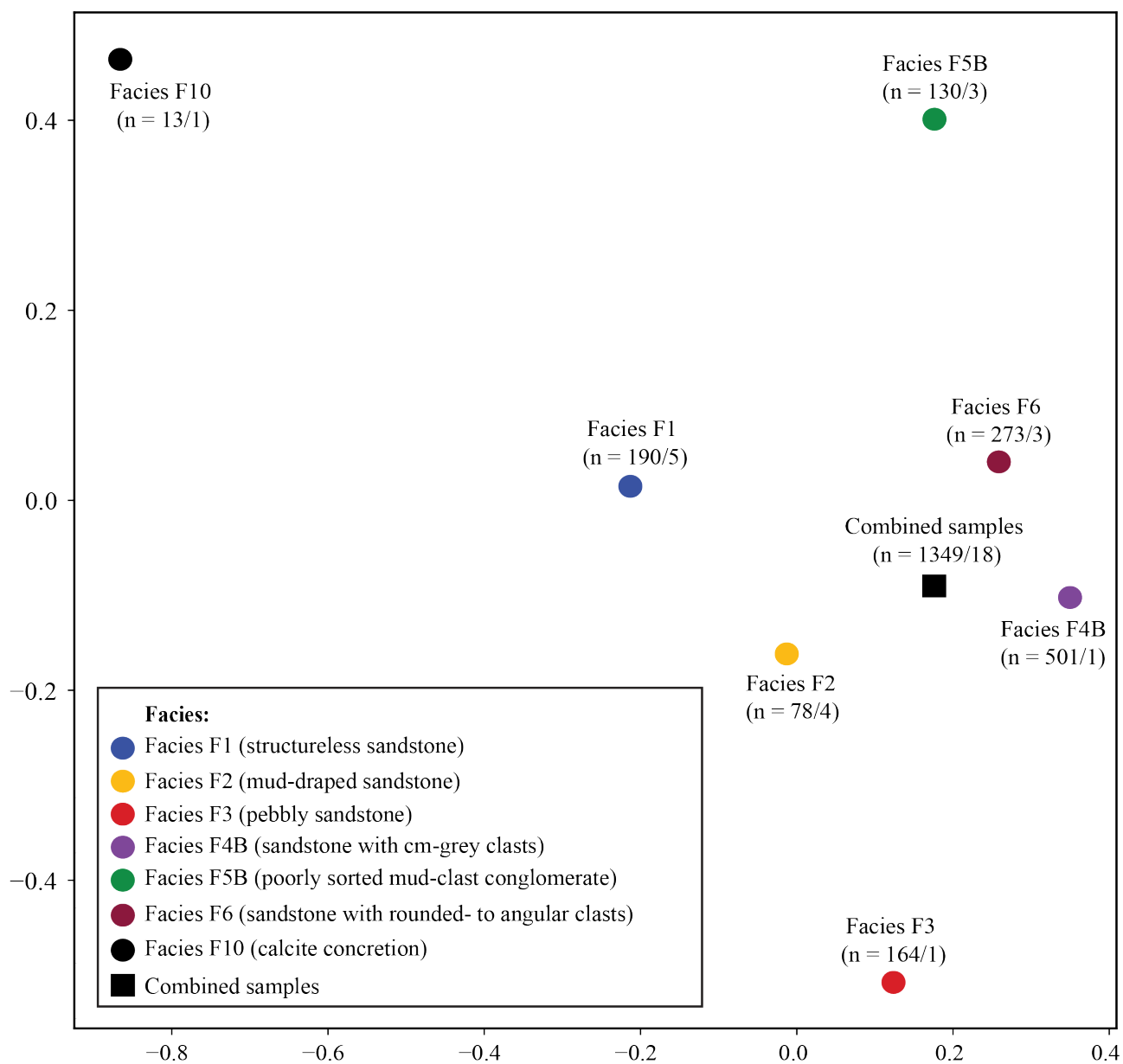


**Figure 5.9:** A) Multidimensional scaling of the 18 detrital zircon age spectra that were produced from the LA-ICP-MS analysis. The plot displays the similarity of the zircon age spectra, where the spectra with most similarity cluster around each other. A group of 13 samples cluster around the combined sample while five samples are displayed as outliers. B) The relative distance between the spectra indicates the relative dissimilarity between the samples. Note the low grade of dissimilarity at the upper part of the plot and both similar and dissimilar spectrums at the bottom half of the core.

The spectras of the sandstone with rounded to- angular clasts (**Facies F6**, dark red markers) show moderate distances to each other and the main cluster. Samples in Facies F6 are very close in core depth meaning that major change in spectra is not expected, this is also the case for the poorly sorted mud-clast conglomerate, since they are closely positioned in the core. The calcite cemented sandstone (**Facies F10**), is far from the main cluster, indicating a dissimilar spectre.

The second plot (Fig. 5.9B) displays dissimilarities between the spectra as lines: short lines indicate similar spectra, whereas long lines represent dissimilar spectra. It is worth mentioning that the BAR-samples are vertically in order downward in the cored interval. This makes it interesting to look at the similarity vertically through the interval. The distance of the lines in the upper core is medium to low, the distances have a decreasing trend until BAR-76 which has the most similar spectre as BAR-77 accompanied by BAR-78 which also has one of the shortest lines. Further towards BAR-82 and BAR-85 the spectra have an increase in dissimilarity with BAR-84 to BAR-85 with the highest dissimilarity. From this spectre the distance decreases until BAR-86 and BAR-87 which also has one of the shortest distances, indicating a very similar spectre as the above. Overall, the plot displays an increase in spectre similarity to BAR-77, from here the spectra similarity decreases to BAR-85 before the similarity decreases again at BAR-87.

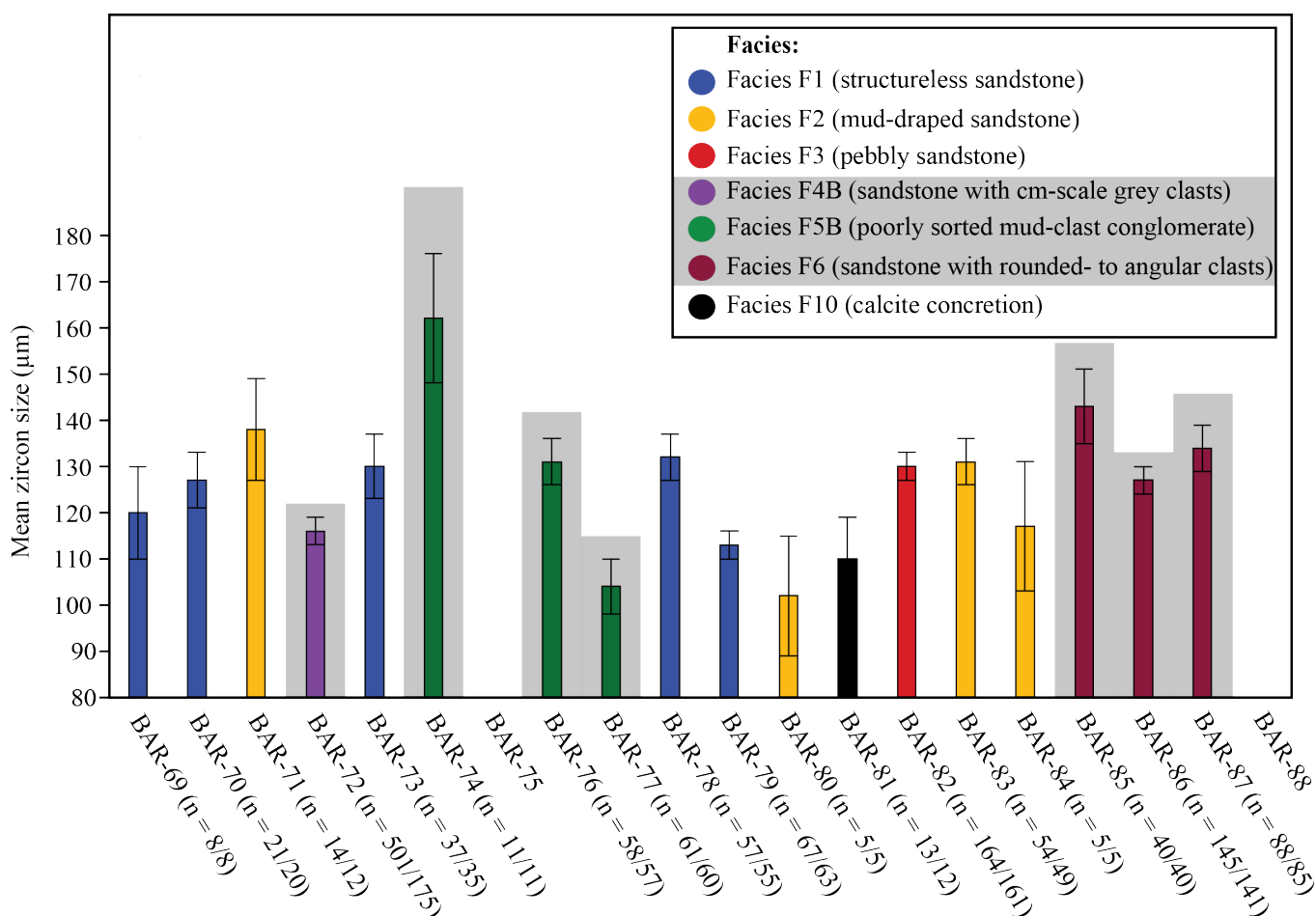
The detrital zircon analyses can also be plotted in an MDS plot according to their facies (Fig. 5.10). The combined spectra of mud-draped sandstone (**Facies F2**), sandstone with cm-scale clasts (**Facies F4B**), and sandstone with rounded to- angular clasts (**Facies F6**), seem to be clustering around the combined sample. The three facies have a large variation in number of grains, but still display very similar zircon age spectra. In total, they make up of 63 % of the collected grains. The combined spectra of **Facies F2**, which only represent 6 % of the grains in total, show a spectre with high similarity to the other two spectra which represents 37 % and 20 % of the total collected grains. The spectra of **Facies F1**, structureless sandstone, is also quite close to the main cluster. **Facies F1** and **F2** display age spectra from samples collected all over the cored interval and have large variations in number of grains in sample. **Facies F3**, pebbly sandstone, is only represented with one sample, and thus, the spectra display the same degree of similarity to the main cluster as in Fig. 5.9A. **Facies F5B**, poorly sorted mud-clast conglomerate, is represented with three samples and show moderate similarity as well. The last facies, calcite concretion (**Facies F10**), is clearly the sample with lowest similarity and the lowest number of grains.



**Figure 5.10:** Multidimensional scaling the zircon age spectra combined as facies. Facies **F1**, **F2**, **F4B**, and **F6** display the highest similarity and cluster around the combined sample. Facies **F3**, **F5B**, and **F10** show spectra with lower similarity than the four that cluster around the combined sample. Parentheses show number of grains/number of samples.

### 5.5 Zircon size

Zircon grains in all samples have been measured in Fiji (v. 4), except for BAR-74, where only a selected area was measured due to the high number of grains. Quantitative measurements of the longest axis of zircon grains show large variations in size within each sample (Tab. 5.4; Fig. 5.11), but small variations in mean zircon size. The smallest value of mean long-axis is observed in BAR-80 (**Facies F2**;  $102 \pm 13 \mu\text{m}$ ) and is interpreted as medium energy flow conditions. The largest mean value is observed in BAR-74 (**Facies F5B**;  $162 \pm 14 \mu\text{m}$ ; Fig. 5.12), which is interpreted as high energy flow conditions. BAR-85 (**Facies F6**; Figs. 5.11 and 5.12) displays the second highest mean values and is also interpreted as high energy facies. BAR-77 (**Facies F5B**; Fig. 5.12) is interpreted as high energy facies but displays the second lowest mean value ( $104 \pm 6 \mu\text{m}$ ). This is also the case for BAR-72, which has the fifth lowest value while being a high energy facies (Fig. 5.11).



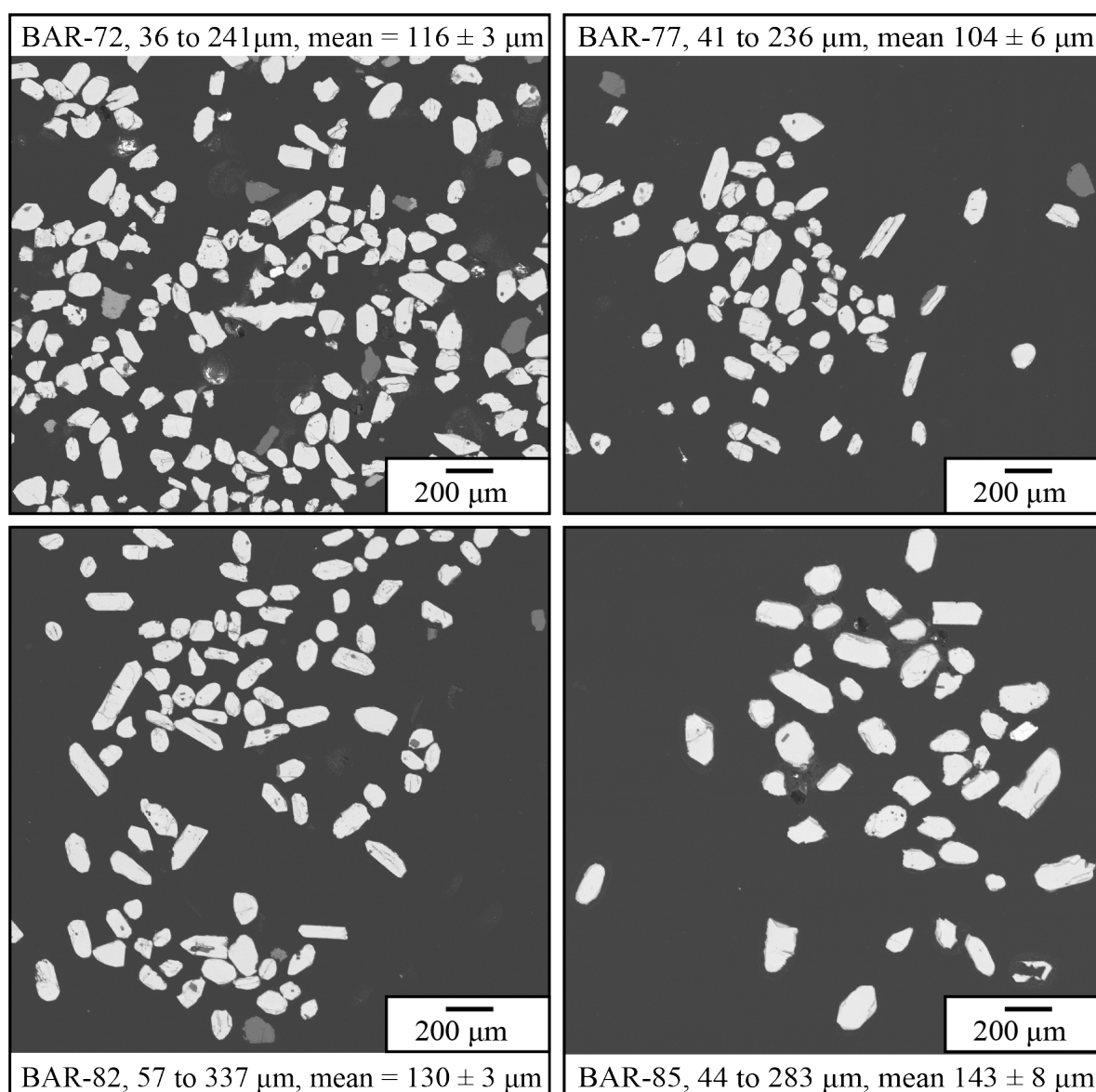
**Figure 5.11:** Mean zircon size distribution for all samples from top to bottom of the cored interval. Samples highlighted in grey are interpreted as high-energy facies and the other have medium energy. Note that BAR-74 and BAR-76 display large differences while been interpreted as the same facies. Large uncertainties are present in low fertility samples, while high fertility samples show low uncertainty.

The largest difference in zircon size is observed in BAR-78 (**Facies F1**; 280  $\mu\text{m}$ ) and the smallest in BAR-80 (74  $\mu\text{m}$ ; Fig. 5.11). The difference between the lowest and highest sample mean is *c.* 60  $\mu\text{m}$ , this is lower than the smallest grain difference in a sample (BAR-80; 74  $\mu\text{m}$ ). The largest zircon grain is visible in BAR-82 (**Facies F3**), with the zircon size of 337  $\mu\text{m}$  (Fig. 5.12), and the smallest grain is measured in BAR-86 (**Facies F6**), with the size of 28  $\mu\text{m}$ . This shows that there are large variations within the samples than there is between the samples. Some of the grains have a significantly low number of measurements because of the low fertility. BAR-74 has the highest mean, but only 11 grains, so the aspect of representativity is highly discussable for the samples with low number of grains. The mean grain size varies between  $102 \pm 13$  and  $162 \pm 14$   $\mu\text{m}$ , which is significantly lower than the Fritsch Pulverisette discmill where all samples are crushed to fractions  $< 315$   $\mu\text{m}$ . From the SEM-images of zircon mounts, there is no sign of zircon grains which have been larger than this.

**Table 5.4:** Mean value of the longest axis on the zircon grains from all samples. There are not any large variations of mean zircon size or between the smallest and largest axis of the zircon grains.

| Sample name   | n   | n/gram | Measurements | Mean ( $\mu\text{m}$ ) | Variation ( $\mu\text{m}$ ) | Energy level |
|---------------|-----|--------|--------------|------------------------|-----------------------------|--------------|
| <b>BAR-69</b> | 8   | 0.23   | 8            | $120 \pm 10$           | 84 – 162                    | Medium       |
| <b>BAR-70</b> | 21  | 0.62   | 20           | $127 \pm 6$            | 74 – 190                    | Medium       |
| <b>BAR-71</b> | 14  | 0.4    | 12           | $138 \pm 11$           | 79 – 213                    | Medium       |
| <b>BAR-72</b> | 501 | 15.66  | 175          | $116 \pm 3$            | 36 – 241                    | High         |
| <b>BAR-73</b> | 37  | 1.03   | 35           | $130 \pm 7$            | 74 – 248                    | Medium       |
| <b>BAR-74</b> | 11  | 0,31   | 11           | $162 \pm 14$           | 111 – 249                   | High         |
| <b>BAR-75</b> | n/a | n/a    | n/a          | n/a                    | n/a                         | Medium       |
| <b>BAR-76</b> | 58  | 1.76   | 57           | $131 \pm 5$            | 65 – 264                    | High         |
| <b>BAR-77</b> | 61  | 1.74   | 60           | $104 \pm 6$            | 41 – 236                    | High         |
| <b>BAR-78</b> | 57  | 1.58   | 55           | $132 \pm 5$            | 60 – 302                    | Medium       |
| <b>BAR-79</b> | 67  | 1.91   | 63           | $113 \pm 3$            | 62 – 194                    | Medium       |
| <b>BAR-80</b> | 5   | 0.14   | 5            | $102 \pm 13$           | 72 – 146                    | Medium       |
| <b>BAR-81</b> | 13  | 0.35   | 12           | $110 \pm 9$            | 74 – 174                    | Medium       |
| <b>BAR-82</b> | 164 | 4.43   | 161          | $130 \pm 3$            | 57 – 337                    | Medium       |
| <b>BAR-83</b> | 54  | 1.5    | 49           | $131 \pm 5$            | 74 – 242                    | Medium       |
| <b>BAR-84</b> | 5   | 0.14   | 5            | $117 \pm 14$           | 90 – 164                    | Medium       |
| <b>BAR-85</b> | 40  | 1.14   | 40           | $143 \pm 8$            | 44 – 283                    | High         |
| <b>BAR-86</b> | 145 | 4.14   | 141          | $127 \pm 3$            | 28 – 271                    | High         |
| <b>BAR-87</b> | 88  | 2.51   | 85           | $134 \pm 5$            | 63 – 286                    | High         |
| <b>BAR-88</b> | n/a | n/a    | n/a          | n/a                    | n/a                         | Low          |

From SEM-images of sample thin sections, the fertility in thin section does not clearly reflect the observed fertility of the samples from mineral separation. BAR-72, -74, and -82 was investigated as they are categorized with high, low, and medium fertility. The fertility variations were not observed and the reason for this is uncertain. Thin sections only display a small part of the sample, so maybe it is not representative enough for the rest of the sample. Small zircon grains with size between 2.71 – 5.64  $\mu\text{m}$  is observed within quartz grains, but these are too small to be point shot with laser. These small grains within quartz are removed when quartz is removed in the mineral separation.



**Figure 5.12:** SEM-images of zircon size in four samples display large variations in zircon size within each sample. The large variations are observed in all samples. The validity for some of the measurements is quite low as the samples have low fertility.

## 5.6 Petrological data

A total of 20 thin sections were optically analysed for mineralogical distribution, grain size and porosity. Some of the thin sections display parts of the samples where sandstone is present with structures, clasts, or secondary processes. This makes the change between mineralogy and additions characteristics comparable. A selection of thin sections representing the differences within the core will be presented down under with a description.

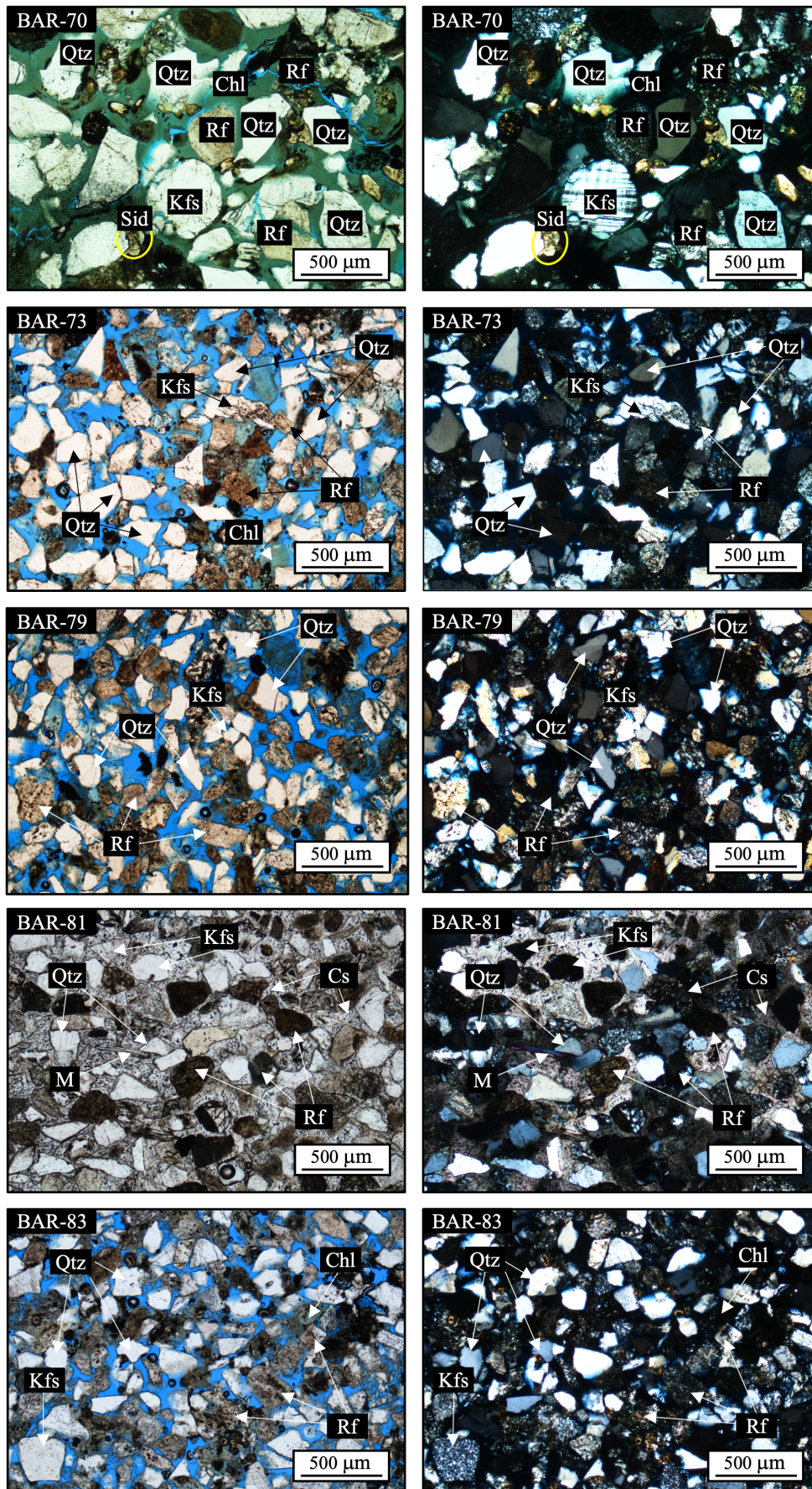
### 5.6.1 Mineralogical description

The thin sections were petrographically investigated under an optical microscope connected to a computer. The results are presented in Tab. 5.5. Small variations were encountered vertically, in which changes in grain-size and secondary processes are the most abundant changes. The sampled interval from 1070 m to 1118 m contains very fine- to medium-grained sandstone supporting mud drapes and clasts varying in size, shape, colour, and orientation. The medium-grained sandstone is constrained to the upper and lower part of the core and shows minimal variations in mineralogy. The mineralogical distribution consists mainly of large proportions of quartz (~37 %) and rock fragments (~20 %), and lower proportions of plagioclase (~10 %), and mica minerals. Grain shape is mainly angular to subangular. Secondary minerals, such as chlorite, siderite and calcite are observed in all the medium-grained samples as pore-filling cements. The secondary minerals are visible alone or together like in BAR-70, where chlorite coating is highly present together with siderite (Fig. 5.13).

In the middle part of the cored interval, the mineralogical composition and proportions are the same as for the upper- and lower medium-grained sandstone. Large proportions of quartz, rock fragments and low proportions of plagioclase. The fine- and very-fine grained sandstone also displays chlorite, siderite, and calcite. There are large differences in porosity within the samples, some display no- to very low porosity, e.g., BAR-73 and BAR-83, while some display much higher, e.g., BAR-70 and BAR-81 which is fully calcite cemented (Fig. 5.13).

The petrological signature is consistent with the observations from Mørk (1999) and Fleming et al. (2016), which also show immature sandstone samples with high proportions of quartz and rock fragments. The petrological signature can be interpreted as arkose litharenite, an immature sandstone, with high proportions of rock fragments and low proportions of quartz and feldspar. The medium- to fine grained sandstone with immature composition is a cause of long transport distances and young volcanic sources winnowing out coarse material (Omme, 2009; Bue and Andresen, 2014; Eide et al., 2018).





**Figure 5.13:** Microphotograph of a selection of thin sections with very fine- to medium grained sandstone. Chlorite coating is highly present in the medium grained BAR-70. BAR-70, -79 and -83 show fine- and very-fine grained sandstone. Calcite cementation is present as pore filling in BAR-81. Abbreviations: Qtz–quartz, Rf–rock fragments, Chl–chlorite, Kfs–potassium feldspar, Sid–siderite, M–mica, Cs–calcite.

**Table 5.5:** Overview of the petrological results. Vertical variations in grain size, level of pore filling, porosity and minerals interpreted from microscopic analysis are visible. Note that some of the samples contain both matrix and mud- or silt clasts that also has been mineralogical analysed. Parts of BAR-82 and BAR-88 are not interpreted as they show no grains.

| Sample name | n/gram | Depth (m) | Grainsize | Pore filling | Porosity | Framework minerals  |
|-------------|--------|-----------|-----------|--------------|----------|---|
| BAR-69      | 0.23   | 1070.00   | Medium    | Very much    | Low      | Quartz, rock fragments, chlorite, siderite                |
| BAR-70      | 0.62   | 1074.80   | Medium    | Very much    | Low      | Quartz, rock fragments, plagioclase, chlorite, siderite   |
| BAR-71      | 0.4    | 1079.35   | Medium    | Medium       | Low      | Quartz, rock fragments, chlorite, siderite                |
| BAR-72      | 15.65  | 1080.10   | Silt      | None         | None     | Mud clast (no grains are visible)                         |
|             |        |           | Fine      | Very little  | Moderate | Quartz, rock fragments, plagioclase, muscovite, chlorite, |
| BAR-73      | 1.03   | 1084.80   | Fine      | Very little  | Good     | Quartz, rock fragments, chlorite                          |
| BAR-74      | 0.31   | 1088.45   | Fine      | None         | None     | Calcite and quartz  |
| BAR-75      | 0      | 1088.70   | Fine      | None         | Good     | Quartz, rock fragments, chlorite                          |
| BAR-76      | 1.75   | 1089.75   | Silt      | None         | Low      | Calcite, quartz, tiny fragments                           |
|             |        |           | Fine      | Very little  | Medium   | Quartz, rock fragments, chlorite                          |
| BAR-77      | 1.74   | 1093.85   | Very fine | Very little  | Low      | Calcite   |
| BAR-78      | 1.58   | 1093.92   | Fine      | Very little  | Moderate | Quartz, rock fragments, chlorite                          |
| BAR-79      | 1.91   | 1099.75   | Very fine | Very little  | Good     | Quartz, rock fragments, chlorite                          |
| BAR-80      | 0.14   | 1100.77   | Very fine | None         | Good     | Quartz, rock fragments, chlorite                          |
| BAR-81      | 0.35   | 1101.92   | Fine      | None         | Low      | Calcite, quartz, rock fragments, muscovite                |
| BAR-82      | 4.43   | 1106.40   | Mud       | None         | Low      | Not visible   |
|             |        |           | Fine      | Very little  | Moderate | Quartz, rock fragments, chlorite                          |
| BAR-83      | 1.54   | 1108.55   | Very fine | Very little  | Moderate | Quartz, rock fragments, chlorite                          |
| BAR-84      | 0.14   | 1111.30   | Very fine | Medium       | Moderate | Quartz, rock fragments, chlorite                          |
| BAR-85      | 1.14   | 1112.25   | Fine      | Much         | Moderate | Quartz, rock fragments, chlorite                          |
| BAR-86      | 4.14   | 1112.65   | Medium    | Medium       | Moderate | Quartz, rock fragments, muscovite, chlorite               |
| BAR-87      | 2.5    | 1112.93   | Medium    | Very little  | Low      | Quartz, rock fragments, muscovite, chlorite, calcite      |
| BAR-88      | 0      | 1116.85   | Silt/mud  | None         | Low      | Not visible   |

## 6 DISCUSSION

---

This study provides information on detrital zircon fertility variations in sediments through an early Carnian core interval from the southwestern Barents Sea. Through detailed sedimentological, geochronological, and petrological analysis, a point bar deposit is explored with the aim to increase understanding of detrital zircon in fluvial systems by combining several disciplines and data from the study area. The following sections will critically evaluate the results from seismic point bar investigations, sedimentological facies analysis, fertility variations, and petrological data. Firstly, the learning outcome on Barents Sea provenance and geodynamics from the Guovca point bar zircon age spectrum will be evaluated. Secondly, the causes of the zircon variations will be evaluated in comparison with other literature. Thirdly, the zircon age spectra will be validated and compared to other zircon spectra from the Barents Sea Region. Lastly, some advice for further collection of zircons in low-zircon fertility sandstone will be given.

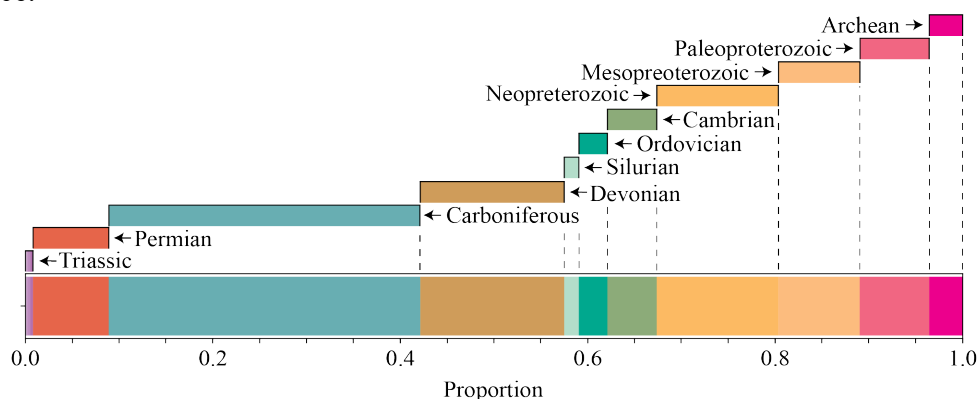
### 6.1 What can be learned about Barents Sea Provenance and geodynamics from the new Guovca point bar zircon age spectrum?

#### 6.1.1 Sediment sources in the Guovca point bar

Provenance sources in the Great Barents Sea Basin have been discussed in multiple papers over the last decades, especially for the Triassic and Jurassic units (e.g., Bergan and Knarud, 1993; Mørk, 1999; Ryseth, 2014; Klausen et al., 2015; Fleming et al., 2016; Bue and Andresen, 2014; Eide et al., 2018; Gilmullina et al., 2020), much because of the interest in hydrocarbon exploration. Provenance is important because reservoir (e.g., properties such as permeability and porosity) often are connected to distinct sand characteristics such as maturity, which may vary with the source of sediments (Haughton et al., 1991). Detrital zircon geochronology, accompanied with other disciplines can help to identify the source area for these sediments, as demonstrated in this thesis. Sediment sources tend to provide distinct zircon age spectra that reflect a pattern of peaks connected to geodynamic events in the source region. In the Barents Sea area, many papers distinguish between Uralian, Caledonian and Fennoscandian age signatures. Uralian zircon spectra tend to have a 270 – 350 Ma age signature, Caledonian age signatures are recognized by an age peak in with Paleozoic mixed with Mesoproterozoic ages, while the Fennoscandian source has Meso- and Neoproterozoic age signature from northern Finnmark and Archean to Paleoproterozoic from the Fennoscandian Shield (Klausen et al., 2017; Line et al., 2020).



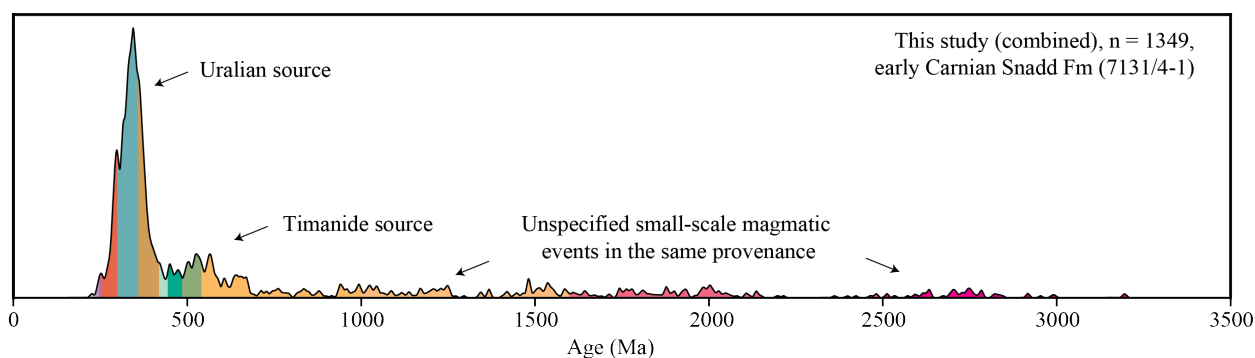
From this study, the samples contain a few Triassic zircons, and a normal distribution of Permian and Carboniferous ages (41 %; Fig.6.1), with a distinct peak being located in the Carboniferous. A wide plateau of grains with ages from Ordovician to *c.* 700 Ma, and a long tail that displays modest amounts of grains with ages ranging from 700 – 3000 Ma (Fig. 6.2). This can be interpreted as Uralian sourced, as their main age component matches with the occurrence of Uralian Orogeny (Faleide et al., 2018). The group of zircon ages from the Ordovician to *c.* 700 Ma are age associated with the Timanide Orogeny and the long tail of older grains with small-scale magmatic events from a large catchment area in the surrounding provenance.



**Figure 6.1:** Bar chart of the proportions of age populations from the combined zircon age spectra. Note the large proportions of Permian and Carboniferous ages (41 % of the grains). There is also a very large proportions of Devonian age populations (16 % of the grains), in total of 57 % of the grains are Permian to Devonian age.

The detrital zircon spectra with a high number of grains presented in this thesis do not display significant variations in source regions throughout the cored interval. This is proven with the close distance the age spectra show in the MDS plot (Fig. 5.9A), where samples from the entire interval are represented in the main cluster. Klausen et al. (2014) has stated that the Guovca meandering channel body has an interpreted thickness of *c.* 58 m. Thus, the cored interval is assumed to be sediments from the same systems. The sediments are interpreted to originate from a system that was not largely influenced by many other sources since it displays such a vertically continuous similarity of age spectra. One important argument as to why the Guovca point bar mainly was sourced by one sediment provenance area is the time it takes for a meandering turn to move. Geodynamic events, such as the Uralian orogeny lasted for a couple of hundred million years. However, by assuming a similar latera migration rate for this system as the Mississippi (*c.* 59.1 m/year; Hudson and Kesel, 2000), a 19 km wide point bar deposit must have been deposited during *c.* 300 years. This is significantly shorter than changes in sediment sources from geodynamic events can change. One can therefore not expect to observe large geodynamic changes in the zircon grains through the point bar deposit. Meandering rivers

with such dimensions are often present in the proximal area of deposition, which supports the theory that the sediments are sourced from the Uralian areas (Klausen et al., 2014). High proportions of quartz and rock fragments and low proportions of plagioclase, feldspar, and accessory minerals (chlorite, mica, and calcite) indicate immature sediment (Section 5.6.1).



**Figure 6.2:** Combined zircon age spectra from the cored interval, note the large peak at the Carboniferous which represents 36 % of the collected zircon grains. The Permian-Devonian grains are sourced from the Uralian orogeny and the Devonian to middle of Neoproterozoic is sourced from the Timanide orogeny. The tail of grains from c. 700 Ma is source to small-scale magmatic events in the same provenance.

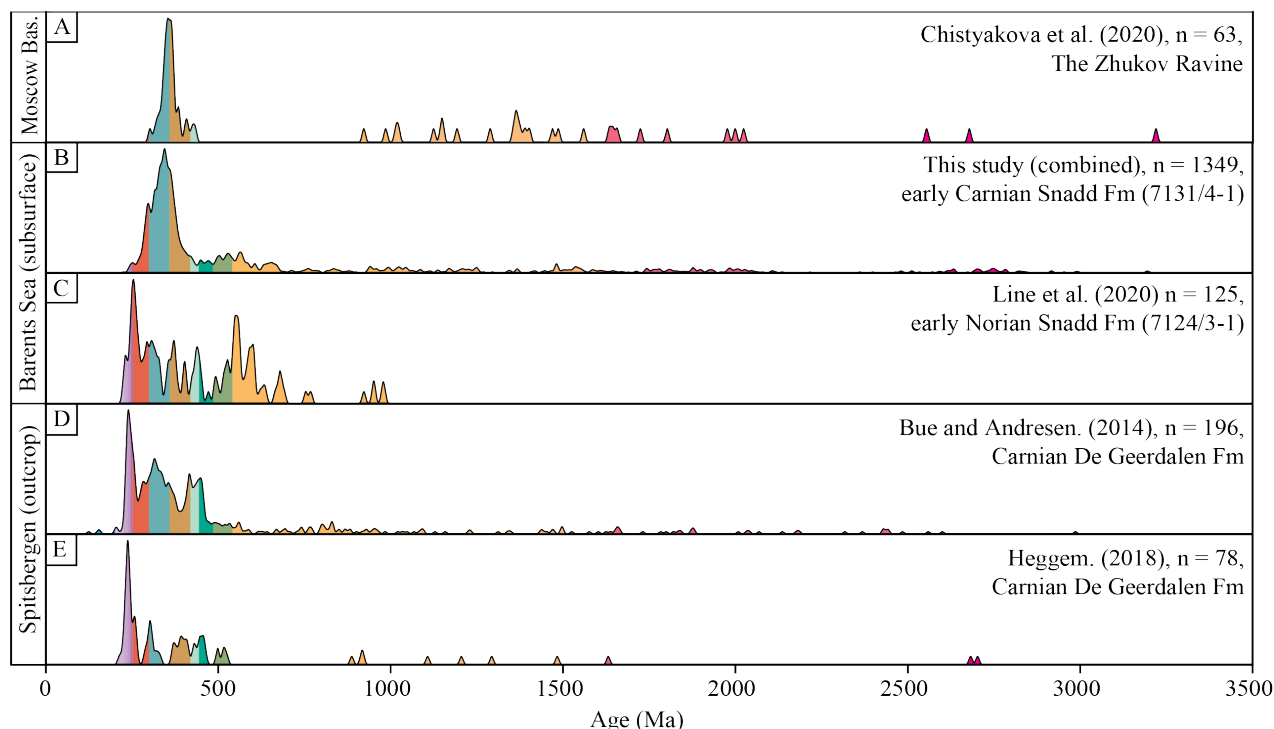
### 6.1.2 Young Triassic zircon grains

Upper Triassic samples from the southern Barents Sea generally show detrital zircon age spectra with a typical Paleozoic age component, whereas a Triassic peak is much more prominent on the samples from Svalbard (Fig. 6.3). The reason for this difference has not yet been resolved. According to Fleming et al. (2016), Svalbard was influenced by another northern source, while e.g., Klausen et al. (2017) and Gilmullina et al. (2020) suggests that this might be because the published onshore and offshore samples from the Snadd and De Geerdalen formations are not entirely time-equivalent. In the southern Barents Sea, the samples from the Snadd Fm are of early Carnian (C1) age, and those on Svalbard are from the late Carnian (C3 – C4). It is likely that there was a geodynamic event in the source area in the east between C2 and C3. It is therefore possible that the young zircon grains are related to young magmatism in the northern Urals and the Barents Sea, or that they originate from The Central Asian Orogenic Belt (Gilmullina et al., 2021).

The age spectra from the subsurface Snadd Fm (Line et al., 2020) and the onshore De Geerdalen Fm on Svalbard (Bue and Andresen, 2014; Heggem, 2017), display Upper Triassic sediments with young detrital zircon ages that are almost equal to the depositional age (Figs. 6.3B – E). The zircon spectra from Line et al. (2020) display a distinct Early Triassic peak, accompanied by a peak at 600 Ma. In this study, there are 13 grains with Triassic age, 12 when maximum uncertainty range is added, and 19 when minimum uncertainty range is added. This means that

Triassic zircons are present in southern parts of the Barents Sea and increases the possibility that there are more young zircons in the later Triassic parts of core 7131/4-1 as well.

The samples in this thesis are from C1 and can therefore not answer whether there are zircon spectra with young ages in Carnian C3 and C4 interval within the southern Barents Sea alone. The interpreted Guovca channel body is quite southernly positioned, has a large width and depth, paleocurrent direction deriving from the east-southeast, and therefore assumed to originate from the Uralian foreland basin (Klausen et al., 2014).



**Figure 6.3:** Zircon age spectra from the Moscow Basin (A), Barents Sea (B and C), and Spitsbergen (D and E) displaying the change in number of Triassic zircon grains. A) Shows a typical Uralian age spectra and is collected from Moscow Basin (Chistyakova et al., 2020). Note the absence of Triassic grains in this study, which is south-easterly positioned. The small Triassic peak in the study by Line et al. (2020), which is more western positioned. The study by Bue & Andresen (2014) and Heggem (2017) clearly show distinct Triassic peaks. The sample from Line et al. (2020) is deposited later (early Norian) while the three others are Carnian.

The detrital zircon age spectra presented in this thesis (Fig. 6.3B) have similarities to the zircon spectra which are produced from the foreland basin in the Urals (Fig. 6.3A; Chistyakova et al., 2020), *c.* 45 % of the grains presented in this thesis fall between Late Devonian and early Permian, and main peak is positioned at the late Carboniferous (36 % of the grains). There is also a small collection of grains with Silurian to Mesoproterozoic age (~32 % of the grains). The Zhukov Ravine sample presented by Chistyakova et al. (2020) has its peak at 362 Ma, which is similar to the spectra in this thesis, and they both display a Uralian peak matching each other. Silurian to mid-Neoproterozoic samples is not present in the Triassic samples from Zhukov Ravine, while this thesis displays a good collection. These samples must be of an origin

that was only restricted to the southwestern Barents Sea at the Carnian time. This thesis has contributed with a total of 1349 detrital zircon grains to strengthen the determination on an east-southeastern source in the southern Barents Sea, and that there is very limited but visible Triassic peaks in the Early Carnian deposits in the southwestern Barents Sea. The Triassic zircons from Line et al. (2020) is evidence that the young zircons reached the southern Barents Sea at least at the end of the Snadd time. However, without samples that are from C3 and C4 intervals in the southern Barents Sea, it is not possible to clearly distinguish between these two explanations, which is important as it supports the theory that there was a geodynamic event close to the depositional area between early Carnian and early Norian, not in the north as assumed by (Fleming et al., 2016).

In this study, two samples (BAR-71 and BAR-72) present zircon grains with early Norian ages (c. 224 – 226 Ma), which is younger than the depositional age of the sediments. There are several possible explanations for this: 1) The stratigraphic interval of the studied core interval stretches further than assumed, 2) the calibration of the U-Pb ages against the standards can be slightly wrong so that ages are adjusted to overall younger ages, 3) or that the stratigraphic age of the samples is not correct. This issue is not important for the overall interpretations in this thesis, but it can be to other publications. The stratigraphic age determination of this study is done based on palynology (Vigran et al., 2014), and the exact tie of the palynological zonation to numerical U-Pb ages is not straightforward. The presence of young zircons in the Triassic Barents Sea offers a way to confirm or refine the age of the palynological zonation.

## 6.2 What causes the large observed zircon fertility variations?

Zircon fertility variations are highly visible in the samples collected from core 7131/4-1, and they vary from sample to sample with 0 to 500 grains. It is highly desired to have the ability to predict high fertility sandstone, as the validity of provenance analysis increases with higher amounts of grains. The causes of zircon fertility are complex. Detrital zircon U-Pb ages can cluster by grain size (Sircombe et al., 2001; Garzanti et al., 2009; Lawrence et al., 2011; Ibañez-Mejia et al., 2018), and grain size sorting is strongly influenced by the dynamics of sediment transport (Udden, 1914; Hajek et al., 2010). Fertility can also vary within types of rocks, ultramafic and mafic rocks tend to have low fertility, while felsic rocks show high (Chew et al., 2020).

The facies division in this thesis provides a qualitative interpretation of energy flow conditions based on the clast size, shapes, and types that are present in the core samples. After the second sampling, the hypothesis for zircon fertility prediction provided supporting evidence. Zircon grains were mainly found in the surrounding sandstone matrix, not in siderite- and mud clasts. Mud-draped sandstone displayed a higher number of zircons in the second round of sampling than in the first round. Zircons per gram in facies and results from the hypotheses testing combined gives a plausible model that zircon fertility increases with higher energy flow conditions.

From this study, the silt- and mud sized material (**Facies F7**) show no- to limited fertility, possibly because the material is too fine-grained and detrital zircon grains are denser and were deposited at a more proximal position than the fine-grained material. Zircon which are small-grained and have a high density tend to settle with coarse-grained quartz since they have a low density (Cantine et al., 2021). Of the sandstone facies, the structureless- and mud-draped sandstone (**Facies F1 and F2**) displayed the lowest fertility and is interpreted to be deposited under the lowest of the medium energy flow conditions because of the lack of intraformational elements (Cabello et al., 2018). The pebbly sandstone (**Facies F3**) shows a much higher abundance of zircons than the two with lower energy. The difference in energy level between the three mentioned facies is limited, but still present.

Sandstone with cm-scale red clasts (**Facies F4A**) has a much lower zircon fertility value (Tab. 5.3) than sandstone with cm-grey clasts (**Facies F4B**). It should be noted that the samples from the second round of sampling are included here, and the latter samples consisted mainly of clasts with lower fertility. The average fertility value of Facies F4B is therefore lower than expected. The moderate- and poorly sorted sandstone conglomerate (**Facies F5A and F5B**) are interpreted as a high energy environment. F5B has a lower fertility value than the two other high energy facies, but still a higher value than **F1** and **F2**. Sandstone with rounded to- angular clasts, channel lag deposits (**Facies F6**) has the third-highest fertility value and is also interpreted as high energy flow conditions (Collinson, 2019). The calcite concretion (**Facies F10**) has unexpected low fertility as the sample material is to a large degree similar to the Facies F1, only cemented with calcite.

The variations in fertility clearly indicate a correlation to the flow conditions. However, there might also be other explanations as there are only quantitative numbers supporting this in this thesis. We see from BAR-72, with 501 zircons grains in 32 g sample that high fertile samples exist in subsurface cores. This also shows that zircons are highly present in the Barents Sea



sediments, and that contribute to the fertility-understanding-subject is needed. The samples in this thesis show similarities between the spectra throughout the cored interval, even though facies with different energy flow conditions are abundant. From zircon picking, and measurements of zircon size in Section 5.5, significant zircon size differences are observed, as well as shape differences. The difference in grain and shape is widely represented in all samples which is an indicator that the energy flow conditions can affect fertility, but the zircon grains are still represented with different sizes and shapes in all samples. This gives support to the theory that the sediments are not clustered by grain size and age in this case as it is for the case of Ibañez-Mejia et al. (2018). The difference between the largest and lowest mean zircon size value was *c.* 60  $\mu\text{m}$ . The sample with the highest and lowest value (BAR-74 and -80) show the largest uncertainty, which weakens the validity of the measurements. This narrows the difference in mean size, and the variations may therefore be more equal than what the results indicate. The mean zircon size varies from Ibañez-Mejia et al. (2018) varies between 75 and 220  $\mu\text{m}$ , which is significantly higher than the samples in this thesis. Zircon deposited in the Carnian Snadd Fm seems to have a quite even zircon size that is present in all samples.

### 6.2.1 Other fertility causes

There are other fertility affecting processes that have not been largely reviewed in this thesis. Bedrock geology is one of them (Malusà et al., 2016), but since all the samples in this thesis are interpreted to be sourced mainly from the same provenance, they are thought to be equally affected. The fertility variations in the Uralian sediment in this thesis vary between 0 – 500 grains, with most of the samples yielding up to 164 grains. Whether these fertility variations are large is hard to distinguish, as there are few observations of publications that calculates the zircon per gram sample value.

Fertility may also be affected/biased during mineral separation (Chew et al., 2020). The stepwise process of separating sandstone to a pure amount of zircon requires many steps. The water shaking table, which was not used in this thesis, may sort out distinct zircon sizes when a wide size variation is present (Sláma and Košler, 2012). Replacement of water shaking table by sample washing in beaker increase the control on the separation between light and dense material. This method is not applied in any other papers targeting zircon fertility, so the effect on fertility is not outlined. In this study, all the samples have been similarly treated and significant variations are not assumed to be caused by this. Biases in conjunction with zircon

handpicking has previously been addressed (Dröllner et al., 2021), but in this, all zircon in the samples were picked and analyses to prevent fertility biases from this step.

Zircon is only one of few heavy minerals that are used for provenance because of its properties. Some of the other heavy minerals are affected by other fertility affecting processes. The properties of zircons allow some fertility affecting processes to be ruled out. Zircon is not largely affected by e.g., diagenesis, which other heavy minerals are (Chew et al., 2020). This is one of the reasons why zircon is so widely used. During physical and chemical weathering, zircon accompanied by apatite, are highly robust (Morton and Hallsworth, 1999)

6.3 Is there a sorting/facies control on zircon age spectra as well? Are the different zircon age spectra representative? Do the different samples pass statistical test for similarity?

### 6.3.1 Age spectra control

Variations in zircon fertility are highly supported, but the question of whether the zircon age spectra are affected by facies or sorting is still questionable. The zircon age spectra may occur dissimilar from a visible point of view. This is because of fertility which causes age spectra with a low number of grains to have large space between the peaks. The peaks are plotted as kernel density plots, not the number of grains, leaving the peaks tall and unaffected by fertility. The fertility seems to be affected by energy flow conditions and the question of whether there are controls on zircon spectra arises, such as sorting of sediments or by facies. The MDS plot (Fig. 5.9) in Section 5.4.1 show very small variations between the age spectra and are mostly related to fertility. Low fertility gives few grains to calculate similarity, causing the spectra to look dissimilar. In this study, sorting control on detrital zircon age spectra has not been observed. The zircon size displays a generally moderate variation in size that is present in all samples, indicating that there is little opportunity for sorting to affect age spectra in this system. The large variation in fertility is a supporting argument to the fact that there is no sorting control observed, if sorting control was affecting the age spectra, a more equal fertility within the facies should be observed.

Small variations are also observed between the facies combined age spectra in the MDS plot in 5.4.2 (Fig. 5.10). A facies control would cause larger dissimilarities between the combined facies spectra plotted in the MDS plot of facies combined spectra, and a more equal fertility within each facies would be expected. The zircon fertility variations in some of the facies are

also very large. If the zircon age spectra would have been affected by facies, the facies would show a similar number of zircon grains in all the samples in one facies. The large fertility variations are a cause of dissimilar age spectra, a cause of high uncertainty to each facies, and a cause to why there is little support given to the question on facies control.

### 6.3.2 Representative age spectra and statistical approval

When it comes to the aspect of whether the zircon age spectra are representative, there is a twofold aspect to this. Are they statistically representative and/or are they representative in the way that they show useful results? One can of course refer to publications suggesting that 117 grains is wanted, and 95 grains when prior knowledge on the population exist to say the spectra is representative (Vermeesch, 2004). In this thesis, 18 zircon age spectra were produced from the same cored interval, and they all showed very small variations in the MDS plot (Fig. 5.9). Only three age spectra pass the suggested number of grains ( $\geq 95$ ), even when it is lowered because prior knowledge exists (BAR-72, -82, and -86). The MDS plot (Fig. 5.9) of all samples shows a clear cluster of samples, while five samples are positioned outside the cluster. The samples outside of the main cluster (inside the dotted square) can contain few numbers of grains, which is also the case for some samples in the outer range of the MDS plot (outside the dotted square). This shows that samples with low amounts of grains, such as BAR-74 ( $n = 11$ ) and BAR-71 ( $n = 14$ ) can display a high degree of similarity, even with a low number of grains.

The three samples with more than 117 grains are positioned both in the top and bottom of the cored interval, these clearly show similarities in the MDS plot, which means that the requirements for what is a representative spectrum can be lowered. In this thesis, we have used the samples with  $n \geq 30$  which are all located in the main cluster in the MDS plot. This gives significant support to whether the age spectra are statistically representative. The density plots show that the spectra with low number of grains display grains with ages within the same interval as those with high numbers (Fig. 5.8). It has not been observed any samples that have distinct age spectra that stand out. This is observed both from the visuals of the spectra and the MDS plot. The visual and statistical aspect gives high confidence to whether the 13 detrital zircon age spectra are representative. The way they are combined with statistics and comparison with the other samples gives the spectra with  $n \geq 30$  a representative significance. The samples are also compared to other publications from the upper Snadd Fm, which is increasing the prior knowledge. Some of these publications also have number of grains lower than the suggested 117, and 95 for spectra with prior populations knowledge.

The MDS plot, in section 5.4.2 show spectra with small variation between them. The largest variations are observed between samples age spectra with low and high fertility. The low fertility age spectra do not provide enough grains to pass the statistical test. BAR-69, -70, -80, 81, and -84 contain such a low number of grains that they display a very low similarity. The case would have been different if the samples had a high number of grains, then the samples could have displayed more similar spectra and passed the statistical test. When the samples are combined as facies age spectra, one facies do not pass the statistical similarity (**Facies F10**) the reason for this is clearly the low number of grains.

#### 6.4 Advice for sampling in low zircon-fertility sandstone

One should be discrete when giving advice on where to sample in low zircon-fertility sandstone, because of the increasing practice of provenance studies and because of the high focus on bias when it comes to using detrital zircon grains from fluvial systems.

In this thesis a hypothesis for sampling low zircon-fertility sandstone was made from the first round of sampling. The results from the testing supported the hypotheses, showing that energy levelled facies record higher zircon fertilities, and that detrital zircon grains are sourced from sand not mud- or siderite clasts. It partly confirmed that mud-draped sandstone has low zircon fertility, because the mud-draped sample displayed higher amounts of zircon grains than what was predicted in the hypothesis. The reason for this is that the collected mud-draped sandstone sample from the second sampling consisted of higher proportions of sand than previously collected mud-draped sandstone samples. From the zircon fertility prediction model, the advice would be to sample sand matrix in areas that reflect high energy flow environment, preferably intervals bearing high-density clasts as these will have had lighter material winnowed out. Mud-draped intervals or intervals with dark laminae should be avoided, as the draped are often rich in organic matter.

There are certain advises to be given in the preparation of zircon samples when limited material is available. Firstly, it's important to make sure all sample material to all time is included. A paint brush was used in many cases to make sure of this, with a new brush for each step and sample. When washing the samples to remove mud, washing in a one L beaker was very useful as it left us with better control on the heavy fractions. It's important during the picking of zircon grains to have some experience, and to know how different zircons can appear, cause zircon can be very different in shape, size, and colour.

Bulk-mounting, as done in this thesis, is a preferable way of presenting zircon grains compared to handpicking. Zircon age spectra produced from handpicked zircons have tendency to not show valid spectra as ages are ruled out during picking of preferential grains (Dröllner et al., 2021). The importance of this is less in this thesis as all zircons in the samples was collected. Else, following conservative mineral separation procedures is recommended to avoid loss of small volcanic zircon grains (Edwards et al., 2014; Sláma and Košler, 2012).

## 7 SUMMARY AND CONCLUSIONS

---

Through seismic interpretation, facies analysis, detrital zircon geochronology, and petrological interpretation a meandering point bar deposit from the late Triassic Snadd Formation has been investigated. After evaluating the results in its own and in combination with associated literature there are several outcomes of this thesis, which are as followed:

- The Guovca prospects displays a large meandering point bar deposit from the Carnian Snadd Formation. Ten facies and four sub facies have been interpreted from the penetrating core 7131/4-1 which reflect various energy flow conditions.
- From the facies division, the cored section contains mid- and upper channel-, channel base-, and channel lag deposits, consisting of very fine- to medium sandstones. Paleosol, floodplain, and floodplain lake deposits are interpreted from silt- and mud stones and coal deposits. Calcite concretions are present as well.
- Large variations on zircon fertility are visible in the interpreted sandstone units, the causes of this are believed to be caused by variations in energy flow conditions connected to geodynamics in the Guovca point bar. There are not observed any changes in the appearance of the detrital zircon age spectra that can be caused by variations in facies or any sorting effects.
- Detrital zircon age spectra from core 7131/4-1 in southwestern Barents Sea display signatures of Uralian sourced sediments throughout the cored interval. This theory is supported by the positioning of the Guovca meandering river, the petrological investigations, and in comparison, with other zircon age spectra signatures from the Barents Sea.
- Statistically the zircon age spectra display similar age spectra through the interval, lowest fertility age spectra display the lowest similarity, and low to high fertility age spectra display the highest similarity.
- There has not been observed any sorting or facies control on the detrital zircon age spectra, the small variations in zircon size and zircon shape is present in all samples indicate little opportunity for sorting effects in this system.
- Limited amounts of young Triassic zircons are present in the early Carnian time, majority of these display ages ranging from 242 Ma to 254 Ma and reflect that there was not any geodynamic event providing young Triassic zircon to the southwestern Barents Sea during the early Carnian Snadd.

- The advice to sample high energy flow condition sandstones is given from this study, and model testing is highly recommendable when outlining zircon fertility in sedimentary environment.

## 8 FURTHER WORK

---

This thesis has contributed with increasing the understanding of intraformational fertility variations through a sedimentary core and providing valuable information on sediment provenance. To create a higher validity to the results and increase sediment understanding in the late Triassic sediments, the following suggestions for further work are:

- Use this type of study on fluvial systems, both subsurface, but also in modern/ancient systems that are directly available in outcrops. Test the presented zircon fertility hypothesis on low and high fertility sandstones. Aim to sample areas that reflect high energy facies mainly, and partly sample areas that are reflecting low energy facies as they can give supporting evidence to the theory.
- Continue to investigate zircon dispersal from the Great Barents Sea Basin to understand the constrain of Uralian, Fennoscandian, and Caledonian sediments in the Triassic and Jurassic sediments.



## REFERENCES

---

- Algeo, T. J. & Twitchett, R. J. (2010). Anomalous Early Triassic sediment fluxes due to elevated weathering rates and their biological consequences. *Geology*, 38, 1023-1026.
- Andersen, T., Elburg, M. A. & Magwaza, B. N. (2019). Sources of bias in detrital zircon geochronology: Discordance, concealed lead loss and common lead correction. *Earth-Science Reviews*, 197, 102899.
- Augustsson, C., Voigt, T., Bernhart, K., Kreißler, M., Gaupp, R., Gärtner, A., Hofmann, M. & Linnemann, U. (2018). Zircon size-age sorting and source-area effect: The German Triassic Buntsandstein Group. *Sedimentary Geology*, 375, 218-231.
- Bergan, M. & Knarud, R. (1993). Apparent changes in clastic mineralogy of the Triassic–Jurassic succession, Norwegian Barents Sea: possible implications for palaeodrainage and subsidence. In: Vorren, T. O., Bergsager, E., Dahl-Stamnes, Ø. A., Holter, E., Johansen, B., Lie, E. & Lund, T. B. (eds.) *Arctic Geology and Petroleum Potential. Norwegian Petroleum Society. Special Publications*, vol. 2, 481–493, Elsevier, Amsterdam.
- Bjerga, A., Stubseid, H., Pedersen, L.-E. & Pedersen, R. B. (2021). Inherited Continental Zircons in Oceanic Rocks—True or False.
- Bue, E. P. & Andresen, A. (2014). Constraining depositional models in the Barents Sea region using detrital zircon U–Pb data from Mesozoic sediments in Svalbard. *Geological Society, London, Special Publications*, 386, 261-279.
- Bugge, T., Mangerud, G., Elvebakk, G., Mørk, A., Nilsson, I., Fanavoll, S. & Vigran, J. O. (1995). The Upper Palaeozoic succession on the Finnmark Platform, Barents Sea. *Norsk Geologisk Tidsskrift*, 758(1), 3-30.
- Cabello, P., Domínguez, D., Murillo-López, M. H., López-Blanco, M., García-Sellés, D., Cuevas, J. L., Marzo, M. & Arbués, P. (2018). From conventional outcrop datasets and digital outcrop models to flow simulation in the Pont de Montanyana point-bar deposits (Ypresian, Southern Pyrenees). *Marine and Petroleum Geology*, 94, 19-42.
- Cantine, M. D., Setera, J. B., Vantongeren, J. A., Mwinde, C. & Bergmann, K. D. (2021). Grain size and transport biases in an Ediacaran detrital zircon record. *Journal of Sedimentary Research*, 91(9), 913-928.
- Carling, P., Kelsey, A. & Glaister, M. (1992). Effect of bed roughness, particle shape and orientation on initial motion criteria. *Dynamics of gravel-bed rivers*, 24-39.
- Chew, D., O'sullivan, G., Caracciolo, L., Mark, C. & Tyrrell, S. (2020). Sourcing the sand: Accessory mineral fertility, analytical and other biases in detrital U–Pb provenance analysis. *Earth-Science Reviews*, 202, 103093.
- Chistyakova, A., Veselovskiy, R., Semenova, D., Kovach, V., Adamskaya, E. & Fetisova, A. (2020). Stratigraphic Correlation of Permian–Triassic Red Beds, Moscow Basin, East European Platform: First Detrital Zircon U–Pb Dating Results. *Doklady Earth Sciences*, Springer, vol. 492(1), 306-310.
- Collinson, J. (2019). *Sedimentary structures*, Dunedin Academic Press Ltd.
- Connelly, J. N. (2001). Degree of preservation of igneous zonation in zircon as a signpost for concordancy in U/Pb geochronology. *Chemical Geology*, 172(1-2), 25-39.

- Davis, D. W., Williams, I. S. & Krogh, T. E. (2018). 6. Historical development of zircon geochronology. *Reviews in mineralogy and geochemistry*, 53 (1), 145 – 182.
- Dengo, C. A. & Rössland, K. G. (1992). Extensional tectonic history of the western Barents Sea. *Structural and tectonic modelling and its application to petroleum geology*, 91 – 107, Elsevier.
- Doré, A. (1995). Barents Sea geology, petroleum resources and commercial potential. *Arctic*, 207 – 221.
- Doré, A. G. (1992). The Base Tertiary Surface of southern Norway and the northern North Sea. *Norsk Geologisk Tidsskrift*, 72(3), 259 – 265.
- Dowey, P. J., Hodgson, D. M. & Worden, R. H. (2012). Pre-requisites, processes, and prediction of chlorite grain coatings in petroleum reservoirs: a review of subsurface examples. *Marine and Petroleum Geology*, 32(1), 63 – 75.
- Dröllner, M., Barham, M., Kirkland, C. L. & Ware, B. (2021). Every zircon deserves a date: selection bias in detrital geochronology. *Geological Magazine*, 158(6), 1135 – 1142.
- Durkin, P. R., Boyd, R. L., Hubbard, S. M., Shultz, A. W. & Blum, M. D. (2017). Three-dimensional reconstruction of meander-belt evolution, Cretaceous McMurray Formation, Alberta foreland basin, Canada. *Journal of Sedimentary Research*, 87(10), 1075 – 1099.
- Edwards, K. L., Padilla, A. J., Evans, A., Morgan, D. J., Balco, G., Putkonen, J. & Bibby, T. (2014). Provenance of glacial tills in Ong Valley, Antarctica, inferred from quartz cathodoluminescence imaging, zircon U/Pb dating, and trace element geochemistry. *AGU Fall Meeting Abstracts*, 2014. EP12B-07.
- Eide, C. H., Klausen, T. G., Katkov, D., Suslova, A. A. & Helland-Hansen, W. (2018). Linking an Early Triassic delta to antecedent topography: Source-to-sink study of the southwestern Barents Sea margin. *Bulletin*, 130(1-2), 263 – 283.
- El Khoriby, E. (2006). Origin of calcite-cemented concretions in a fluvial sequence, the Malha Formation (Lower Cretaceous), El Tih Plateau, East Central Sinai, Egypt. *Mansoura Journal of Geology and Geophysics*, 33, 91 – 126.
- Faleide, J. I., Gudlaugsson, S. T. & Jacquart, G. (1984). Evolution of the western Barents Sea. *Marine and Petroleum geology*, 1(2), 123 – 150.
- Faleide, J. I., Pease, V., Curtis, M., Klitzke, P., Minakov, A., Scheck-Wenderoth, M., Kostyuchenko, S. & Zayonchek, A. (2018). Tectonic implications of the lithospheric structure across the Barents and Kara shelves. *Geological Society, London, Special Publications*, 460(1), 285 – 314.
- Faleide, J. I., Vågnes, E. & Gudlaugsson, S. T. (1993). Late Mesozoic–Cenozoic evolution of the southwestern Barents Sea. *Geological Society, London, Petroleum Geology Conference Series*, 4(1), 933 – 950.
- Fedo, C. M., Sircombe, K. N. & Rainbird, R. H. (2003). Detrital zircon analysis of the sedimentary record. *Reviews in Mineralogy and Geochemistry*, 53(1), 277 – 303.
- Fleming, E. J., Flowerdew, M. J., Smyth, H. R., Scott, R. A., Morton, A. C., Omma, J. E., Frei, D. & Whitehouse, M. J. (2016). Provenance of Triassic sandstones on the southwest Barents Shelf and the implication for sediment dispersal patterns in northwest Pangaea. *Marine and Petroleum Geology*, 78, 516 – 535.

- Flowerdew, M. J., Fleming, E. J., Morton, A. C., Frei, D., Chew, D. M. & Daly, J. S. (2019). Assessing mineral fertility and bias in sedimentary provenance studies: examples from the Barents Shelf. *Geological Society, London, Special Publications*, 484(1), SP484. 11.
- Gac, S., Hansford, P. A. & Faleide, J. I. (2018). Basin modelling of the SW Barents Sea. *Marine and Petroleum Geology*, 95, 167 – 187.
- Galloway, W. E. & Hobday, D. K. (1996). Fluvial systems. *Terrigenous Clastic Depositional Systems, 60-90*, Springer.
- Garzanti, E. & Andò, S. (2019). Heavy minerals for junior woodchucks. *Minerals*, 9(3), 148.
- Garzanti, E., Andò, S. & Vezzoli, G. (2009). Grain-size dependence of sediment composition and environmental bias in provenance studies. *Earth and Planetary Science Letters*, 277(3-4), 422 – 432.
- Ghazi, S. & Mountney, N. P. (2009). Facies and architectural element analysis of a meandering fluvial succession: The Permian Warchha Sandstone, Salt Range, Pakistan. *Sedimentary Geology*, 221(1 – 4), 99 – 126.
- Gilmullina, A., Klausen, T. G., Doré, A. G., Rossi, V. M., Suslova, A. & Eide, C. H. (2021). Linking sediment supply variations and tectonic evolution in deep time, source-to-sink systems—The Triassic Greater Barents Sea Basin. *GSA Bulletin*.
- Gilmullina, A., Klausen, T. G., Paterson, N. W., Suslova, A. & Haug Eide, C. (2020). Regional correlation and seismic stratigraphy of Triassic Strata in the Greater Barents Sea: implications for sediment transport in Arctic basins. *Basin Research*, 33(2), 1546 – 1579.
- Glørstad-Clark, E., Birkeland, E., Nystuen, J., Faleide, J. & Midtkandal, I. (2011). Triassic platform-margin deltas in the western Barents Sea. *Marine and Petroleum Geology*, 28(7), 1294 – 1314.
- Glørstad-Clark, E., Faleide, J. I., Lundschie, B. A. & Nystuen, J. P. (2010). Triassic seismic sequence stratigraphy and paleogeography of the western Barents Sea area. *Marine and Petroleum geology*, 27(7), 1448 – 1475.
- Gudlaugsson, S. T., Faleide, J. I., Johansen, S. E. & Breivik, A. J. (1998). Late Palaeozoic structural development of the South-western Barents Sea. *Marine and Petroleum Geology*, 15(1), 73 – 102.
- Haile, B. G., Line, L. H., Klausen, T. G., Olaussen, S., Eide, C. H., Jahren, J. & Hellevang, H. (2021). Quartz overgrowth textures and fluid inclusion thermometry evidence for basin-scale sedimentary recycling: An example from the Mesozoic Barents Sea Basin. *Basin Research*, 33(3), 1697 – 1710.
- Hajek, E. A., Huzurbazar, S. V., Mohrig, D., Lynds, R. M. & Heller, P. L. (2010). Statistical characterization of grain-size distributions in sandy fluvial systems. *Journal of Sedimentary Research*, 80(2), 184 – 192.
- Hartley, A. J., Weissmann, G. S., Nichols, G. J. & Warwick, G. L. (2010). Large distributive fluvial systems: characteristics, distribution, and controls on development. *Journal of Sedimentary Research*, 80(2), 167 – 183.
- Haughton, P., Todd, S. & Morton, A. (1991). Sedimentary provenance studies. *Geological Society, London, Special Publications*, 57(1), 1 – 11.

- Heggem, B. (2017). *An analysis of facies in the De Geerdalen Formation and provenance across the Middle to Late Triassic boundary on Spitsbergen, Svalbard*. (Master's thesis, NTNU).
- Henriksen, E., Ryseth, A., Larssen, G., Heide, T., Rønning, K., Sollid, K. & Stoupakova, A. (2011). Tectonostratigraphy of the greater Barents Sea: implications for petroleum systems. *Geological Society, London, Memoirs*, 35(1), 163 – 195.
- Hochuli, P. A. & Vigran, J. O. (2010). Climate variations in the Boreal Triassic—Inferred from palynological records from the Barents Sea. *Palaeogeography, Palaeoclimatology, Palaeoecology*, 290(1 – 4), 20 – 42.
- Hudson, P. F. & Kesel, R. H. (2000). Channel migration and meander-bend curvature in the lower Mississippi River prior to major human modification. *Geology*, 28, 531 – 534.
- Ibañez-Mejia, M., Pullen, A., Pepper, M., Urbani, F., Ghoshal, G. & Ibañez-Mejia, J. C. (2018). Use and abuse of detrital zircon U-Pb geochronology—A case from the Río Orinoco delta, eastern Venezuela. *Geology*, 46(11), 1019 – 1022.
- Jackson, S. E., Pearson, N. J., Griffin, W. L. & Belousova, E. A. (2004). The application of laser ablation-inductively coupled plasma-mass spectrometry to in situ U–Pb zircon geochronology. *Chemical geology*, 211(1 - 2), 47 – 69.
- Johnson, S. P., Kirkland, C. L., Evans, N. J., McDonald, B. J. & Cutten, H. N. (2018). The complexity of sediment recycling as revealed by common Pb isotopes in K-feldspar. *Geoscience Frontiers*, 9(5), 1515 – 1527.
- Klausen, T. G., Müller, R., Slama, J. & Helland-Hansen, W. (2017). Evidence for Late Triassic provenance areas and Early Jurassic sediment supply turnover in the Barents Sea Basin of northern Pangea. *Lithosphere*, 9(1), 14 – 28.
- Klausen, T. G., Nyberg, B. & Helland-Hansen, W. (2019). The largest delta plain in Earth's history. *Geology*, 47(5), 470 – 474.
- Klausen, T. G., Ryseth, A. E., Helland-Hansen, W., Gawthorpe, R. & Laursen, I. (2014). Spatial and temporal changes in geometries of fluvial channel bodies from the Triassic Snadd Formation of offshore Norway. *Journal of Sedimentary Research*, 84(7), 567 – 585.
- Klausen, T. G., Ryseth, A. E., Helland-Hansen, W., Gawthorpe, R. & Laursen, I. (2015). Regional development and sequence stratigraphy of the Middle to Late Triassic Snadd formation, Norwegian Barents Sea. *Marine and Petroleum Geology*, 62, 102 – 122.
- Labrecque, P., Hubbard, S., Jensen, J. & Nielsen, H. (2011). Sedimentology and stratigraphic architecture of a point bar deposit, Lower Cretaceous McMurray Formation, Alberta, Canada. *Bulletin of Canadian Petroleum Geology*, 59(2), 147 – 171.
- Lasabuda, A. P., Johansen, N. S., Laberg, J. S., Faleide, J. I., Senger, K., Rydningen, T. A., Patton, H., Knutsen, S.-M. & Hanssen, A. (2021). Cenozoic uplift and erosion on the Norwegian Barents Shelf—A review. *Earth-Science Reviews*, 217, 103609.
- Lawrence, R. L., Cox, R., Mapes, R. W. & Coleman, D. S. (2011). Hydrodynamic fractionation of zircon age populations. *Bulletin*, 123(1 – 2), 295 – 305.
- Lee, J. K., Williams, I. S. & Ellis, D. J. (1997). Pb, U and Th diffusion in natural zircon. *Nature*, 390(6656), 159 – 162.
- Line, L. H., Müller, R., Klausen, T. G., Jahren, J. & Hellevang, H. (2020). Distinct petrographic responses to basin reorganization across the Triassic–Jurassic boundary in the southwestern Barents Sea. *Basin Research*, 32(6), 1463 – 1484.

- Malusà, M. G., Resentini, A. & Garzanti, E. (2016). Hydraulic sorting and mineral fertility bias in detrital geochronology. *Gondwana Research*, 31, 1 – 19.
- Mangerud, G. & Rømuld, A. (1991). Spathian-Anisian (Triassic) palynology at the Svalis Dome, southwestern Barents Sea. *Review of Palaeobotany and Palynology*, 70(3), 199 – 216.
- Miall, A. D. (1988). Reservoir heterogeneities in fluvial sandstones: lessons from outcrop studies. *AAPG bulletin*, 72(6), 682 – 697.
- Morton, A. C. (1991). Geochemical studies of detrital heavy minerals and their application to provenance research. *Geological Society, London, Special Publications*, 57, 31 – 45.
- Morton, A. C. & Hallsworth, C. R. (1999). Processes controlling the composition of heavy mineral assemblages in sandstones. *Sedimentary geology*, 124(1 – 4), 3 – 29.
- Mørk, M. B. E. (1999). Compositional variations and provenance of Triassic sandstones from the Barents Shelf. *Journal of Sedimentary Research*, 69, 690 – 710.
- Norwegian Petroleum Directorate. (2021). *NPD FactPages (FactMaps)* [Online]. Available: [https://factmaps.npd.no/factmaps/3\\_0/](https://factmaps.npd.no/factmaps/3_0/) [Accessed 13.11 2021].
- Nøttvedt, A., Cecchi, M., Gjelberg, J., Kristensen, S., Lønøy, A., Rasmussen, A., Rasmussen, E., Skott, P. & Van Veen, P. (1993). Svalbard-Barents Sea correlation: a short review. *Norwegian Petroleum Society Special Publications*, 2, 363 – 375.
- Omma, J. E. (2009). Provenance of Late Paleozoic and Mesozoic sediment to key Arctic basins: implications for the opening of the Arctic Ocean. [Ph.D. thesis]: Cambridge, UK, University of Cambridge.
- Paton, C., Woodhead, J. D., Hellstrom, J. C., Hergt, J. M., Greig, A. & Maas, R. (2010). Improved laser ablation U-Pb zircon geochronology through robust downhole fractionation correction. *Geochemistry, Geophysics, Geosystems*, 11(3).
- Powell, D. M. (1998). Patterns and processes of sediment sorting in gravel-bed rivers. *Progress in Physical Geography*, 22(1), 1 – 32.
- Puchkov, V. N. (2009). The evolution of the Uralian orogen. *Geological Society, London, Special Publications*, 327(1), 161 – 195.
- Pullen, A., Ibáñez-Mejía, M., Gehrels, G. E., Ibáñez-Mejía, J. C. & Pecha, M. (2014). What happens when n= 1000? Creating large-n geochronological datasets with LA-ICP-MS for geologic investigations. *Journal of Analytical Atomic Spectrometry*, 29, 971 – 980.
- Rossi, V. M., Paterson, N. W., Helland-Hansen, W., Klausen, T. G. & Eide, C. H. (2019). Mud-rich delta-scale compound clinoforms in the Triassic shelf of northern Pangea (Havert Formation, south-western Barents Sea). *Sedimentology*, 66(6), 2234 – 2267.
- Rubatto, D. & Gebauer, D. (2000). Use of cathodoluminescence for U-Pb zircon dating by ion microprobe: some examples from the Western Alps. *Cathodoluminescence in geosciences*, 373 – 400, Springer.
- Ryseth, A. (2014). Sedimentation at the Jurassic–Triassic boundary, south-west Barents Sea: indication of climate change. *From depositional systems to sedimentary successions on the Norwegian Continental Margin*, 187, 214.
- Saylor, J. E., Knowles, J. N., Horton, B. K., Nie, J. & Mora, A. (2013). Mixing of source populations recorded in detrital zircon U-Pb age spectra of modern river sands. *The Journal of Geology*, 121(1), 17 – 33.

- Sharman, G. R. & Johnstone, S. A. (2017). Sediment unmixing using detrital geochronology. *Earth and Planetary Science Letters*, 477, 183 – 194.
- Sharman, G. R., Sharman, J. P. & Sylvester, Z. (2018). detritalPy: A Python-based toolset for visualizing and analysing detrital geo-thermochronologic data. *The Depositional Record*, 4(2), 202 – 215.
- Simpson, G., Pecha, M. & Gehrels, G. (2012). Mineral separation instruction manual. *Arizona LaserChron Center*, 1.
- Sircombe, K. N., Bleeker, W. & Stern, R. A. (2001). Detrital zircon geochronology and grain-size analysis of a ~2800 Ma Mesoarchean proto-cratonic cover succession, Slave Province, Canada. *Earth and Planetary Science Letters*, 189(3 – 4), 207 – 220.
- Skjold, L. J., Van Veen, P., Kristensen, S.-E. & Rasmussen, A. R. (1998). Triassic sequence stratigraphy of the southwestern Barents Sea.
- Sláma, J. & Košler, J. (2012). Effects of sampling and mineral separation on accuracy of detrital zircon studies. *Geochemistry, Geophysics, Geosystems*, 13(5).
- Sláma, J., Košler, J., Condon, D. J., Crowley, J. L., Gerdes, A., Hanchar, J. M., Horstwood, M. S., Morris, G. A., Nasdala, L. & Norberg, N. (2008). Plešovice zircon—a new natural reference material for U–Pb and Hf isotopic microanalysis. *Chemical Geology*, 249(1 – 2), 1 – 35.
- Smelror, M., Petrov, O., Larssen, G. B. & Werner, S. (2009). Geological history of the Barents Sea. *Norges Geol. undersøkelse*, 1 – 135.
- Spencer, C. J. & Kirkland, C. L. (2016). Visualizing the sedimentary response through the orogenic cycle: A multidimensional scaling approach. *Lithosphere*, 8(1), 29 – 37.
- Taylor, A. & Goldring, R. (1993). Description and analysis of bioturbation and ichnofabric. *Journal of the Geological Society*, 150(1), 141 – 148.
- Udden, J. A. (1914). Mechanical composition of clastic sediments. *Bulletin of the Geological Society of America*, 25(1), 655 – 744.
- Vermeesch, P. (2004). How many grains are needed for a provenance study? *Earth and Planetary Science Letters*, 224(3 – 4), 441 – 451.
- Vermeesch, P. (2013). Multi-sample comparison of detrital age distributions. *Chemical Geology*, 341, 140 – 146.
- Vermeesch, P. (2018). Dissimilarity measures in detrital geochronology. *Earth-Science Reviews*, 178, 310 – 321.
- Vigran, J. O., Mangerud, G., Mørk, A., Worsley, D. & Hochuli, P. A. (2014). *Palynology and geology of the Triassic succession of Svalbard and the Barents Sea*, Norges geologiske undersøkelse, vol. 14.
- Wiedenbeck, M., Alle, P., Corfu, F. Y., Griffin, W., Meier, M., Oberli, F. V., Quadt, A. V., Roddick, J. & Spiegel, W. (1995). Three natural zircon standards for U-Th-Pb, Lu-Hf, trace element and REE analyses. *Geostandards newsletter*, 19(1), 1 – 23.
- Williams, G. D. (1966). Origin of Shale-Pebble Conglomerate1. *AAPG Bulletin*, 50(3), 573 – 577.
- Willis, B. J. (1989). Palaeochannel reconstructions from point bar deposits: a three-dimensional perspective. *Sedimentology*, 36(5), 757 – 766.

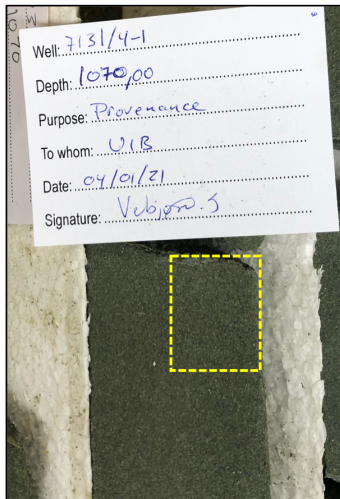
- Worsley, D. (2008). The post-Caledonian development of Svalbard and the western Barents Sea. *Polar research*, 27(3), 298 – 317.



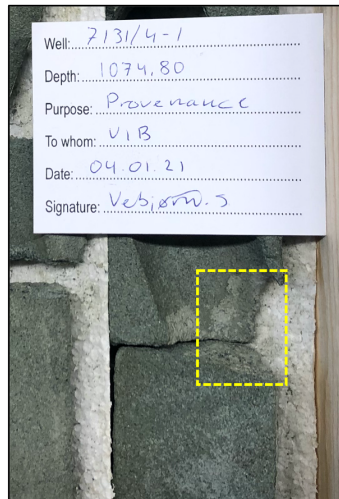
# APPENDICES

## 8.1 Appendix I – Samples

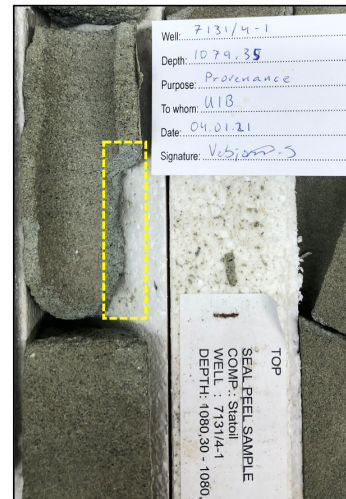
**BAR-69**



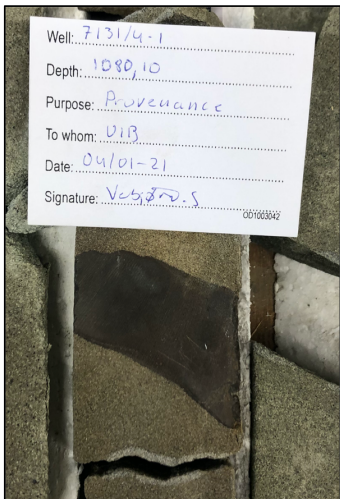
**BAR-70**



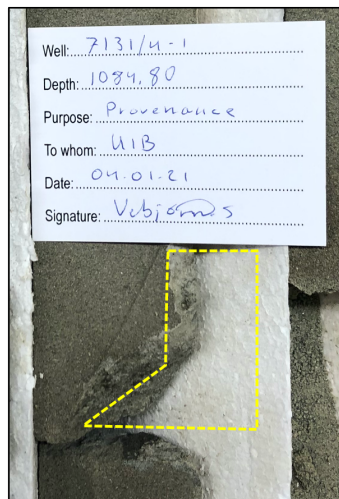
**BAR-71**



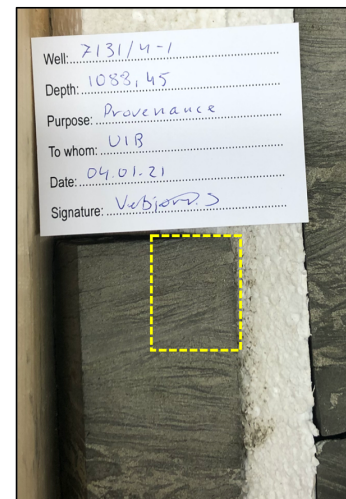
**BAR-72**



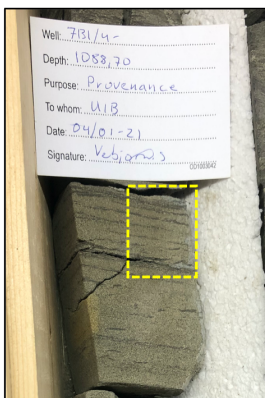
**BAR-73**



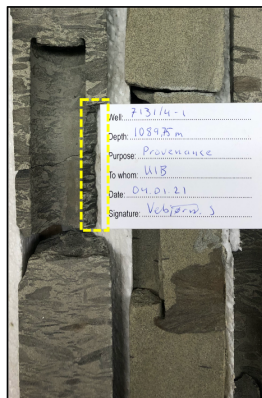
**BAR-74**



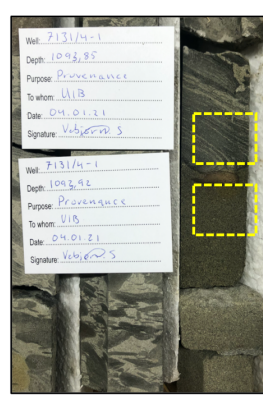
**BAR-75**



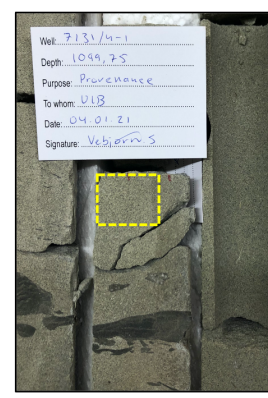
**BAR-76**



**BAR-77 & 78**

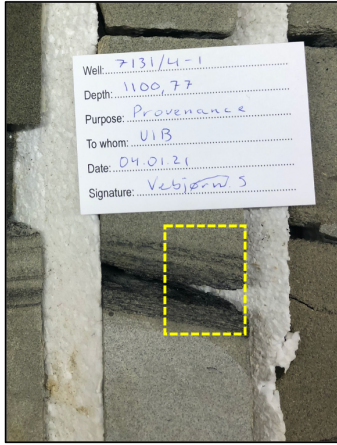


**BAR-79**

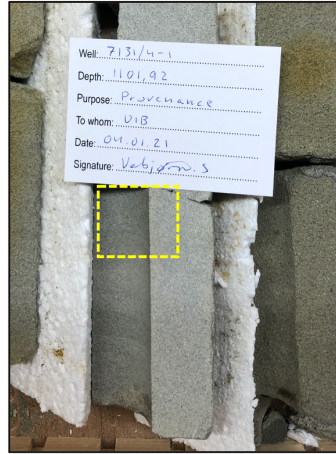




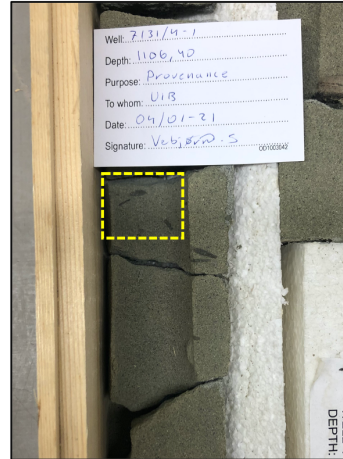
BAR-80



BAR-81



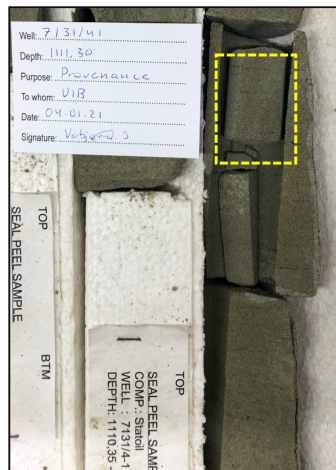
BAR-82



BAR-83



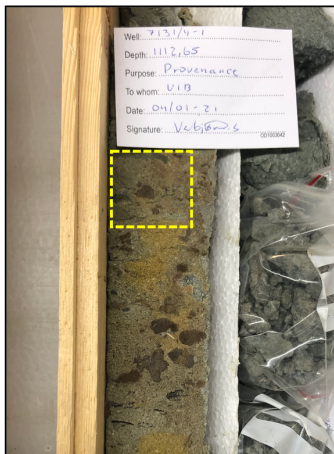
BAR-84



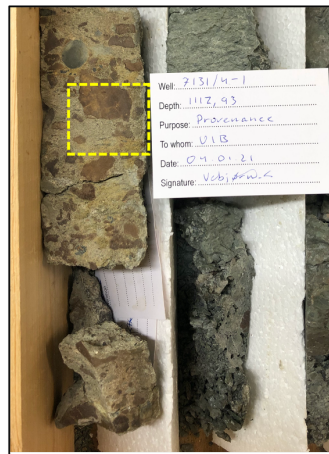
BAR-85



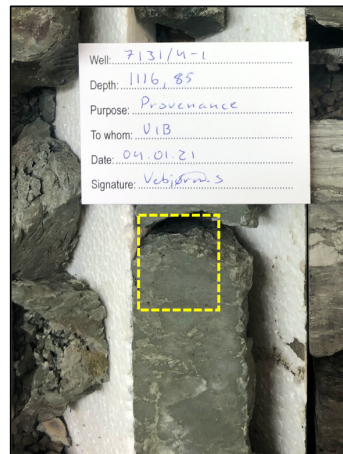
BAR-86



BAR-87



BAR-88



## 8.2 Appendix II – LA-ICP-MS

|  |  |
|--|--|
| <b>Laboratory &amp; Sample Preparation</b> |  |
| Laboratory name                            | Department of Earth Science, University of Bergen  |
| Sample type/mineral                        | Zircon   |
| Samples preparation                        | Conventional mineral separation, 2.5 cm resin mount, 0.025 $\mu$ m polish to finish  |
| Imaging                                    | CL, Zeiss Supra55 VP, 15 kV, 1 nA, 15mm working distance   |
| <b>Laser ablation system</b>               |  |
| Make, Model & type                         | RESolution M-50 LR with a Coherent COMPexPRO® 110 193 nm ArF excimer laser   |
| Ablation cell & volume                     | Two volume   |
| Laser wavelength                           | 193 nm   |
| Pulse duration                             | 20 ns  |
| Fluence                                    | 2.2 - 2.5 J.cm <sup>-2</sup>   |
| Repetition rate                            | 5 Hz   |
| Ablation duration                          | 30 secs  |
| Spot diameter                              | 26 $\mu$ m   |
| Sampling mode/pattern                      | Static spot ablation/circular  |
| Carrier gas                                | He (0.75 l/min) with small amounts of N <sub>2</sub> (0.004 ml/min) mixed in before entering the ICP-MS to increase sensitivity.   |
| Signal smoothing device                    | “Squid” connected between the laser and the ICP-MS   |
| <b>ICP-MS Instrument</b>                   |  |
| Make, Model & type                         | Nu Instruments, Nu Attom HR, SC-ICP-MS   |
| Sample introduction                        | Ablation aerosol from laser ablation   |
| RF power                                   | 1300W  |
| Cool gas                                   | Ar 13 l/min  |
| Aux gas                                    | Ar 0.7 l/min   |
| Make-up gas flow                           | Ar 0.49 l/min  |
| Detection system                           | MasCom Electron Multiplier   |
| Masses measured                            | <sup>202</sup> Hg, <sup>204</sup> (Hg + Pb), <sup>206</sup> Pb, <sup>207</sup> Pb, <sup>208</sup> Pb, <sup>232</sup> Th, <sup>238</sup> U  |
| Integration time per peak/dwell times      | 200 $\mu$ s for <sup>202</sup> Hg, <sup>204</sup> (Hg + Pb), <sup>206</sup> Pb, <sup>208</sup> Pb, <sup>232</sup> Th, <sup>238</sup> U<br>800 $\mu$ s for <sup>207</sup> Pb and <sup>235</sup> U |
| Number of sweeps per cycle                 | 10   |
| Total time per cycle 0.                    | 0.0493 s   |
| Analysis method                            | Deflector jump   |
| IC Dead time                               | 14 ns  |
| Detection Mode                             | Ion counting mode and ion-attenuated mode  |
| <b>Data Processing</b>                     |  |
| Gas blank                                  | 15 s   |

|  |  |
|--|--|
| Calibration strategy                               | 91500 (Wiedenbeck et al., 1995) used as primary reference material, while Plesovice (Sláma et al., 2008), & GJ1 (nr. 63; Jackson et al., 2004) are used as secondaries.  |
| Data processing package used / Correction for LIEF | Iolite4 (v. 4.4.5) for data normalization, uncertainty propagation and age calculation. LIEF correction assumes reference material and samples behave identically.   |
| Common-Pb correction                               | No common-Pb correction applied to the data. Analysis that are marked or cleared contain a significant amount of common lead, see table below.   |
| Data reduction                                     | VizualAge UComPbine (Chew et al. 2014)   |
| Down-hole correction model                         | Exponential or Exponential + linear  |
| Uncertainty level & propagation                    | Ages are quoted at 2s absolute, propagation is by quadratic addition.  |
| Quality control/validation                         | <p><b><u>Run 1 – LAS411, LAS412 and LAS413</u></b></p> <p>Plêsovice – Wtd ave <math>^{206}\text{Pb}/^{238}\text{U}</math> age = <math>342.17 \pm 0.079</math> Ma (1s, MSWD = 2.7, n = 208/208)</p> <p>GJ-1 – Wtd ave <math>^{206}\text{Pb}/^{238}\text{U}</math> age = <math>598.34 \pm 0.12</math> Ma (1s, MSWD = 150, n = 208/208)</p> <p>91500 – Wtd ave <math>^{206}\text{Pb}/^{238}\text{U}</math> age = <math>1062.93 \pm 0.23</math> Ma (1s, MSWD = 6.7, n = 208/208)</p> <p>Systematic uncertainty for propagation is 1% (1s).</p> |
| Data reporting                                     | Reported in the format of the plasmage.org data reporting template ( <a href="http://www.plasmage.org/recommendations/home.html">http://www.plasmage.org/recommendations/home.html</a> ) using a python script made by Joe Petrus ( <a href="https://github.com/iolite-LA-ICP-MS/iolite4-pythonexamples/blob/master/export/PlasmAge.py">https://github.com/iolite-LA-ICP-MS/iolite4-pythonexamples/blob/master/export/PlasmAge.py</a> ).   |
| Data visualization                                 | Plotting of KDE using IsoplotR (Vermesch, 2018)  |

### 8.3 Appendix III – U-Pb data

See attachment Appendix III